

1 Estimating 2010–2015 Anthropogenic and Natural Methane 2 Emissions in Canada using ECCC Surface and GOSAT Satellite 3 Observations

4 Sabour Baray¹, Daniel J. Jacob², Joannes D. Maasakkers³, Jian-Xiong Sheng⁴, Melissa P. Sulprizio²,
5 Dylan B.A. Jones⁵, A. Anthony Bloom⁶, and Robert McLaren¹

6 ¹Centre for Atmospheric Chemistry, York University, Toronto, Canada

7 ²Harvard University, Cambridge, MA, USA

8 ³SRON Netherlands Institute for Space Research, Utrecht, The Netherlands

9 ⁴Massachusetts Institute of Technology, Cambridge, MA, USA

10 ⁵University of Toronto, Toronto, Canada

11 ⁶Jet Propulsion Laboratory, California Institute of Technology, Pasadena, CA, USA

12 *Correspondence to:* Sabour Baray (sabour@yorku.ca)

13 **Abstract.** Methane emissions in Canada have both anthropogenic and natural sources. Anthropogenic emissions are estimated to
14 be 4.1 Tg a⁻¹ from 2010–2015 in the National Inventory Report submitted to the United Nation’s Framework Convention on
15 Climate Change (UNFCCC)-Canadian Greenhouse Gas Inventory. Natural emissions, which are mostly due to Boreal wetlands, are
16 the largest methane source in Canada and highly uncertain, on the order of ~20 Tg a⁻¹ in biosphere process models. ~~Top-down~~
17 ~~constraints on Canadian methane emissions using atmospheric observations have been limited by the sparse coverage of both~~
18 ~~surface and satellite observations.~~ Aircraft studies over the last several years have provided ‘snapshot’ emissions that ~~have been~~
19 ~~conflicting~~ with inventory estimates. Here we use surface data from the Environment and Climate Change Canada (ECCC)
20 in situ network and space borne data from the Greenhouse Gases Observing Satellite (GOSAT) to determine 2010–2015
21 anthropogenic and natural methane emissions in Canada in a Bayesian inverse modelling framework. We use GEOS-Chem to
22 simulate anthropogenic emissions comparable to the Canadian National Inventory and wetlands emissions using an ensemble of
23 WetCHARTS v1.0 scenarios in addition to other minor natural sources. We conduct a comparative analysis of the monthly natural
24 emissions and yearly anthropogenic emissions optimized by surface and satellite data independently. Mean 2010–2015 posterior
25 emissions using ECCC surface data are 6.0 ± 0.4 Tg a⁻¹ for total anthropogenic and ~~40.5~~11.6 \pm ~~4.9~~1.2 Tg a⁻¹ for total natural
26 emissions, ~~where the error intervals represent the 1- σ spread in yearly posterior results.~~ These results agree with our posterior using
27 GOSAT data of 6.5 ± 0.7 Tg a⁻¹ for total anthropogenic and 11.7 ± 1.2 Tg a⁻¹ for total natural emissions. The seasonal pattern of
28 posterior natural emissions using either dataset shows a slower to start emissions in the spring and a less intense peak in the
29 summer compared to the mean of WetCHARTS scenarios. We combine ECCC and GOSAT data to ~~evaluate capabilities~~
30 characterize limitations towards ~~for~~ sectoral and provincial level inversions ~~and identify limitations.~~ We estimate Energy +
31 Agriculture emissions to be 5.1 ± 1.0 Tg a⁻¹ which is 59% higher than the National GHG Inventory. We attribute 39% higher
32 anthropogenic emissions to Western Canada than the prior. Natural emissions are lower across Canada ~~with large downscaling in~~
33 ~~the Hudson Bay Lowlands.~~ Inversion results are verified against independent aircraft data ~~in Saskatchewan~~ and surface data ~~in~~

34 ~~Quebec~~ which show better agreement with posterior emissions. This study shows a readjustment of the Canadian methane budget is
35 necessary to better match atmospheric observations with lower natural ~~higher anthropogenic~~ emissions partially offset by higher
36 anthropogenic ~~lower natural~~ emissions.

37 1 Introduction

38 Methane is a significant anthropogenically-influenced greenhouse gas second to carbon dioxide in terms of its direct
39 radiative forcing (Myhre et al., 2013). The mixing ratio of methane has increased from ~720 to ~1800 ppb since pre-
40 industrial times (Hartmann et al., 2013). Present-day global methane emissions are well known to be $550 \pm 60 \text{ Tg a}^{-1}$ (Prather
41 et al., 2012). ~~However~~ recent trends in atmospheric methane since the 1990s are not well understood (Turner et al., 2019).
42 Anthropogenic methane sources include oil and gas activities, livestock, rice cultivation, coal mines, landfills, and
43 wastewater treatment. Natural methane emissions are dominated by wetlands, but also include seeps, termites and biomass
44 burning (Kirschke et al., 2013). The main sink of methane is oxidation by the hydroxyl radical (OH) resulting in a lifetime of
45 9.1 ± 0.9 years (Prather et al., 2012). Improving constraints on national methane emissions is a requirement of mitigation
46 policy (Nisbet et al., 2020). Here we use atmospheric methane observations from the Environment and Climate Change
47 Canada (ECCC) surface network and satellite observations from the Greenhouse Gas Observing Satellite (GOSAT) to
48 estimate Canadian methane emissions and disaggregate anthropogenic and natural sources.

49

50

~~The growth rate of atmospheric methane levelled off from the 1990's to early 2000's. This hiatus continued until 2007 when
52 methane concentrations began a renewed growth continuing to present time (Dlugokencky et al., 2009). Differing hypotheses
53 have attempted to constrain the possible causes of these decadal trends. Associated increases with ethane have attributed
54 recent growth to oil and gas (Hausmann et al., 2016). An increasing trend of isotopically lighter methane has been associated
55 with increasing biogenic emissions from wetlands and agriculture (Nisbet et al., 2016), however decreasing biomass burning
56 emissions may be masking increasing oil and gas emissions in the global isotopic ratios (Worden et al., 2017). Observations
57 of methyl chloroform suggest decreasing OH may have resulted in the renewed growth (Rigby et al., 2017; Turner et al.,
58 2017). Causal attribution of the methane growth rate has continued to be challenging partly because only a 3% source-sink
59 imbalance, or $\sim 20 \text{ Tg a}^{-1}$, can result in the observed rate of increase. Hence changes in the relative contributions from
60 anthropogenic and natural sources are key to understanding atmospheric methane.~~

61

~~Atmospheric observations provide constraints on methane emissions. In the the Government of Canada's submission to the
62 United Nations Framework Convention on Climate Change (UNFCCC), hereafter referred to as the National Inventory,
63 Canadian greenhouse gas inventory, anthropogenic emissions are estimated to be 4.1 Tg a^{-1} in 2015, with 68% of emissions
64 originating from the Western Canadian provinces of Alberta (42%), Saskatchewan (17%) and British Columbia (9%).~~

66 Sectoral contributions over the entire country are from three categories: Energy (49%), Agriculture (29%) and Waste (22%)
67 (Environment and Climate Change Canada, 2017). Natural emissions, which are mostly due to Boreal wetlands, are highly
68 uncertain, on the order of $\sim 10\text{--}30 \text{ Tg a}^{-1}$ from biosphere process modelling (Miller et al., 2014; Bloom et al., 2017).

69
70 Atmospheric observations provide constraints on methane emissions. –Studies constraining anthropogenic and/or natural
71 methane emissions within Canada have included the use of surface in situ measurements (Miller et al., 2016; Atherton et al.,
72 2017; Ishiziwa et al., 2019), aircraft campaigns (Johnson et al., 2017; Baray et al., 2018) and satellites (Wecht et al., 2014;
73 Turner et al., 2015; Maasakkers et al., 2020, 2021). These observations can determine emissions through mass balance
74 methods or be used in conjunction with a chemical transport model (CTM). Bayesian inverse modelling constrains prior
75 knowledge of emissions based on the mismatch between modelled and observed concentrations. This requires reliable
76 mapping of “bottom-up” inventory emissions for the “top-down” observational constraints to be useful (Jacob et al., 2016).
77 Inverse modelling has been more challenging for Canada than the United States due to a) the sparsity of surface stations and
78 satellite data (Sheng et al., 2018a), b) a factor of ~ 10 lower anthropogenic emissions (Maasakkers et al., 2019), c) large
79 spatially-overlapping emissions from Boreal wetlands that are highly uncertain (Miller et al., 2014), and d) model biases in
80 the high-latitudes stratosphere (Patra et al., 2011), compromising the interpretation of observed methane columns.

81
82 These observing system challenges have made Canadian methane emissions difficult to quantify. ~~However,~~ studies ~~have~~
83 ~~been showing~~ show a consistent story across different scales and measurement platforms. Miller et al. (2014, 2016)
84 determined that the North American network can successfully constrain Canadian natural emissions and found Boreal
85 wetlands to be lower in 2008 when compared to prior fluxes in the WETCHIMP model. Aircraft campaigns over the Alberta
86 oil and gas sector have found higher emissions than inventories in the Red Deer and Lloydminster regions (Johnson et al.,
87 2017) and unconventional oil extraction in the Athabasca Oil Sands region (Baray et al., 2018). Atherton et al. (2017)
88 conducted ground-based mobile measurements of gas production in British Columbia and determined higher emissions than
89 reported, and Zavala-Araiza et al. (2018) conducted similar ground-based measurements in Alberta to show a profile of
90 super-emitters dominating the fugitive methane profile similar to sites in the United States. Ishiziwa et al. (2019) constrained
91 arctic wetlands fluxes to be similar in magnitude to the mean of the WetCHARTS inventory but with better identified
92 seasonal and interannual variability. Satellite inversions over North America using the GEOS-Chem CTM and data from
93 SCIAMACHY (Wecht et al., 2014) or GOSAT (Turner et al., 2015; Maasakkers et al., 2019) consistently require upscaling
94 an increase in anthropogenic emissions in Western Canada and downscaling a decrease in natural emissions in Boreal
95 Canada to match observations, even with the use of updated Canadian fluxes in Maasakkers et al. (2019) for anthropogenic
96 (Sheng et al., 2017) and wetlands (Bloom et al., 2017) sources. Inverse modelling studies that use both in situ and satellite
97 observations are valuable for intercomparison and for identifying the limits of spatial and temporal discretization that are
98 possible (Lu et al., 2021; Tunnicliffe et al., 2020). The Tropospheric Monitoring Instrument (TROPOMI) launched in 2017
99 with a data record beginning in 2018 and is expected to provide significant improvements in emissions monitoring through

denser observational coverage at a similar precision to GOSAT (Hu et al., 2018). It is necessary to build a reliable historical record of Canadian methane emissions, as anthropogenic emissions are sensitive to changes in policy and economic activity (Rogelj et al., 2018) and natural emissions in Boreal Canada may be sensitive to climate change (Kirschke et al., 2013).

In this study we use surface observations from the ECCC GHG monitoring network and satellite data from GOSAT to constrain anthropogenic and natural emissions in Canada. We use the GEOS-Chem CTM to simulate 2010–2015 methane concentrations. The model setup includes the use of an improved bottom-up inventory for Canadian oil and gas emissions (Sheng et al., 2017), the WetCHARTS extended ensemble for ~~wetlands emissions~~ wetland emissions (Bloom et al., 2017) and EDGAR v4.3.2 for other anthropogenic sources. We perform an ensemble forward model analysis which compares six wetlands scenarios to the ECCC surface observation network to assess the influence of process model configurations on Canadian methane. A series of Bayesian inverse analyses are performed that use ECCC and GOSAT data independently and in a joint surface-satellite system. We constrain monthly natural emissions and yearly total anthropogenic emissions from 2010–2015 using ECCC and GOSAT data independently for ~~intercomparison~~ comparison to produce aggregated-source emissions estimates. We test the limitations of the ECCC and GOSAT joint observation system towards constraining emissions by inventory sector and according to provincial boundaries. We demonstrate where the observation system succeeds in providing strong constraints on major emissions sources and quantify the information content of the system to understand the limitations for resolving all minor Canadian emissions.

2 Data and Methods

We use the GEOS-Chem CTM v12-03 (<http://acmg.seas.harvard.edu/geos/>) to simulate methane fields from 2010–2015 on a 2° x 2.5° global grid and compare to surface observations from the ECCC in situ GHG monitoring network and satellite observations from GOSAT within the Canadian domain. We test for bias in the global model representation of background methane using both surface and aircraft in situ data at Canada’s most westerly site, Estevan Point (ESP), ~~and~~ using global GOSAT data, and using global NOAA/HIPPO data. The sensitivity of simulated methane in Canada to the use of different wetlands flux parametrization is evaluated by comparing an ensemble of WetCHARTS v1.0 configurations to ECCC surface observations. The WetCHARTS ensemble mean ~~along-in addition to~~ other GEOS-Chem prior emissions are used in the Bayesian inverse analysis which optimizes Canadian sources using ECCC surface data and GOSAT satellite data independently for comparative analysis. We show the limitations of the observing system towards subnational level discretization by combining ECCC and GOSAT data in a joint-inversion. Here we describe the observations, the model, and the inverse analysis in further detail.

129 **2.1 Observations**

130 **2.1.1 In situ Surface Observations**

131 We use continuous measurements from eight sites in the ECCC greenhouse gas monitoring network from 2010–2015. Figure
132 1 shows a map of the sites and Table 1 provides a descriptive list. The eight sites are Estevan Point, British Columbia (ESP),
133 Lac La Biche, Alberta (LLB), East Trout Lake, Saskatchewan (ETL), Churchill, Manitoba (CHC), Fraserdale, Ontario
134 (FRA), Egbert, Ontario (EGB), Chibougamau, Quebec (CHM) and Sable Island, Nova Scotia (SBL). All sites use Picarro
135 cavity ring-down spectrometers (G1301, G2301 or G2401) measuring dry-air mole fractions of methane with hourly-average
136 precision better than 1 ppb. For model comparison the measurements are averaged over 4h from 12:00 to 16:00 local time,
137 ~~for~~ when the planetary boundary layer is well-mixed. The instruments are calibrated against World Meteorological
138 Organization (WMO) certified standard gases. The western-most site, ESP, measures methane continuously from a 40 m
139 tower at a lighthouse station on the west coast of Vancouver Island. ESP is surrounded by forests to the north, east, and south
140 and the Pacific Ocean to the west. ESP is used to evaluate boundary conditions and model bias in the methane background as
141 it is the least sensitive to Canadian emissions due to prevailing westerly winds. Sites LLB and ETL are the most sensitive to
142 anthropogenic emissions in Western Canada. LLB measures continuously from a 50 m tower located in a region of peatlands
143 and forest ~200 km NE of Edmonton and ~230 km S of Fort McMurray. ETL measures from a height of 105 m located ~150
144 km north of Prince Albert surrounded by Boreal forest. The sites in the Hudson Bay Lowlands (HBL) region, CHC and
145 FRA, are the most sensitive to natural ~~wetlands emissions~~wetland emissions as this area produces some of the largest
146 methane fluxes from wetlands in North America. CHC measures continuously from a 60 m tower in a small port town on the
147 western edge of Hudson Bay surrounded by flat tundra. FRA measures from a 40 m tower and is located on the southern
148 perimeter of James Bay surrounded by extensive wetlands coverage. The site CHM in Quebec is also sensitive to natural
149 ~~wetlands emissions~~wetland emissions and is excluded in the inverse analysis to be used to verify the posterior results. CHM
150 is substituted by Chapais, Quebec ~50 km away from 2011 onwards. The remaining Central and Atlantic Canada sites EGB
151 and SBL are sensitive to net outflow from Canadian sources, both natural and urban, and some emissions from the Eastern
152 United States. EGB is in a small rural village ~80 km north of Toronto and measures from a 25 m tower. SBL is on a remote
153 uninhabited island 275 km ESE of Halifax, Nova Scotia and measures from a height of 25 m.

154
155 **Table 1:** Descriptive list of ECCC in situ observation sites used in the analysis.
156

Site Code	Full Name, Province	Latitude	Longitude	Elevation (asl) /
				Sampling Height (agl) (m)
ESP	Estevan Point, British Columbia	49.4° N	126.5° W	7 / 40
LLB	Lac La Biche, Alberta	55.0° N	112.5° W	548 / 50
ETL	East Trout Lake, Saskatchewan	54.4° N	105.0° W	500 / 105

CHC	Churchill, Manitoba	58.7° N	93.8° W	16 / 60
FRA	Fraserdale, Ontario	49.8° N	81.5° W	210 / 40
EGB	Egbert, Ontario	44.2° N	79.8° W	225 / 25
SBL	Sable Island, Nova Scotia	43.9° N	60.0° W	2 / 25
CHM ^{*†}	Chibougamau, Quebec	49.7° N	74.3° W	383 / 30
CHA ^{*†}	Chapais, Quebec	49.8° N	75.0° W	381 / 30

*Chibougamau, Quebec is replaced by Chapais, Quebec ~50 km away from 2011 ~~onward~~^{to 2015}, overlapping in Fig.1

† Site is used to evaluate the posterior inversion results, and is not used in the inversion itself

2.1.2 GOSAT Satellite Observations

The Greenhouse Gas Observing Satellite (GOSAT) was launched in January 2009 by the Japan Aerospace Exploration Agency (JAXA). GOSAT is in a low-Earth polar sun-synchronous orbit with an equator overpass around 13:00 local time. The TANSO-FTS instrument on-board GOSAT retrieves column-averaged dry air mol fractions of methane using short-wave infrared (SWIR) solar backscatter in the 1.65 μm absorption band (Butz et al., 2011). Observation pixels in the default mode are 10 km in diameter separated by 260 km along the orbit track with repeated observations every 3 days. Target mode observations provide denser spatial coverage over areas of interest. There has been no observed degradation of GOSAT data quality since the beginning of data collection (Kuze et al., 2016). Here we use version 7 of the University of Leicester proxy methane retrieval over land from January 2010 to December 2015 (Parker et al., 2011, 2015; ESA CCI GHG project team, 2018). The single-observation precision of GOSAT XCH₄ data is 13 ppb, and the relative bias is 2 ppb when validated against the Total Column Carbon Observing Network (TCCON; Buchwitz et al., 2015). Figure 1 shows the GOSAT observations over Canada used in our analysis within the domain of 45° N–60° N latitude and 50° W–150° W longitude. The observations used have passed all quality assurance flags for a total of 45,936 observations from 2010–2015, or approximately ~7600 observations per year. Our analysis excludes glint data over oceans, and cloudy conditions are accounted for by the quality assurance flags. We avoid using data above 60° N latitude due to higher uncertainty in the satellite retrieval and the model comparison (Maasakkers et al., 2019; Turner et al., 2015).

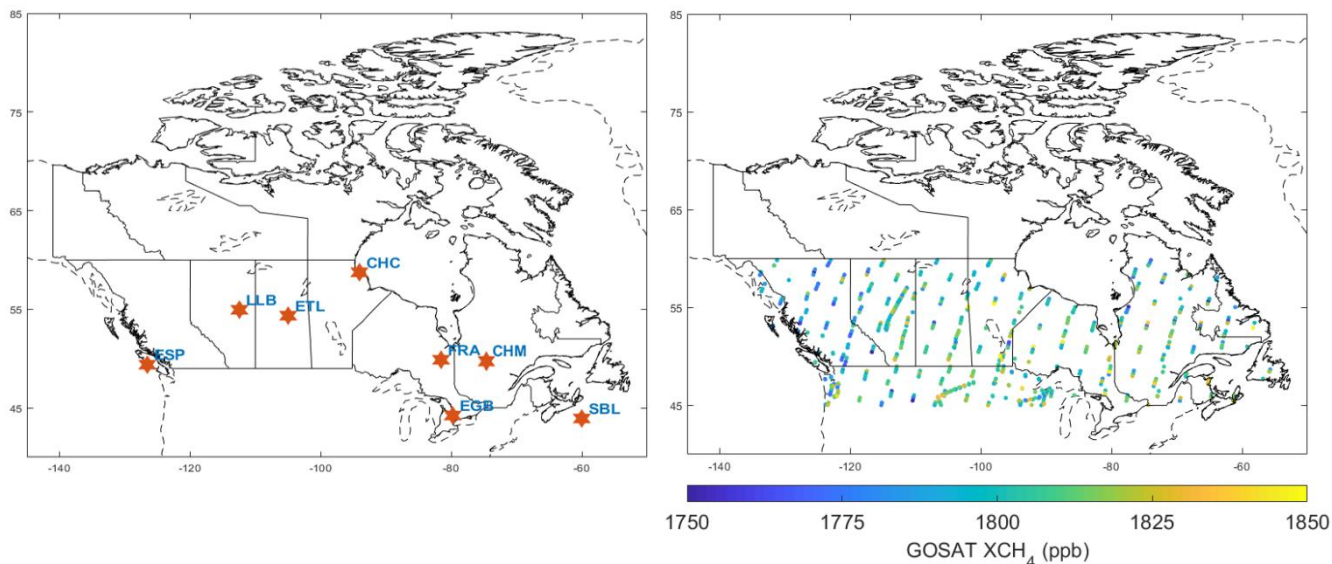


Figure 1: ECCC surface (left) and GOSAT satellite (right) observations used in the inverse analysis. A descriptive list of the ECCC sites is shown in Table 1. GOSAT data shown is from a single year in 2013 and is filtered to the Canadian domain within 45°N–60°N latitude and 50°W–150°W longitude. There are ~600 GOSAT observations per month in this domain with a minimum Nov–Jan (112–248) and maximum Jul–Sep (872–1098), individual months are shown in the Supplement (Fig. S1).

2.2 Forward Model

We use the GEOS-Chem CTM v12-03 at $2^\circ \times 2.5^\circ$ grid resolution driven by 2009–2015 MERRA-2 meteorological fields from the NASA Global Modeling and Assimilation Office (GMAO). Initial conditions from January 2009 are from a previous GOSAT inversion by Turner et al. (2015) which was shown to be unbiased globally when compared to surface and aircraft data. Bottom-up anthropogenic emissions in GEOS-Chem are from the 2013 ICF Canadian oil and gas inventory (Sheng et al., 2017) and the 2012 EDGAR v4.3.2 global inventory for other Canadian and global sources, and the gridded US 2012 EPA Inventory for the United States (Maasakkers et al., 2016). For wetlands, six configurations from the 2010–2015 extended ensemble of WetCHARTS (Bloom et al., 2017) are used in the ensemble forward model analysis (Section 3.12) and the ensemble mean is used as the prior for the inverse analysis (Sections 3.32–3.4). Figure 2 shows the spatial distribution of the prior methane emissions in Canada from the major anthropogenic and natural sources. The two largest sources are from the ICF oil and gas inventory, (Sheng et al., 2017) and ~~wetlands emissions~~ wetland emissions from the ensemble mean of the WetCHARTS inventory (Bloom et al., 2017), with significant emissions from livestock and waste emissions from EDGAR. Oil and gas are 54% of the anthropogenic total and wetlands are 94% of the natural total. The prior emissions estimates in this simulation are summarized in Table 2, which organizes emissions by Canadian source categories

198 and are compared to sector attribution in the National ~~GHG-Inventory Report~~ (Environment and Climate Change Canada,
199 2017). Our totals for Energy, Agriculture and Waste are 2.4, 1.0, and 0.9 Tg a⁻¹ respectively compared to 2.0, 1.2 and 0.9 Tg
200 a⁻¹ in the National Inventory. In the absence of a spatially disaggregated Canadian inventory for methane, we consider these
201 prior estimates reasonably similar for the purpose of comparing our posterior emissions to the National Inventory, however
202 we cannot compare the spatial pattern of emissions which ~~may will likely~~ show ~~less agreement~~ more discrepancies. Natural
203 emissions are divided into wetlands, which are 14.0 Tg a⁻¹ in the ensemble mean, and other natural sources, which are 0.8 Tg
204 a⁻¹ from biomass burning, seeps, and termites. Each component of other natural emissions has a separate spatially
205 disaggregated inventory as described in Maasakkers et al. (2019). Emissions from the United States and the rest of the world
206 are included in the model but not optimized in the inversions. Loss of methane from oxidation due to OH is computed using
207 archived 3-D monthly fields of OH from a previous GEOS-Chem full-chemistry simulation (Wecht et al., 2014).

208

209

210

211 **Table 2:** Mean 2010–2015 prior estimates of Canadian methane emissions used in GEOS-Chem arranged according to
212 categories in the National ~~GHG Emissions~~ Inventory (Environment and Climate Change Canada, 2017).

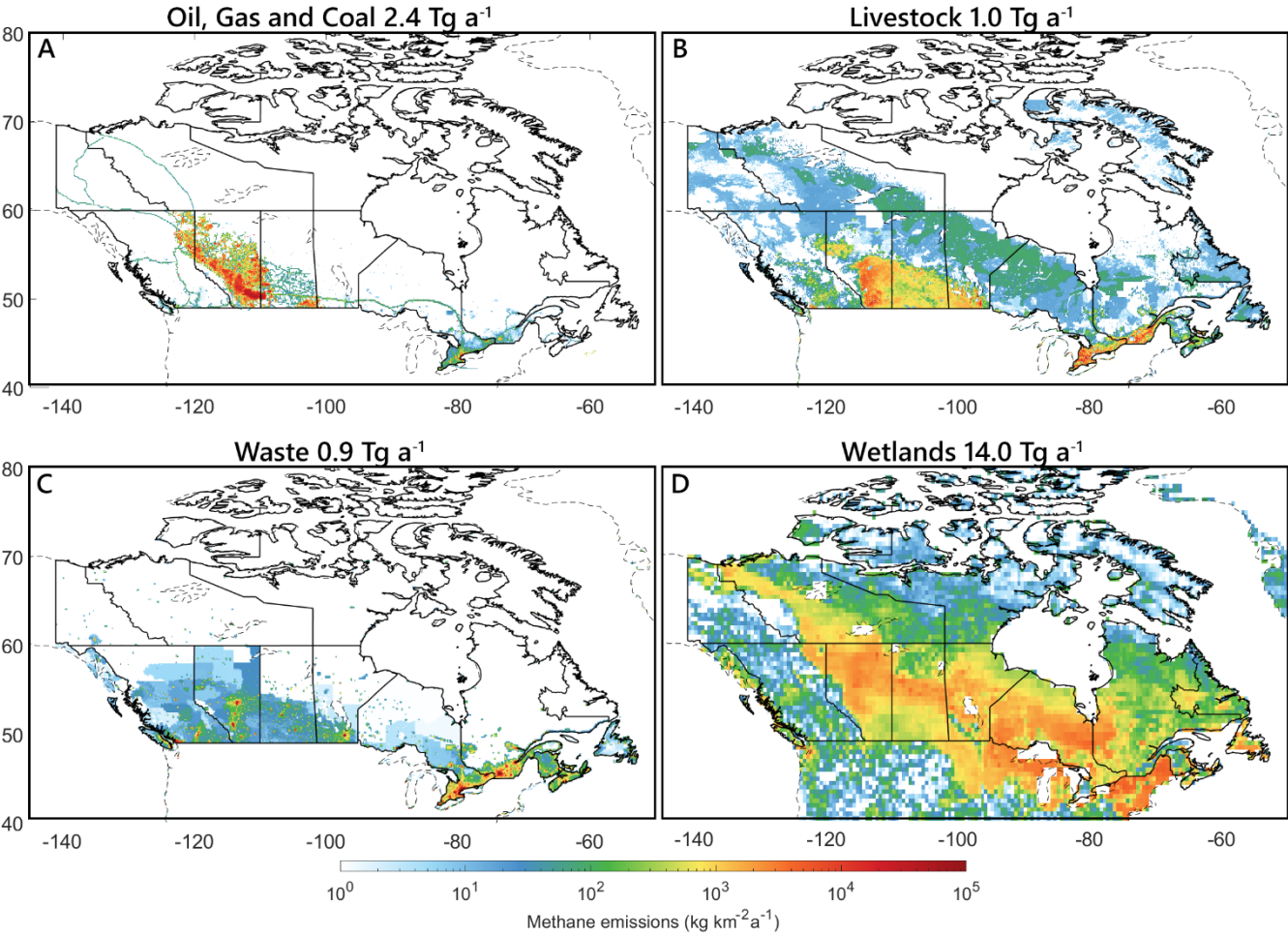
213

Category		Source Type ^a	Emissions (Tg a ⁻¹) ^a	Total (Tg a ⁻¹) ^a	Inventory (Tg a ⁻¹) ^b
Anthropogenic	Energy	Oil	0.52	2.42	2.00
		Gas	1.81		
		Coal	0.09		
	Agriculture	Livestock	1.00	1.00	1.20
	Waste	Landfills	0.66	0.94	0.92
		Wastewater	0.19		
		Other Anthropogenic	0.09		
Natural	Wetlands	-	14.0	14.0	-
	Other Natural	Biomass Burning	0.28	0.84	-
		Seeps	0.28		
		Termites	0.28		

214 ^aEmissions inputs for GEOS-Chem. These are shown for the individual source types and summed over the categories
215 Energy, Agriculture and Waste. In Canada, oil and gas are from Sheng et al. (2017), coal, livestock, landfills, wastewater and
216 other anthropogenic are from EDGAR v4.3.2, wetlands are from Bloom et al. (2017). Biomass burning is from QFED
217 (Darmenov and da Silva, 2013) and termite emissions are from Fung et al. (1991). Seeps and other global sources are

218 described in Maasakkers et al. (2019).
219

220 ^bEmissions from the National ~~GHG Emissions~~ Inventory (Environment and Climate Change Canada, 2017) that correspond
221 to the Energy, Agriculture and Waste categories. These are used in the discussion of results but are not included in the
222 inverse model.



223
224

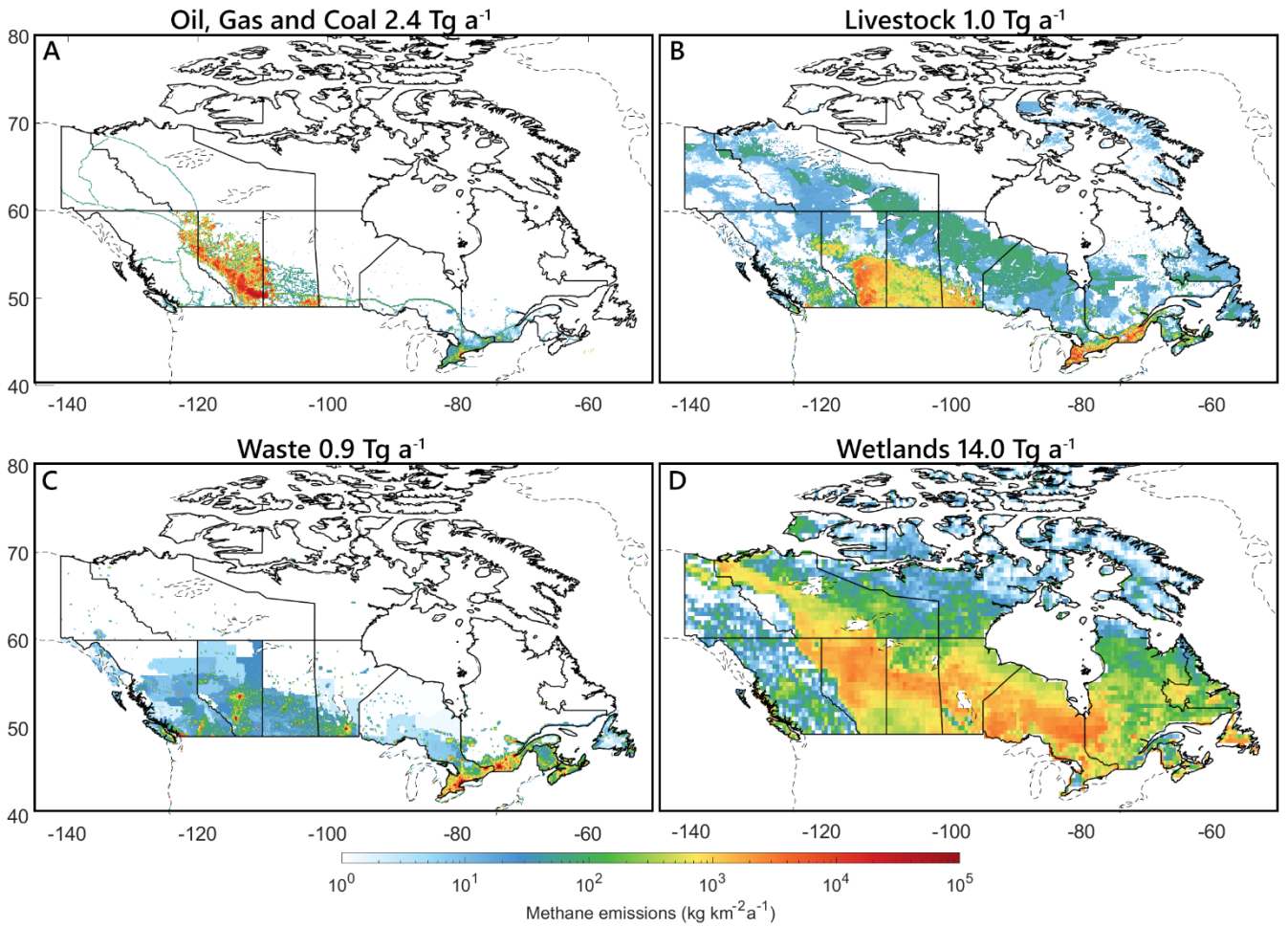


Figure 2: Prior estimates of anthropogenic and natural methane emissions. Colour bars are in log scale in units of $\text{kg CH}_4 \text{ km}^{-2} \text{a}^{-1}$. Most anthropogenic emissions fall under the energy category (A) which are oil and gas in the ICF inventory (Sheng et al., 2017) plus minor emissions from coal in EDGAR 4.3.2. Livestock (B) and waste (C) are from EDGAR. Natural emissions are primarily wetlands from the WetCHARTS inventory (D; Bloom et al., 2017).

2.3 Inverse Model Methodology

We optimize emissions in the inverse analysis by minimizing the Bayesian cost function $J(\mathbf{x})$ (Rodgers, 2000).

$$J(\mathbf{x}) = \frac{1}{2} (\mathbf{x} - \mathbf{x}_a)^T \mathbf{S}_a^{-1} (\mathbf{x} - \mathbf{x}_a) + \frac{1}{2} (\mathbf{y} - \mathbf{F}(\mathbf{x}))^T \mathbf{S}_o^{-1} (\mathbf{y} - \mathbf{F}(\mathbf{x})) \quad (1)$$

Where \mathbf{x} is the vector of emissions being optimized, \mathbf{x}_a is the vector of prior emissions (Table 2), $\mathbf{F}(\mathbf{x})$ is the simulation of methane concentrations corresponding to the observation vector \mathbf{y} of ECCO surface and/or GOSAT data. \mathbf{S}_a is the prior error covariance matrix and \mathbf{S}_o is the observational error covariance matrix. The observational error matrix includes both

instrument and model transport error. The GEOS-Chem model relating methane concentrations to emissions $F(\mathbf{x})$ is essentially linear and can be represented by the Jacobian matrix \mathbf{K} such that $F(\mathbf{x}) = \mathbf{K}\mathbf{x} + \mathbf{b}$, where \mathbf{b} is the model background. The background includes initial conditions from Turner et al. (2015) and methane from global emissions that are held constant in the inversion. Possible bias in the background is evaluated in detail in [the Supplement Section 3-1.3](#) and shown to be minimal. The \mathbf{K} matrix is of ~~m~~ by ~~n~~ size where n is the number of state vector elements being optimized and m is the number of ECCC surface and/or GOSAT observations being used. The \mathbf{K} matrix is constructed using the forward mode of GEOS-Chem and the tagged tracer output for Canadian sources which describes the sensitivity of concentrations to emissions dy/dx in ppb Tg⁻¹.

246

GEOS-Chem continuously simulates global emissions with a global source-sink imbalance of +13 Tg a⁻¹ in the budget as described in Maasakkers et al. (2019). We show in [Section 3-1.3 of the Supplement](#) that this configuration of the model reliably reproduces the global growth rate in atmospheric methane with adjustments only needed for 2014 and 2015 primarily due to differences in tropical wetland emissions (Maasakkers et al., 2019). [with reduced transport errors at the 2° × 2.5° resolution \(Stanevich et al., 2020\). This gives a well-represented background for methane which is tested using global GOSAT and NOAA data, as well as in situ data at Canadian background sites. We improve the model representation of methane using bias corrections which are discussed in Section 1.3 of the Supplement, and we show the consistency of the inversion results without adjustments to the model.](#) A high resolution inversion over North America over the 2010–2015 time-period using the same prior has shown adjustments to US emissions near the Canadian border are also relatively minimal, (Maasakkers et al., ~~2020~~2021), so we treat US emissions as constant. [The assumption of constant US emissions is tested in Section 1.3.2 of the Supplement by removing ECCC stations near the US border from the inversion, which show consistent results. This gives a well-represented background for methane which is checked using global GOSAT data and in situ data at Canadian background site ESP.](#) Hence, we can attribute the model-observation mismatch ($\mathbf{y} - F(\mathbf{x})$) using observations limited to Canada to Canadian emissions which are optimized in the inversion. [Here-In the main text](#) we show three inversions with a different number of state vector elements: a) the monthly inversion ($n = 78$) optimizes monthly natural emissions in Canada and yearly anthropogenic emissions from 2010–2015, b) the sectoral inversion ($n = 5$) optimizes emissions according to the major inventory categories in Table 2 ~~done~~ individually for each year, and c) the provincial inversion ($n = 16$) optimizes emissions according to subnational boundaries which is also repeated for each year. The monthly inversion provides [higher](#) temporal resolution [relative to the other approaches in this study](#) to constrain the seasonality of natural emissions, assuming the spatial distribution is correct. The sectoral inversion provides direct constraints on inventory categories, and the provincial inversion provides [relatively](#) higher spatial resolution for subnational attribution. Substituting $F(\mathbf{x}) = \mathbf{K}\mathbf{x}$ in eq. 1 and subtracting the background \mathbf{b} , the analytical solution of the cost function $dJ(\mathbf{x})/d\mathbf{x} = 0$ yields the optimal posterior solution $\hat{\mathbf{x}}$ (Rodgers, 2000):

270

$$\hat{\mathbf{x}} = \mathbf{x}_a + \mathbf{S}_a \mathbf{K}^T (\mathbf{K} \mathbf{S}_a \mathbf{K}^T + \mathbf{S}_o)^{-1} (\mathbf{y} - \mathbf{K} \mathbf{x}_a) \quad (2)$$

271

272

273 The analytical solution provides closed-form error characterization, such that the the posterior error covariance $\hat{\mathbf{S}}$ of the
 274 posterior solution $\hat{\mathbf{x}}$ is given by:

275

$$276 \quad \hat{\mathbf{S}} = (\mathbf{K}^T \mathbf{S}_o^{-1} \mathbf{K} + \mathbf{S}_a^{-1})^{-1} \quad (3)$$

277

278 The averaging kernel matrix \mathbf{A} is used to evaluate the surface and satellite observing systems and is given by:

279

$$280 \quad \mathbf{A} = \mathbf{I}_n - \hat{\mathbf{S}} \mathbf{S}_a^{-1} \quad (4)$$

281

282 where \mathbf{I}_n is the identity matrix of length n corresponding to the number of state vector elements. The averaging kernel matrix
 283 \mathbf{A} describes the sensitivity of the posterior solution $\hat{\mathbf{x}}$ to the true state \mathbf{x} ($\mathbf{A} = d\hat{\mathbf{x}}/d\mathbf{x}$). The trace of \mathbf{A} provides the degrees of
 284 freedom for signal (DOFS), which is the number of pieces of information of the state vector that is gained from the inversion
 285 ($\text{DOFS} \leq n$). The diagonal values of \mathbf{A} provide information on which Canadian state vector elements can be constrained by
 286 ECCC surface and GOSAT satellite observations above the noise, and higher DOFS closer to n correspond to better
 287 constrained sources in total. As a further diagnostic of the inversion we conduct a singular value decomposition of the
 288 prewhitened Jacobian $\tilde{\mathbf{K}} = \mathbf{S}_o^{-1/2} \mathbf{K} \mathbf{S}_a^{1/2}$ (Rodgers, 2000). The number of singular values greater than one is the effective rank
 289 of $\tilde{\mathbf{K}}$, which shows the independence of the state vector elements and the number of pieces of information above the noise
 290 that are resolved in the inversion (Heald et al., 2004). The comparison between this eigenanalysis and the DOFS are
 291 discussed in the Supplement Section 1.4 and is used to inform the limitations of the observation system.

292

293 We construct the prior error covariance matrix \mathbf{S}_a based on aggregated error estimates for source categories and regions. We
 294 use 50% error standard deviation for the aggregated anthropogenic emissions which includes the Sheng et al. (2017) oil and
 295 gas inventory and other EDGAR sources, 60% for ~~wetlands emissions~~ wetland emissions from the Bloom et al. (2017)
 296 WetCHARTS inventory and 100% for non-wetlands natural sources. We assume no correlation between state vector
 297 elements so that \mathbf{S}_a is diagonal. Anthropogenic emissions have been shown to be spatially uncorrelated (Maasakkers et al.,
 298 2016) however wetlands show spatial correlation (Bloom et al., 2017). Here we optimize broadly aggregated categories, so
 299 our method assumes the spatial pattern of each state vector element is correct, however correlations between state vector
 300 elements in the eigenanalysis are used to assess the limitations of source discretization in the observing systems.

301

302 We construct the diagonal observation error matrix \mathbf{S}_o which captures instrument and model error using the relative residual
 303 error method (Heald et al., 2004). In this approach the vector of observed-modelled differences $\Delta = y_{\text{GEOS-Chem}} - y_{\text{observations}}$ is
 304 calculated and the mean observed-modelled difference $\overline{\Delta} = \overline{y_{\text{GEOS-Chem}} - y_{\text{observations}}}$ is attributed to the emissions that will

be optimized. Hence, the standard deviation in the residual error $\Delta' = \Delta - \overline{\Delta}$ represents the observational error and is used as the diagonal elements of S_o . For our Canadian inversion we find positive model-observation biases in the warmer months (April to September) and negative biases in the colder months (October to March). We calculate the relative residual error for growing and non-growing seasons separately, such that Δ' is partitioned into Δ'_g (October to March) and Δ'_{ng} (April to September) which is then used to calculate the diagonal elements of S_o . For surface observations the mean observational error is 65 ppb. Since the instrument error is <1 ppb for afternoon mean methane measurements, the observational error is entirely attributed to transport and representation error of surface methane in the model grid pixels. For satellite observations the mean observational error is 16 ppb where the instrument error is 11 ppb, showing most of the observational error is from the instrument rather than the forward model representation of the total column. Column-averaged methane concentrations are less sensitive to surface emissions resulting in the lower model error (Lu et al., 2021).

In summary, the inverse model is designed to suit the objectives of this study, which are to: (1) optimize anthropogenic and natural emissions in Canada at the national-scale and (2) compare the results of inversions using surface and satellite observations, and (3) characterize the limitations of the observing system towards subnational-scale emissions discretization. The spatial and temporal resolution of the inversion is limited by the precision of GOSAT data, the precision of the model representation of surface methane for ECCC data, and the sparse coverage of both systems relative to the smaller magnitude of Canadian emissions. This simplified approach, where Canadian emissions are optimized using only observations in Canada, may be sensitive to errors in the global model that are projected onto the Canadian domain. This is minimized if errors in the regional representation of methane, which are corrected in the inversion, are much larger than errors in the background from the global model, or if the background methane is corrected using global observations outside of the Canadian domain. We show an analysis of the global model alongside sensitivity tests of the inversions in Section 1.3 of the Supplement which produce consistent results. Future studies may deploy a more sophisticated, high resolution inverse model that will match more sophisticated observations, which include an expanded ECCC surface network, as well as satellites with higher density (TROPOMI; Hu et al., 2018) or higher precision (GOSAT-2; Nakajima et al., 2017) observations outside of the years of this analysis.

3 Results and Discussion

3.1 Evaluation of Bias in the Global Model

~~The left panel of Figure 3 shows the comparison of monthly mean GEOS Chem surface methane concentrations and methane measured at the ECCC station ESP from 2009 to 2015. ESP is located at the west coast of Vancouver Island (Fig. 4); this site is used as an evaluation of background methane and tests the bias in the global model as it is the least sensitive to Canadian emissions due to westerly prevailing winds. The model reliably reproduces surface observations at this station and~~

the growth rate in background methane due to the source-sink imbalance of $+13 \text{ Tg a}^{-1}$ in the model global budget (Maasakkers et al., 2019) with a small mean model observation bias of 5.3 ppb. The right panel of Figure 3 shows the comparison of modelled methane to NOAA aircraft profiles at the same site. Aircraft profiles occur approximately once a month continuously over the study period. The data is not averaged here and is directly compared to GEOS-Chem simulated grid boxes at the pressure level of the measurement. The reduced major axis (RMA) regression shows a slope of 0.86 and a coefficient of regression $r^2 = 0.67$ which shows a reasonable model representation of the measurements. These statistics are consistent with previous inversions using GEOS-Chem that showed relatively unbiased conditions against NOAA surface stations globally (Turner et al., 2015; Maasakkers et al., 2019). A high resolution inversion over North America over the same 2010–2015 time period using the same prior have shown adjustments to US emissions near the Canadian border are relatively minimal (Maasakkers et al., 2020), so we treat US emissions as constant in the inversion. The acceptable reproducibility of background methane at this site allows us to attribute much larger differences observed at other sites, up to a maximum of $\sim 1000 \text{ ppb}$ in the summer (Figure 6), to Canadian emissions which are optimized using Canadian observations while holding other global emissions constant.

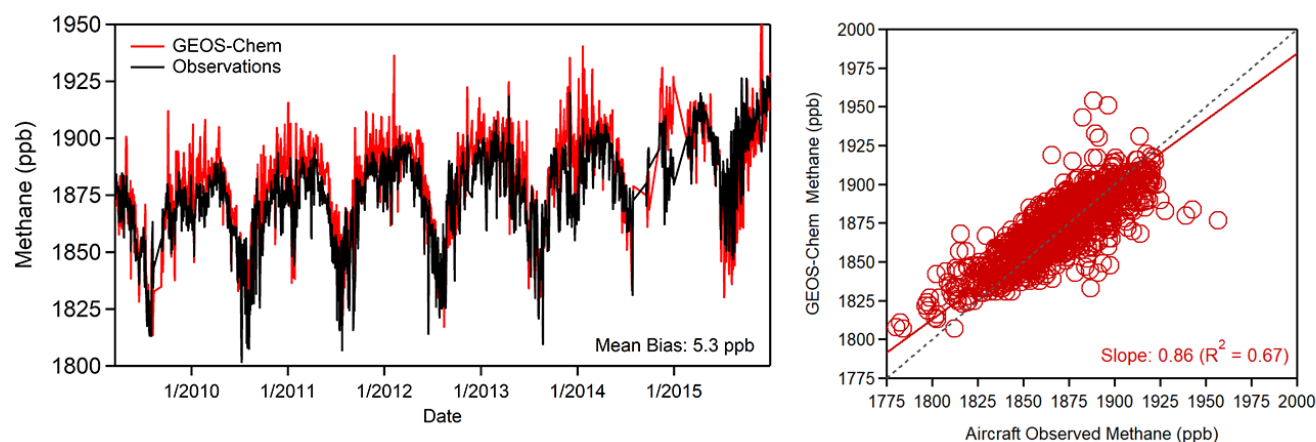


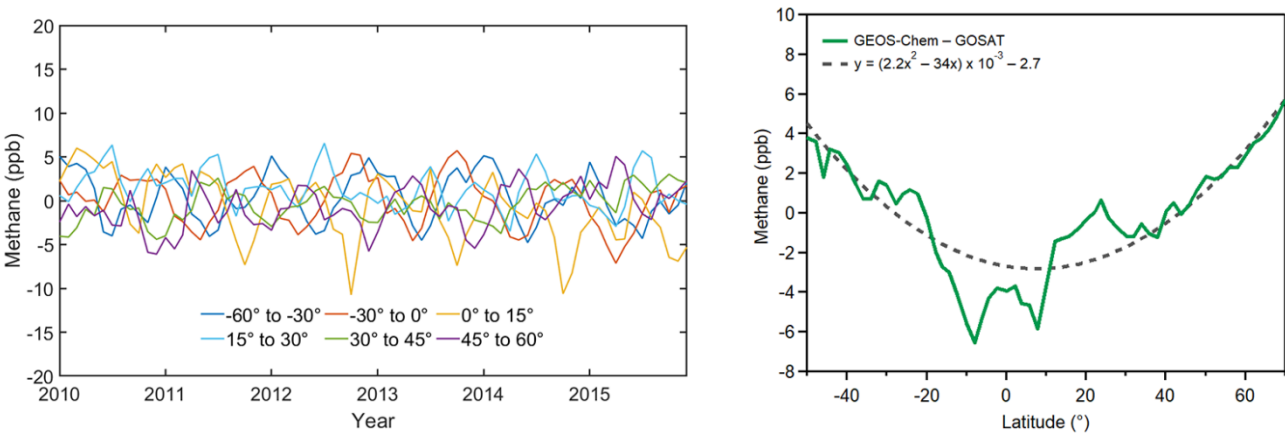
Figure 3: Time series comparison (left) from 2009–2015 of surface GEOS-Chem simulated methane (red) and measured in situ methane (black) at site ESP off the west coast of British Columbia. Comparison to NOAA aircraft profiles (right) from 2009–2015 at the same site using a reduced major axis (RMA) regression along with the 1:1 line (black).

The GEOS-Chem simulation of column averaged methane shows three global biases previously discussed in the literature: (1) a latitude dependent bias, (2) a seasonal bias and (3) a background change for 2014 and 2015 due to differences in the global source-sink imbalance in these two years (Turner et al., 2015; Saad et al., 2018; Maasakkers et al., 2019; Stanevich et al., 2019). We apply these corrections to the simulated column of methane on a global basis to produce an unbiased

background for our target Canadian domain (45° N to 60°N, 50° W to 150° W). The latitude-dependent bias (1) is likely due to excessive polar stratospheric transport (Stanevich et al., 2019). We correct for this bias by fitting the model GOSAT difference for global 2° × 2.5° grid cells according to a second-order polynomial as shown in Figure 4:

$$\xi = (2.2\theta^2 - 340) \times 10^{-3} - 2.7 \quad (5)$$

where ξ is the resulting bias correction in ppb and θ is latitude in degrees. The correction in this work for the latitude bins of our target domain (45° N to 60° N) is between 0.3 to 2.9 ppb. This correction is lower than what has been shown previously (Turner et al., 2015; Maasakkers et al., 2019) and we attribute this improvement to our use of a 2°x2.5° gridded simulation instead of a 4°x4.5° as recommended by Stanevich et al. (2019) to reduce transport errors. A seasonally oscillating bias (2) remains after this correction. The seasonal bias has an amplitude of ± 4 ppb with repeating maxima in June and minima in December. It is not clear whether this seasonal bias is due to emissions and/or transport errors. In our base case we remove the seasonal bias on a monthly basis following Maasakkers et al. (2019) and show a sensitivity test without the correction for our inversion of monthly natural emissions in Canada (Supplement 1.3). Inversion results using GOSAT data with and without bias corrections in the model simulation of total column methane do not show major differences (Fig. S3). These scenarios all show agreement with the posterior emissions adjustments determined using ECCC in situ data which is a useful benchmark since modelled methane at the surface is not subject to any bias corrections. The background change (3) that appears in the simulated methane column from 2014 onwards is corrected for in Maasakkers et al. (2019) by optimizing emissions, emissions trends and trends in OH using a global inversion. In that work correction factors do not appear over Canada and the United States that would significantly influence the global change in atmospheric methane, and the main adjustment in 2014 and 2015 were to tropical wetlands emissions and OH. Here we treat this as a background change and apply a uniform correction to the simulated column since emissions outside of Canada and changes in OH are treated as fixed in our Canada focused inversion. The background change (3) is 5 ppb in 2014 and 10 ppb in 2015. The right panel of Figure 4 shows the latitude dependent bias correction and the left panel shows the resulting global time series of GEOS-Chem total column methane from 2010–2015 after corrections are applied. The global GEOS-Chem–GOSAT differences in the methane column can be limited globally to within 10 ppb without including the seasonal bias correction, and within 5 ppb with its inclusion. This shows a steady background in methane for the entire time period from 2010–2015 so global emissions do not affect the optimization of Canadian emissions. While biases within 10 ppb have been treated as acceptable for methane inversions (Buchwitz et al., 2015), we evaluate our GOSAT inversion results against inversions with independent ECCC in situ measurements that do not require any bias corrections in the model (Section 3.3) to produce more robust emissions estimates.



393

394

395 **Figure 4:** Time series (left) from 2010–2015 of the difference between GEOS-Chem simulated total column methane and
396 GOSAT observations after applying bias corrections, showing a consistent global background for methane. Data used in the
397 inversion for Canada is from 45° N to 60° N (purple line) and shows acceptable differences within 5 ppb over the entire
398 global latitude band. To produce the left figure, the latitude-dependent bias (right) is shown with the polynomial correction
399 that is applied (gray dash) that is within a magnitude of 0.3 to 2.9 ppb for the same latitude.

400

401 **3.2.1 Evaluation of WetCHARTS Extended Ensemble for ~~Wetlands Emissions~~Wetland Emissions in Canada**

402 Wetlands are the largest methane source in Canada with uncertainties in the magnitude, seasonality, and spatial distribution
403 of emissions. Our inverse analysis constrains the magnitude and seasonality of emissions with observations. Ideally, the prior
404 emissions in the model should be the best possible representation of emissions to reduce error in the optimization problem
405 (Jacob et al., 2016). Table 2 shows 2010–2015 mean ~~wetlands emissions~~wetland emissions in Canada to be 14.0 Tg a⁻¹ from
406 the mean of the WetCHARTS v1.0 inventory (Bloom et al., 2017). These emissions are more than three times the total of
407 anthropogenic emissions 4.4 Tg a⁻¹. The much larger signal from ~~wetlands emissions~~wetland emissions poses a difficulty for
408 constraining anthropogenic emissions (Miller et al., 2014). In this section, we evaluate our use of the mean of the
409 WetCHARTS v1.0 extended ensemble by running a series of forward model runs using alternate ensemble members in
410 GEOS-Chem and comparing model output to ECCC in situ observations.

411

412 The WetCHARTS extended ensemble for 2010–2015 contains an uncertainty dataset of 18 possible global wetlands
413 configurations as described in Bloom et al. (2017). These depend on three processing parameters which are: three CH₄:C
414 temperature-dependent respiration fractions ($q_{10} = 1, 2, \text{ and } 3$; where 1 is the highest temperature dependency), two
415 inundation extent models (GLWD vs. GLOBCOVER; where GLWD corresponds to higher inundation in Canada) and three

416 global scaling factors for global emissions to amount to 124.5, 166 or 207.5 Tg CH₄ yr⁻¹ (3×2×3=18). We find using the
417 scaling factors corresponding to 124.5 and 207.5 Tg CH₄ yr⁻¹ within GEOS-Chem results in an imbalance in the global
418 budget beyond what is observed in our measurements and degrades the representation of background methane, so we limit
419 the extended ensemble to six members which depend on three temperature parameterizations and two inundation scenarios
420 (3×2=6). Figure 35 shows the magnitude and spatial distribution of ~~wetlands emissions~~ wetland emissions in the six
421 scenarios. The total ~~wetlands emissions~~ wetland emissions within Canada show nearly an order of magnitude difference
422 between ensemble members from 3.9 Tg a⁻¹ to 32.4 Tg a⁻¹. Compared to the rest of North America, Boreal Canada shows the
423 largest variability between ensemble members, with the Southeast United States as the second most uncertain (Sheng et al.,
424 2018b).

425
426 We use ECCC in situ observations to better constrain the range of wetlands methane emissions in the ensemble members.
427 All six configurations are used in GEOS-Chem to produce a series of forward model runs for a subrange of years between
428 2013–2015. Figure 64 shows GEOS-Chem simulated methane concentrations using the six WetCHARTS configurations
429 and compares them to four ECCC in situ measurement sites in Canada (LLB, ETL, FRA, EGB). This subset of available data
430 is representative of sites sensitive to both anthropogenic and natural emissions. Most of Canadian anthropogenic emissions
431 are from Western Canada (Fig. 2), which we use sites LLB and ETL to evaluate (Fig. 1), and a significant amount of
432 Canadian natural emissions are from regions surrounding the Hudson’s Bay Lowlands, which we use sites FRA and EGB to
433 evaluate. Methane concentrations from GEOS-Chem show large differences when compared to ECCC observations, ranging
434 from +1050 to –150 ppb. The boundary-condition site ESP (Fig. S3) showed a mean bias of 5.3 ppb for all of 2010–2015.
435 Since there is no similar mismatch in the global representation of methane, these biases up to 1050 ppb can therefore be
436 attributed to misrepresented local Canadian emissions plus associated transport and representation error. Two types of biases
437 with opposite signs appear from this comparison. The first type is a positive summertime bias where the modelled methane
438 concentrations significantly exceed the observations; this bias is more pronounced in sites FRA (Fig. 46-C) and EGB (Fig.
439 64-D), which are in Ontario and sensitive to the Hudson Bay Lowlands. The bias is also visible in the western sites LLB
440 (Fig. 64-A) and ETL (Fig. 64-B) to a lesser extent. As we use a smaller magnitude of wetlands methane emissions
441 corresponding to the ensemble members in Figure 53 (from 32.4 Tg a⁻¹ to 3.9 Tg a⁻¹), this summertime bias decreases
442 proportionately. Therefore, we can attribute these large positive summertime biases to growing season ~~wetlands~~
443 ~~emissions~~ wetland emissions that are overestimated in the process model configurations. The second type of bias is a year-
444 long negative bias that appears most in site LLB (Fig. 46-A) and is magnified with the use of lower-magnitude ~~wetlands~~
445 ~~emissions~~ wetland emissions. This suggests the presence of year-round anthropogenic emissions in Western Canada that are
446 underestimated in the prior, or that winter-time wetland emissions could also be underestimated in WetCHARTS due to the
447 lack of explicit soil water and temperature dependencies. The inverse modelling results in the next section attribute this bias
448 to anthropogenic emissions.

449

450 Miller et al. (2016) conducted a study constraining North American Boreal ~~wetlands emissions~~wetland emissions from the
 451 WETCHIMP inventory modelled in WRF-STILT by comparing to observations in 2008. Their study included the use of
 452 three of the ECCC stations described here (CHM, FRA and ETL). The model comparison to observations in that study
 453 showed a similar pattern of modelled methane exceeding observations in the summer and a low bias at ETL. They suggested
 454 ~~wetlands emissions~~wetland emissions were overestimated in most model configurations and that the wetlands bias may be
 455 masking underestimated anthropogenic emissions. These conclusions are corroborated by the 2013–2015 comparison shown
 456 here, we show high ~~wetlands emissions~~wetland emissions configurations in WetCHARTS produce a high bias that exceed
 457 measured summertime methane concentrations, and the use of lower wetlands configurations reveal a year-long low bias
 458 apparent in Western Canada. Our results suggest the combined use of higher inundation extent and lower temperature
 459 dependencies (GLWD and $q_{10} = 3$), or the use of lower inundation extent and higher temperature dependencies
 460 (GLOBCOVER and $q_{10} = 1$) best reproduce observations near the mean of the range of emissions, although the ensemble
 461 forward model analysis is unable to specify more detailed process model constraints.

462
 463 The forward model analysis in this section is a direct evaluation of wetlands configurations. This approach allows us
 464 *manually* tune wetlands scenarios and diagnose the sensitivity of the modelled-observed differences to the process modelling
 465 parameters. The inverse analysis shown subsequently is a statistical optimization that applies scaling factors to emissions
 466 based on the same model-observation differences. The inverse analysis can be viewed analogously as an *automatic* approach.
 467 These results show the challenge with optimizing Canadian methane emissions when ~~wetlands emissions~~wetland emissions
 468 are largely uncertain. Our approach of optimizing anthropogenic and natural emissions simultaneously in an inversion is
 469 useful because attempting to constrain either emissions category, anthropogenic or natural, obfuscates the analysis on the
 470 other. We exploit the different pattern of anthropogenic and natural emissions in time and space (Fig. 64). Natural emissions
 471 peak in the summertime and are concentrated in Boreal Canada, while anthropogenic emissions are persistent year-round and
 472 are concentrated in Western Canada (Fig. 2). Hence when optimizing the model-observation mismatch in a Bayesian inverse
 473 framework, some elements of the observation vector will correspond to high biases from summertime observations in Boreal
 474 Canada and some elements will correspond to low biases in Western Canada. As the choice of prior for the inversion we use
 475 the mean of the WetCHARTS configurations (14.0 Tg a^{-1}) which corresponds to the middle of the range shown shaded in red
 476 in Figure 64. The 60% range of uncertainty in the prior error covariance matrix \mathbf{S}_a appropriately excludes the extreme
 477 scenarios in Fig. 5-3 and 64.

478

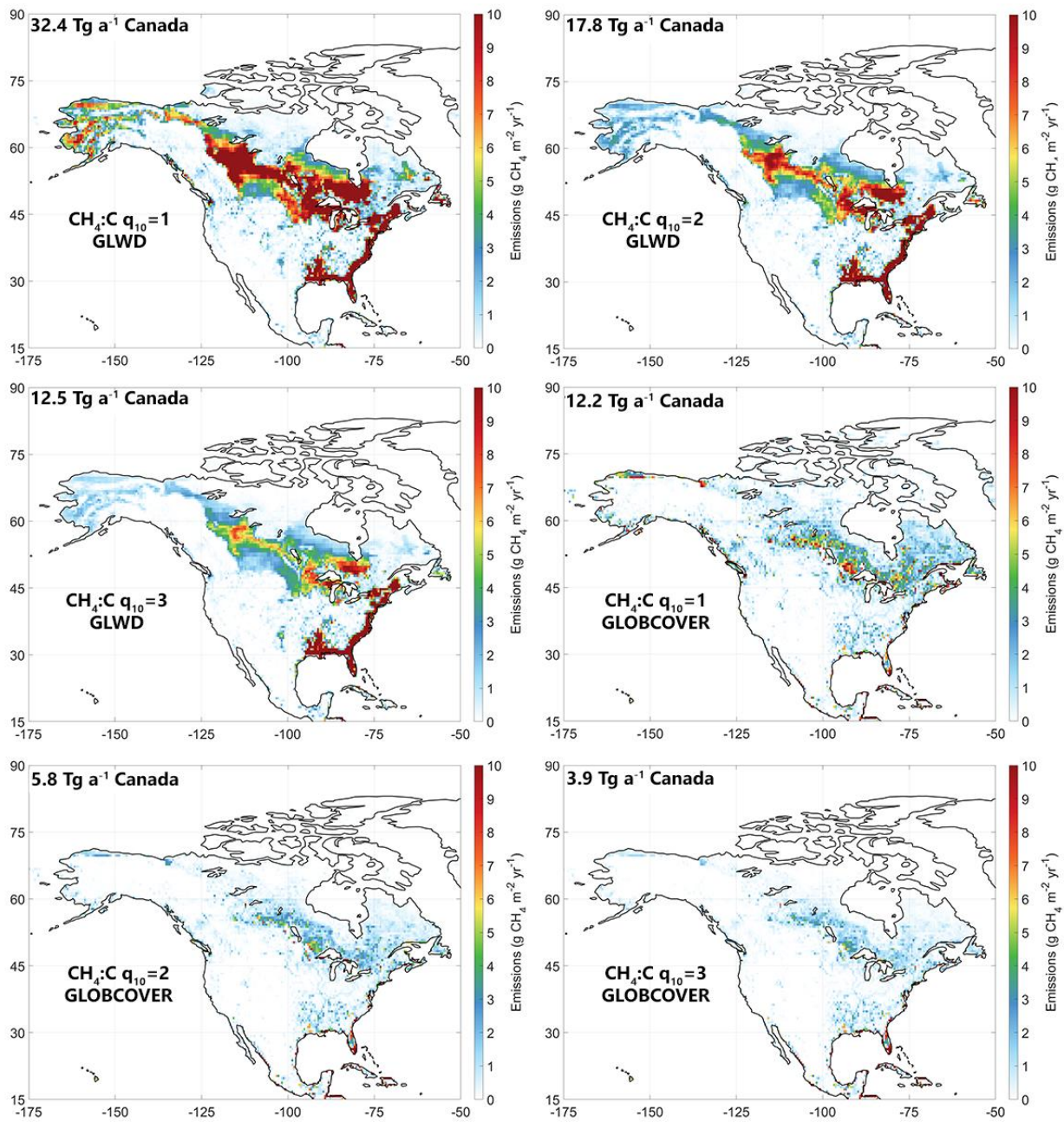


Figure 35: Ensemble members from the WetCHARTS v1.0 inventory (Bloom et al., 2017) with totals for wetland methane emissions within Canada for each configuration shown in $\text{Tg CH}_4 \text{ a}^{-1}$. Ensemble members vary according to the use of three $\text{CH}_4:\text{C } q_{10}$ temperature dependencies and two inundation extent scenarios (GLWD vs. GLOBCOVER) for $3 \times 2 = 6$ scenarios.

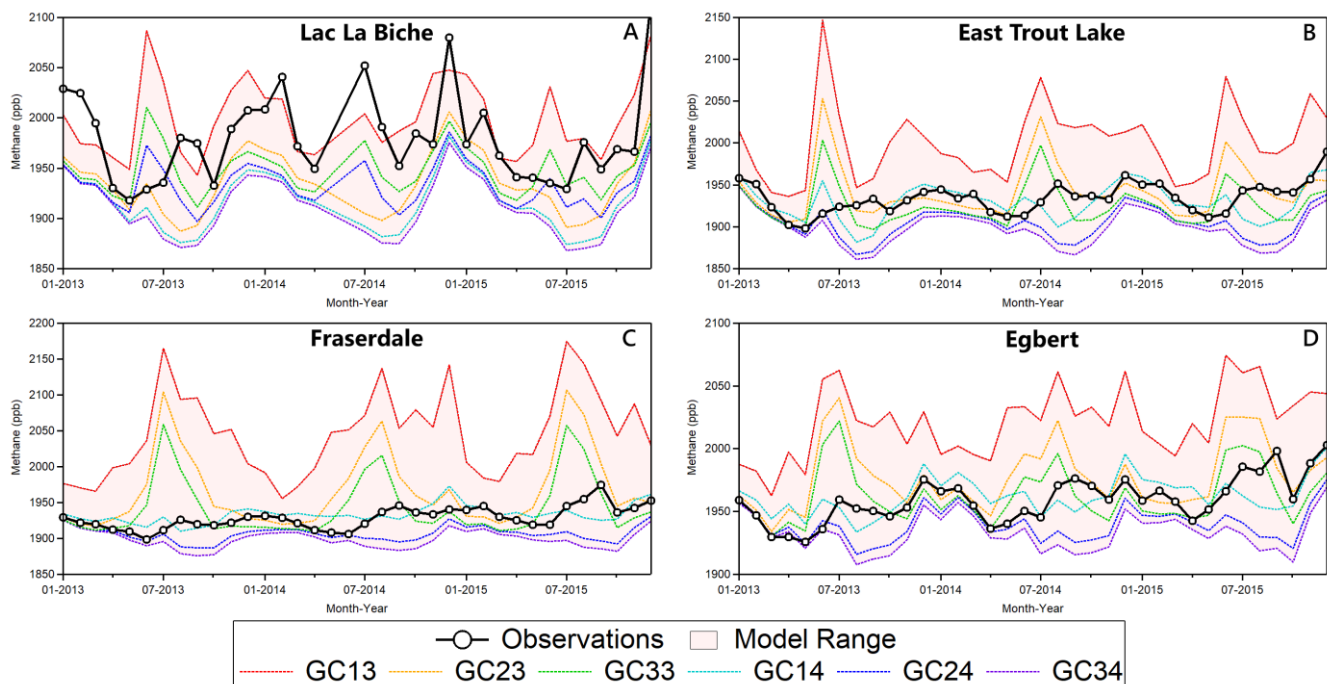


Figure 46: Time series of 2013–2015 modelled and observed methane concentrations. Monthly-mean methane from ECCC in situ observations (black) are shown and compared to six GEOS-Chem simulations differing in the use of WetCHARTS ensemble members for ~~wetlands emissions~~ wetland emissions, with other emissions corresponding to Table 2. The six configurations are labelled GCXY where first digit (X=1,2,3) corresponds to the $\text{CH}_4:\text{C}_{\text{q10}}$ temperature dependency, which decreases the sensitivity of emissions to temperature with increasing value. The second digit (Y=3,4) corresponds to the model used for inundation extent (3 = GLWD, 4 = GLOBCOVER) where GLOBCOVER produces lower emissions in Canada. Emissions configurations are those shown in Fig. 5-3 in order of magnitude from red to purple lines, with the shaded red showing the range of concentrations. Sites are LLB, Alberta (A), ETL, Saskatchewan (B), FRA, Northern Ontario (C) and EGB, Southern Ontario (D).

504 **3.23 Comparative ~~analysis~~ Analysis of ~~inversions~~ Inversions using ECCC in situ and GOSAT ~~satellite~~ Satellite** 505 **~~data~~ Data**

506 We optimize 2010–2015 emissions in Canada using an $n = 78$ state vector element inversion setup with GOSAT and ECCC
 507 data independently. Elements 1–72 of the inversion are monthly total natural emissions (wetlands + other natural) from
 508 2010–2015 and elements 73–78 are yearly total anthropogenic emissions (energy + agriculture + waste) for the same years.
 509 These categories correspond to the emissions shown in Table 2. We do not optimize emissions according to clustered grid
 510 boxes like other satellite inversions using GEOS-Chem (Wecht et al., 2014; Turner et al., 2015; Maasakkers et al., 2019) and
 511 instead scale the amplitudes of these two aggregated categories. This approach is a trade-off of time for space, due to the
 512 limitations of the observations, giving up finer spatial resolution for finer temporal resolution. This is useful for optimizing
 513 Canadian methane emissions since a) anthropogenic emissions are largely concentrated in Western Canada and require less
 514 spatial discretization over the entire country and b) natural emissions are the largest source and have an uncertain seasonality
 515 – as shown in the previous section – and require finer temporal discretization. The limitations of this method are that natural
 516 emissions are very unlikely to be spatially homogenous and vary due to hydrological differences even at the
 517 microtopographic level (Bubier et al., 1993). Perfectly resolving Canadian emissions sources in time and space is challenged
 518 by the sparsity and precision of the observing system and the model representation of the observations. We show the
 519 limitations of the combined ECCC and GOSAT observing system towards resolving subnational emissions in more detail in
 520 the subsequent section.

521

522 Figure 7-5 (top) shows 2010–2015 posterior emissions using this 78 state vector approach with ECCC in situ data (blue) and
 523 GOSAT satellite data (green). Error bars are from the diagonal elements of the posterior error covariance matrix $\hat{\mathbf{S}}$. Posterior
 524 anthropogenic emissions averaged over the 6 year period are $6.0 \pm 0.4 \text{ Tg a}^{-1}$ (1σ year-to-year variability) using ECCC data
 525 and $6.5 \pm 0.7 \text{ Tg a}^{-1}$ using GOSAT data. Posterior estimates are 36% and 48% higher than the prior of 4.4 Tg a^{-1} for ECCC
 526 and GOSAT results, respectively. There does not appear to be a significant year-to-year trend above the noise for the
 527 anthropogenic emissions optimized by either dataset. The posterior anthropogenic emissions using ECCC and GOSAT data
 528 show agreement with each other in each year but 2011, where the GOSAT derived emissions are statistically higher. The
 529 error from the diagonal of the posterior error covariance matrix $\hat{\mathbf{S}}$ may be overly optimistic, particularly for GOSAT data.
 530 This is due to the observational error covariance matrix \mathbf{S}_o being treated as diagonal when realistically there are correlations
 531 between GOSAT observations that are difficult to quantify (Heald et al., 2004). Our results for anthropogenic emissions
 532 show agreement with top-down aircraft estimates of methane emissions in Alberta that are higher than bottom-up inventories
 533 (Johnson et al., 2017; Baray et al., 2018) and previous satellite inverse-modelling studies over North America that upscale
 534 emissions in Western Canada (Turner et al., 2015; Maasakkers et al., 2019; Maasakkers et al., ~~2020~~2021; Lu et al., 20210).

535 We show source attribution through a sectoral and subnational scale analysis of anthropogenic emissions in the subsequent
536 section.

537

538 Inversion results for monthly natural emissions from 2010–2015 are also shown in Figure 7-5 (bottom). The total of posterior
539 natural emissions averaged over the 6 year period is 10.5 ± 1.6 Tg a⁻¹ using ECCC data and 11.7 ± 1.2 Tg a⁻¹ using
540 GOSAT data. The prior for natural emissions is 14.8 Tg a⁻¹ from the mean of the WetCHARTS extended ensemble (14.0 Tg
541 a⁻¹) plus other natural (biomass burning + termites + seeps = 0.8 Tg a⁻¹). There is some interannual variability in the prior due
542 to higher emissions in 2010 and 2015. Posterior results averaged over the six years are 29% lower than the prior using
543 ECCC data and 21% lower using GOSAT data, with both posterior results showing agreement with each other. These results
544 are within the uncertainty range of the WetCHARTS extended ensemble, and we show the magnitude of emissions from the
545 larger uncertainty dataset (3.9 to 32.4 Tg a⁻¹) can be better constrained with both ECCC and GOSAT observations.

546

547 While our results show lower natural emissions in all years, a linear fit to the posterior annual emissions using ECCC data
548 shows a trend of increasing natural emissions at a rate of ~ 0.56 Tg a⁻¹ per year from 2010–2015. The posterior with
549 GOSAT data does not corroborate this result, the overall emissions trend using GOSAT data is not robust and shows a
550 decreasing trend of ~ 0.2 Tg a⁻¹ per year. The lack of corroboration of trends between ECCC and GOSAT data may be
551 reflective of the lower overall sensitivity of total column methane to these surface fluxes (Sheng et al., 2017; Lu et al.,
552 2021) or the inability of this inverse system to constrain trends sufficiently. The combined ECCC+GOSAT inversion using
553 this setup is consistent with the results of the individual inversions, it is shown in the Supplement (Fig SXXS11) while the
554 intercomparison is emphasized here, although we note the combined inversion also does not corroborate this trend. We
555 evaluate the possible influence of errors in the global model on the projection of a trend onto the ECCC inversion in Section
556 1.3.2 of the Supplement. While the mean natural emissions over 2010–2015 show consistent results in the sensitivity tests,
557 the limitations of the observation system, the inversion procedure and the timescale of the analysis limit the interpretation of
558 trends. Poulter et al. (2017) estimated global ~~wetlands emissions~~ wetland emissions using biogeochemical process models
559 constrained by inundation and wetlands extend data. They estimated mean annual emissions over all of Boreal North
560 America to be 25.1 ± 11.3 Tg a⁻¹ in 2000–2006, 26.1 ± 11.8 Tg a⁻¹ in 2007–2012 and 27.1 ± 12.5 Tg a⁻¹ which suggests a
561 small increasing trend. Observational constraints over longer timescales are necessary to investigate the possibility of trends
562 in Canadian natural methane emissions. Improvements to the observation network and a better understanding of climate
563 sensitivity in WetCHARTS are necessary to understand how wetlands methane emissions will evolve in future climates.

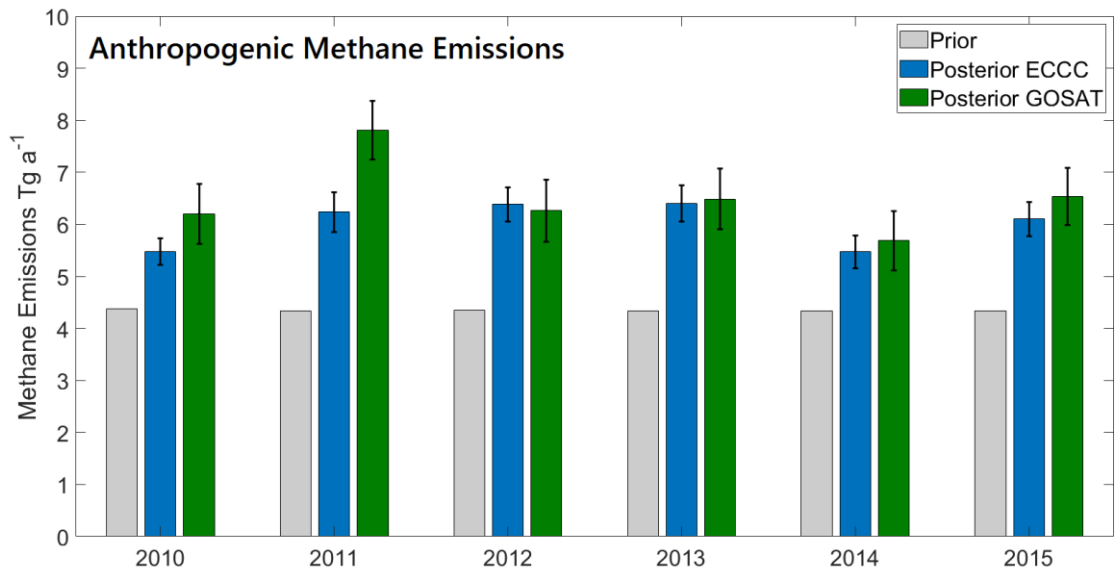
564

565 Figure 8-6 shows the 2010–2015 average seasonal pattern of natural emissions in the prior and posterior results. The
566 seasonality of natural methane emissions in the prior shows a sharp peak in July with a narrow methanogenic growing
567 season. The posterior with ECCC data shows a peak 1-month later in August in most years instead of July, with lower than
568 prior emissions in the spring months before the peak (March to May) and similar emissions to the prior in the autumn

569 months after the peak (September to November). Posterior emissions with GOSAT show a peak in July and corroborates the
 570 pattern of slower-to-begin spring emissions and the lower intensity summer peak seen from the ECCC inversion. The
 571 posterior results show the seasonality of emissions is not symmetrical around the temperature peak in July. August emissions
 572 are higher than June, September emissions are higher than May, and October emissions are higher than April. This pattern
 573 around July is present in the prior emissions from WetCHARTS, however the inversion results constrained by ECCC or
 574 GOSAT observations intensify the relative difference between emissions before and after July. Miller et al. (2016) found a
 575 similar seasonal pattern of emissions in the Hudson Bay Lowlands using an inverse model constrained by 2007–2008 in situ
 576 data. They found a less narrow and less intense peak of summertime emissions with higher autumn over spring emissions.
 577 Warwick et al. (2016) used a forward model and isotopic measurements of $\delta^{13}\text{C}\text{-CH}_4$ and $\delta\text{D}\text{-CH}_4$ from 2005–2009 to show
 578 northern ~~wetlands emissions~~wetland emissions should peak in August-September with a later spring kick-off and later
 579 autumn decline. This is further corroborated by Arctic methane measurements (Thonat et al., 2017) and high latitude eddy
 580 covariance measurements (Peltola et al., 2019; Treat et al., 2018; Zona et al., 2016) that show a larger contribution from the
 581 nongrowing season. Our inverse model results using ECCC and GOSAT data both show agreement with slower to start
 582 emissions in the spring and a less intense summertime peak for Canadian ~~wetlands emissions~~wetland emissions.
 583
 584 Several mechanisms have been proposed to describe a larger relative contribution from cold season methane emissions.
 585 Pickett-Heaps et al. (2011) attributed a delayed spring onset in the HBL to the suppression of emissions by snow cover. The
 586 temperature dependency in WetCHARTS is based on surface skin temperature (Bloom et al., 2017), however subsurface soil
 587 temperatures may continue to sustain methane emissions while the surface is below freezing. When subsurface soil
 588 temperatures are near 0°C, this “zero curtain” period can further continue to release methane for an extended period (Zona et
 589 al., 2016). Subsurface soils may remain unfrozen at a depth of 40 cm even until December (Miller et al., 2016).
 590 Alternatively, field studies in the 1990’s suggested the seasonality of emissions may be more influenced by hydrology than
 591 temperature, with large differences between peatlands sites (Moore et al., 1994). The WetCHARTS extended ensemble
 592 inundation extent variable is constrained seasonally by precipitation. While this does not directly constrain water table depth
 593 and wetland extent it provides an aggregate constraint on hydrological variability (Bloom et al., 2017). We show the mean
 594 seasonal pattern of both air temperature and precipitation from climatological measurements in subarctic Canada are
 595 similarly asymmetrical about the July peak (Fig. S2 in the Supplement). August is warmer and wetter than June, September
 596 is warmer and wetter than May, and October is wetter and warmer than April – with wetness being more persistent into the
 597 autumn than air temperature. Our inversion results showing a delayed spring start in the seasonal pattern of natural methane
 598 emissions in Canada may suggest a lag in the response of methane emissions to temperature and precipitation. This may be
 599 due to lingering subsurface soil temperatures and/or more complex parametrization necessary for hydrology.
 600
 601 The overall agreement between ECCC and GOSAT inversions shows robustness in the results. While the same model, prior
 602 emissions and inversion procedure are used for assimilating ECCC and GOSAT data, the two datasets are produced with

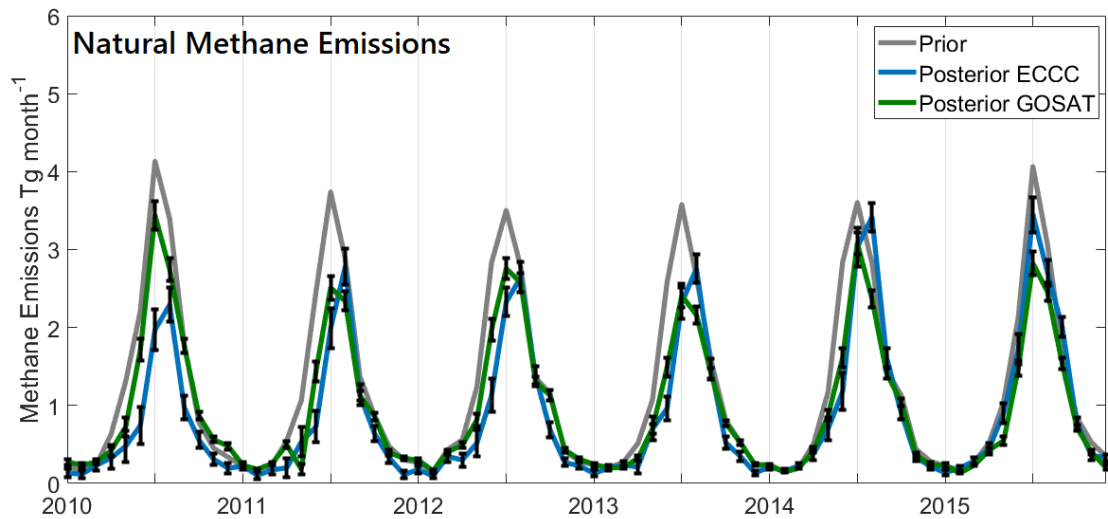
603 very different measurement methodologies (in situ vs. remote sensing) and sample different parts of the atmosphere (surface
604 concentrations or the total vertical column). The posterior error intervals shown from \hat{S} reflect assumptions about the
605 treatment of observations and may insufficiently account for correlations, however the comparative analysis provides a
606 useful sensitivity test of the posterior emissions since the datasets reflect different treatment of these assumptions.

607



608

609



610

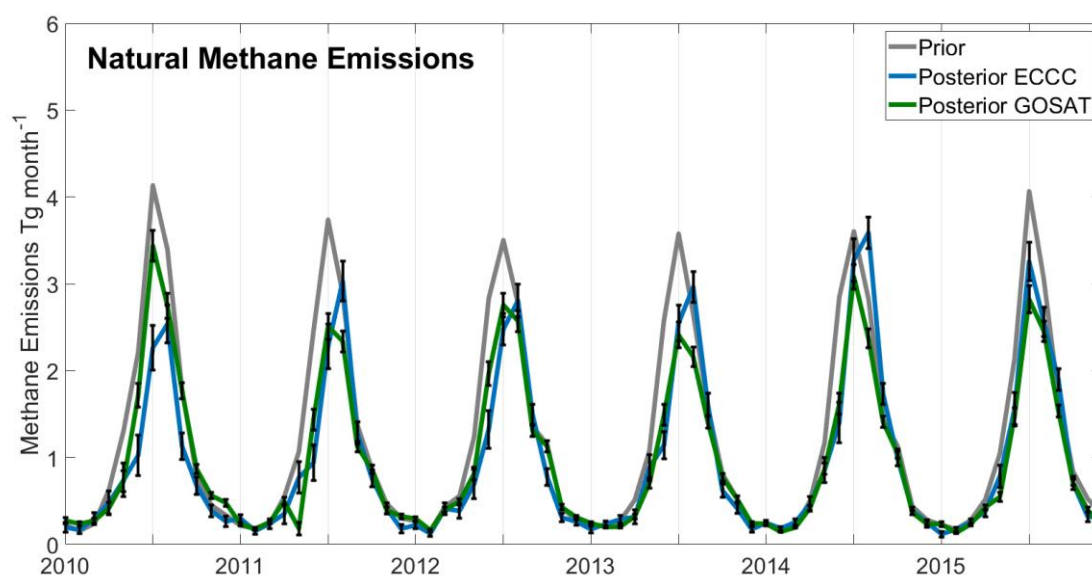
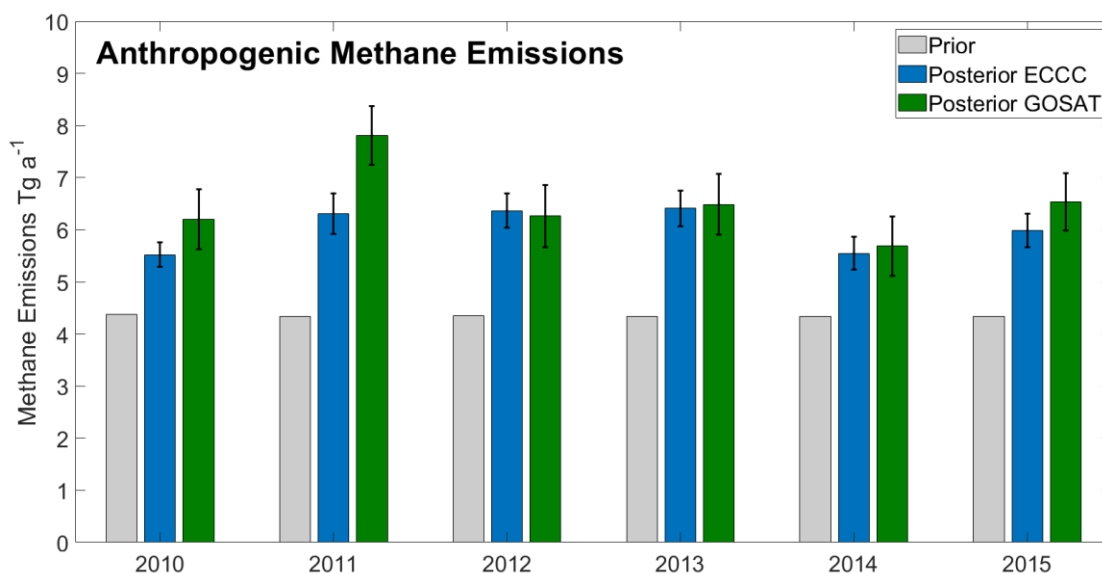
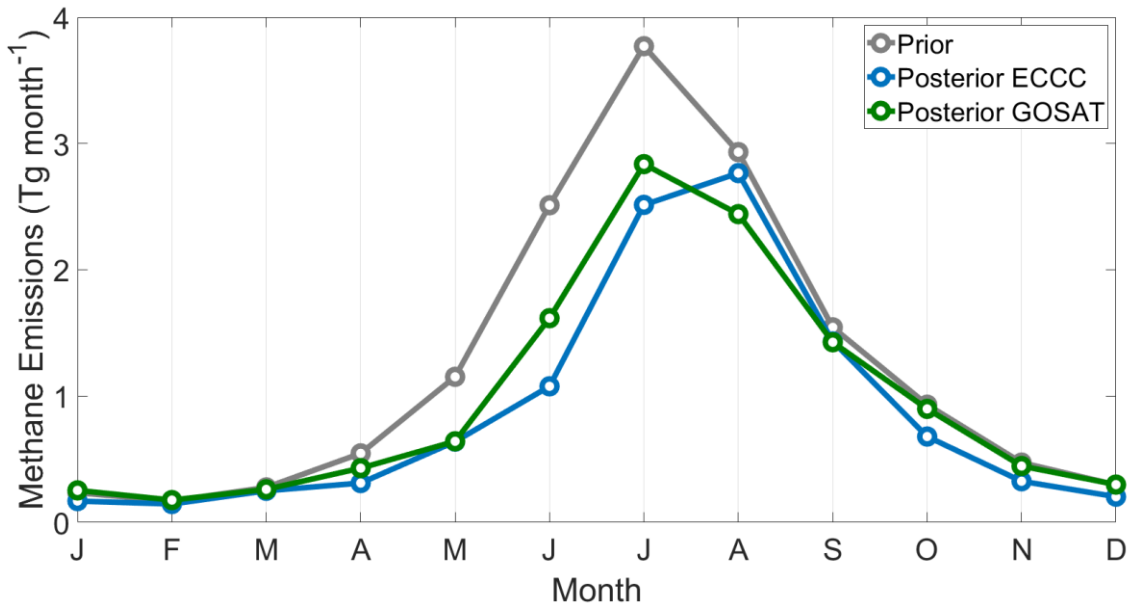
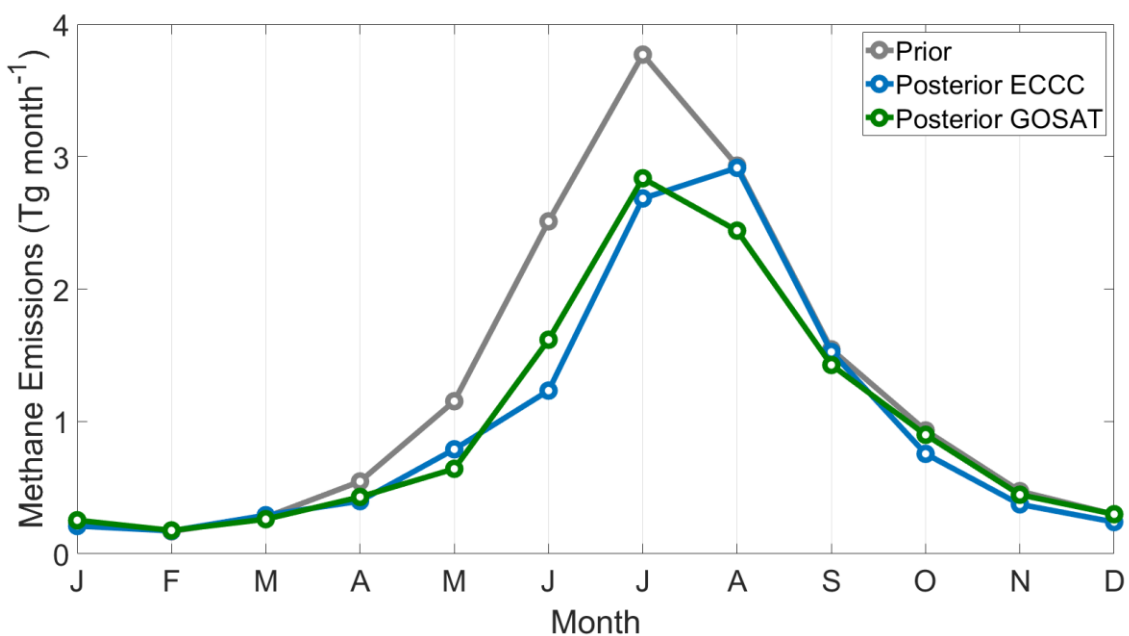


Figure 57: Comparative analysis of inversion results optimizing annual total Canadian anthropogenic emissions (top) and monthly total natural emissions (bottom) in an $n = 78$ state-vector element setup. The posterior emissions determined using ECCC in situ (blue) and GOSAT satellite (green) data are compared to the prior (gray). Error bars are from the diagonal elements of the posterior error covariance matrix.

618
619
620



621



622

623 **Figure 68:** Mean 2010–2015 seasonal pattern of natural methane emissions in Tg month⁻¹. The annual total emissions are
624 14.8 Tg a⁻¹ (prior, gray), ~~10.5~~11.6 ± 1.92 Tg a⁻¹ (posterior ECCC, blue) and 11.7 ± 1.2 Tg a⁻¹ (posterior GOSAT, green). The

625 posterior results are within the uncertainty range provided by the WetCHARTS extended ensemble (3.9–32.4 Tg a⁻¹ for
626 Canada).

627

628 **3.34 Joint-inversions ~~combining~~ Combining ECCC ~~in~~ In situ and GOSAT ~~satellite~~ Satellite data>Data**

629 We combine the ECCC and GOSAT datasets in two policy-themed inversions: (1) optimizing emissions according to the
630 sectors in the national inventory ($n = 5$ state vector elements; corresponding to the categories in Table 2) and (2) optimizing
631 emissions by provinces split into anthropogenic and natural totals ($n = 16$) and show the results in Figure 97. These
632 inversions are under-determined and show the limitations of the ECCC+GOSAT observing system towards constraining ~~very~~
633 ~~small-magnitude~~ emissions in Canada with very small magnitudes. We conduct the inversions for each year from 2010–2015
634 individually and present the average from these six samples. Since these two policy inversions use a low number of state
635 vector elements, they are vulnerable to both aggregation error and overfitting of the well-constrained state vector elements
636 and do not necessarily benefit from using a larger data vector from all six years. We discuss the diagnostics and information
637 content for these inversions in detail in Section 1.4 of the Supplement. The error bars are the 1 σ standard deviation of the six
638 yearly results and therefore represent both noise in the inversion procedure and year-to-year differences in the state
639 (emissions and/or transport). Here we do not apply a weighting factor to either dataset, the observations are treated
640 equivalently for the cost function in eq. (1). While there are about 5 times more GOSAT observations than ECCC
641 observations for use in the analysis and the in-situ observations have larger observational error in S_a (due to model error), the
642 surface measurements are much more sensitive to surface fluxes, which offsets the weight of the larger amount of GOSAT
643 data~~While there are about 5 times more GOSAT observations than ECCC observations for use in our analysis, the in-situ~~
644 ~~observations have larger observational error in S_a (due to model error) are much more sensitive to surface fluxes which offset~~
645 ~~overweighing the larger amount of GOSAT data~~. As further diagnostics we show the inversions using GOSAT and ECCC
646 individually (Table S43 and S54) which show general agreement between the datasets. We also use a singular value
647 decomposition eigenanalysis (Heald et al., 2004) to evaluate the independence of the state vector elements and to
648 demonstrate which sectoral categories and provinces can be reliably constrained above the noise in the system (Fig. S94 and
649 S105 in the Supplement).

650

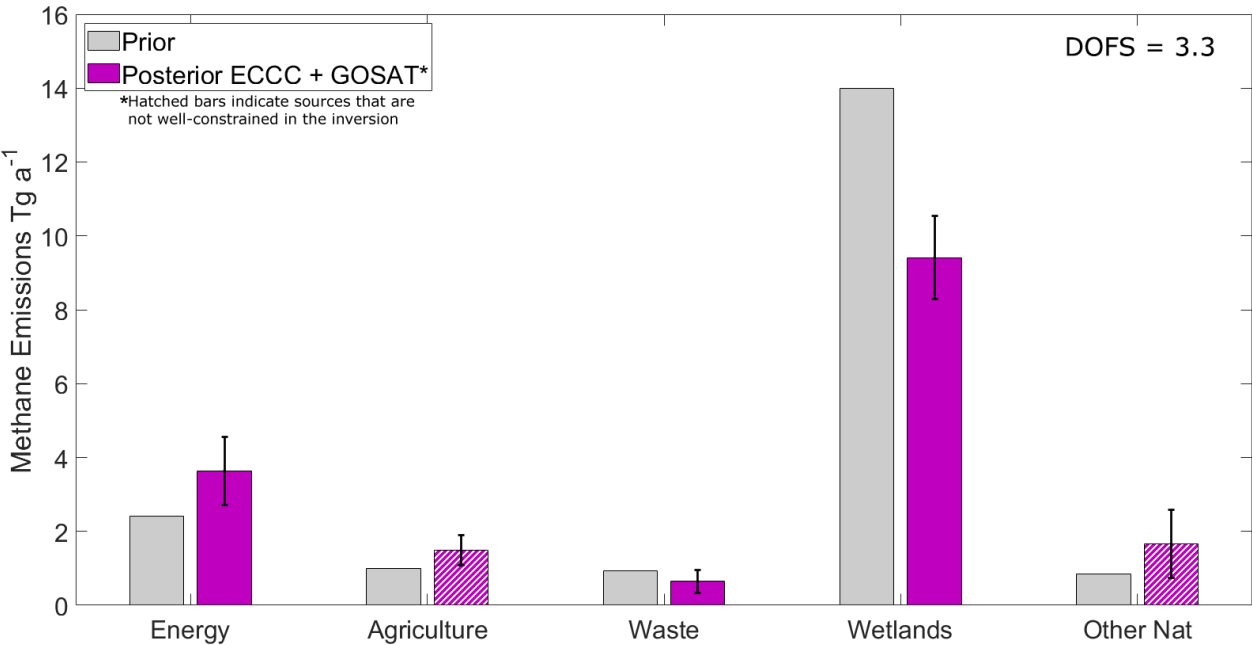
651 Figure 9-7 (top) shows the sectoral inversion corresponding to categories in the ~~N~~ational ~~I~~nventry (Table 2). The prior
652 emissions with 50% error estimates (60% for wetlands) are 2.4 Tg a⁻¹ (Energy), 1.0 Tg a⁻¹ (Agriculture), 0.9 Tg a⁻¹ (Waste),
653 14.0 Tg a⁻¹ (Wetlands) and 0.8 Tg a⁻¹ (Other Natural). The posterior emissions are 3.6 ± 0.9 Tg a⁻¹ (Energy), 1.5 ± 0.4 Tg a⁻¹
654 (Agriculture), ~~0.60.8~~ \pm ~~0.30.2~~ Tg a⁻¹ (Waste), 9.49.6 \pm 1.1 Tg a⁻¹ (Wetlands), and 1.7 ± 0.9 Tg a⁻¹ (Other Natural). The
655 degrees of freedom for signal and singular value decomposition (Fig. S94) show 3–4 independent pieces of information can
656 be retrieved, which are differentiated in the figure by solid and hatched bars. The singular value decomposition shows strong
657 source signals corresponding to wetlands and energy with signal-to-noise ratios of ~37 and ~5, respectively. These are the

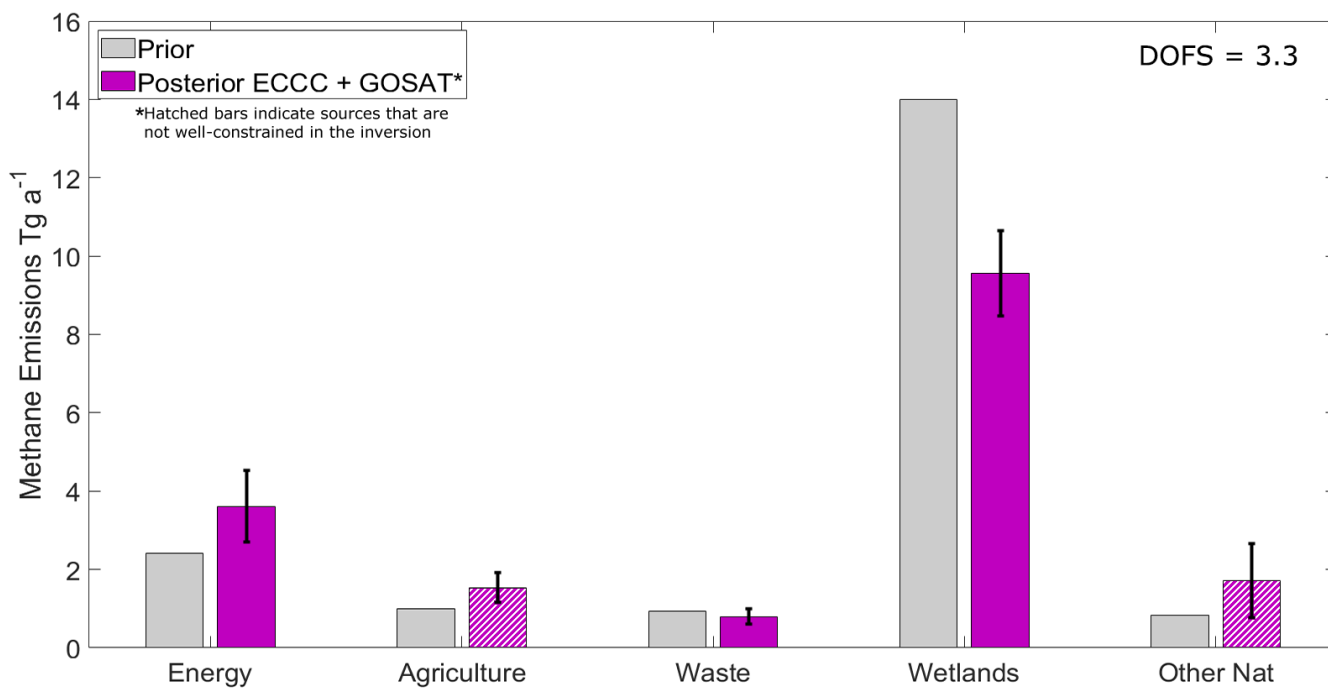
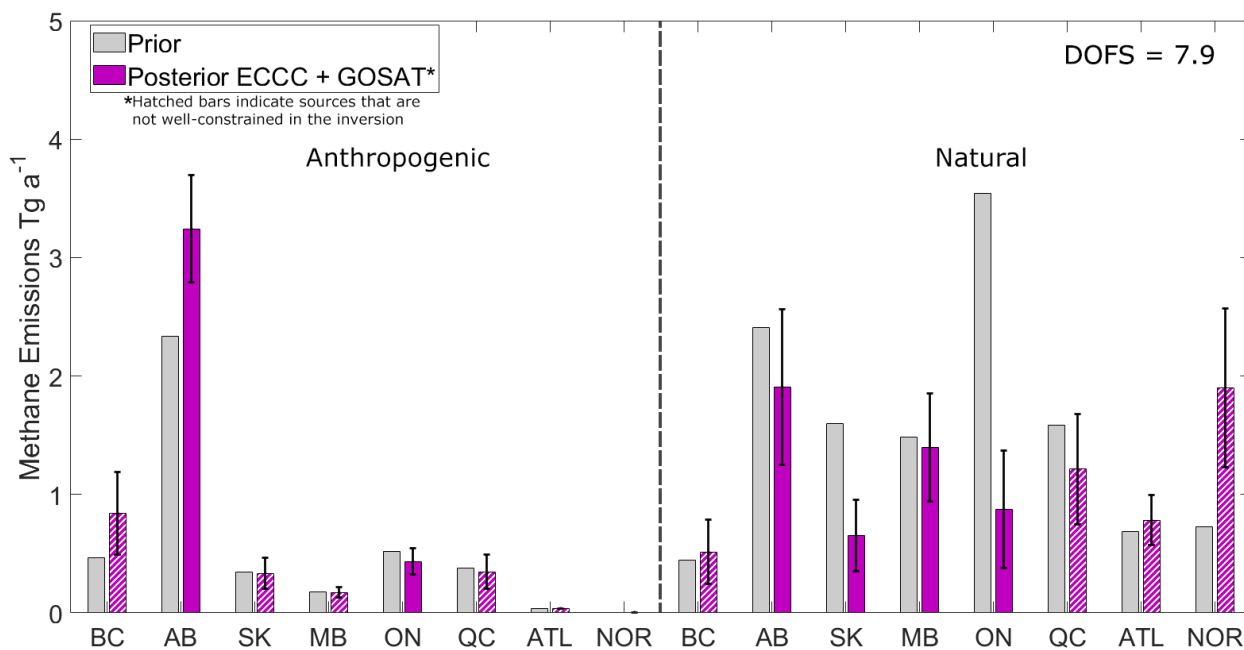
two largest emissions sources in Canada and show the inverse system can successfully disentangle the major anthropogenic and natural contributors. Emissions from waste have a signal-to-noise ratio of ~ 2 and can be constrained despite the low magnitude of emissions. This is likely due to waste emissions being more concentrated in Central Canada and away from the influence of large energy and agriculture emissions in Western Canada. Emissions from other natural sources are at the noise limit and show a moderate correlation with wetlands, which shows that these two sources are not completely independent. Agriculture emissions are below the noise in the system and highly correlated with energy emissions. This is likely due to the high spatial overlap of energy and agriculture emissions in Western Canada. As a result of these limitations, we present the total of energy and agriculture as $5.1 \pm 1.0 \text{ Tg a}^{-1}$ and the total of wetlands and other natural as ~~4.4~~11.3 $\pm 1.4 \text{ Tg a}^{-1}$. Our results for total natural and total anthropogenic emissions are consistent with the results from the previous monthly inversion, with the added benefit of identifying which sectors are responsible for the higher anthropogenic emissions at the cost of lower temporal resolution. Waste emissions are ~~36~~15% lower than the prior and ~~35~~14% lower than the National GHG Inventory. The total for energy and agriculture is 49% higher than the prior and 59% higher than the total in the inventory. These results show that energy and/or agriculture are the sectors that are responsible for the higher anthropogenic emissions.

Figure ~~9~~7 (bottom) shows the provincial inversion corresponding to the six largest emitting provinces (BC British Columbia, AB Alberta, SK, Saskatchewan, MB Manitoba, ON Ontario, QC Quebec) and two aggregated regions (ATL Atlantic Canada, NOR Northern Territories). These regions are further subdivided into total anthropogenic and total natural methane emissions, with below detection limit anthropogenic emissions from Atlantic Canada and Northern Territories. This inversion especially challenges the limitations of the ECCC+GOSAT observation system, as only about 8 of 16 independent pieces of information are retrieved. This means that half of the posterior provincial emissions are below the noise, and we are unable to constrain province-by-province emissions. The singular value decomposition identifies which regions are well constrained (Fig. S105). For the anthropogenic emissions AB and ON are strongly constrained. For the natural emissions AB, ON, SK and MB are well constrained. BC shows correlation between its own anthropogenic and natural emissions and cannot be completely disaggregated. As a result, we group elements together in Western Canada (BC + AB + SA + MB) and Central Canada (ON + QC) for interpretation. The total for Western Canada anthropogenic emissions is ~~4.6~~4.7 $\pm 0.6 \text{ Tg a}^{-1}$ which is ~~39~~42% higher than the prior of 3.3 Tg a^{-1} . The total for Central Canada is $0.8 \pm 0.2 \text{ Tg a}^{-1}$ which is 11% lower than the prior of 0.9 Tg a^{-1} .

Each of our top-down inversion results show higher total anthropogenic emissions than bottom-up estimates. This is consistent regardless of the observation vector incorporating ECCC data, GOSAT data or ECCC+GOSAT data. The subnational scale emissions are limited in their ability to provide full characterization of minor emissions across Canada but can successfully constrain major emissions for source attribution. The sectoral inversion attributes higher anthropogenic emissions to energy and/or agriculture and applies a small decrease to waste emissions. The provincial inversion attributes higher anthropogenic emissions to Western Canada and a small decrease to Central Canada. These results suggest that

692 anthropogenic emissions in Canada are underestimated primarily because of higher emissions from Western Canada energy
693 and/or agriculture. This interpretation is consistent with previous satellite inverse modelling studies over North America that
694 apply positive scaling factors to grid box clusters in Western Canada to match observations (Maasakkers et al., 2019; Turner
695 et al., 2015; Wecht et al., 2014). Aircraft studies in Alberta have also shown higher emissions from oil and gas in Alberta
696 than bottom up estimates (Baray et al., 2018; Johnson et al., 2017). Atherton et al. (2017) estimated higher emissions from
697 natural gas in north-eastern British Columbia using mobile surface in situ measurements (Atherton et al., 2017). Zavala-
698 Araiza et al. (2018) showed a significant amount of methane emissions in Alberta from equipment leaks and venting go
699 unreported due to current reporting requirements and in some regions a small number of sites may be responsible for most
700 methane emissions. Our inverse modelling results from 2010–2015 suggest a consistent presence of under-reported or
701 unreported emissions which require a policy adjustment to reporting practices.





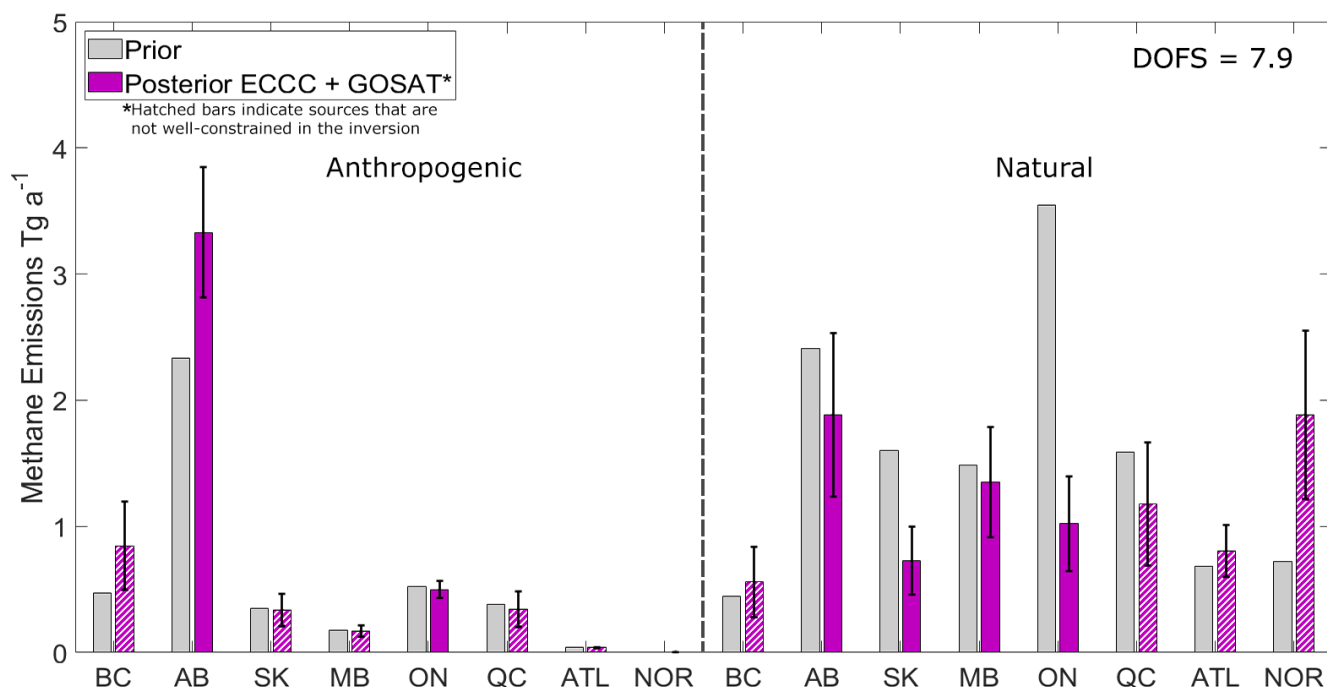


Figure 79: Joint-inversions combining 2010–2015 ECCC in situ and GOSAT satellite data showing how the combined observing system remains limited towards resolving all Canadian sources. Inversions are done for each year and we present the six-year average with error bars showing the 1 σ standard deviation of the yearly results. Hatched bars indicate sources that are not well-constrained, these are defined as state vector elements with averaging kernel sensitivities less than 0.8 which are affected by aliasing with other sources (See Supplemental Fig. S4-9 and S5-10). The top panel shows the sectoral inversion according to the categories in the National GHG inventory-Inventory (Energy, Agriculture, Waste) and two natural categories (Wetlands and Other Natural). As an example, the diagnostics in Figure S94 shows Agriculture emissions are beneath the noise and cannot be distinguished from Energy. The bottom panel shows the subnational regional inversion according to provinces (BC British Columbia, AB Alberta, SK, Saskatchewan, MB Manitoba, ON Ontario, QC Quebec) and aggregated regions (ATL Atlantic Canada, NOR Northern Territories) further subdivided according to total anthropogenic and total natural emissions. The diagnostics in Fig. S105 show more than half of the regions are at or below the noise. For anthropogenic emissions, the best constraints are on provinces AB and ON. For natural emissions, the best constraints are on AB, SK, MB and ON.

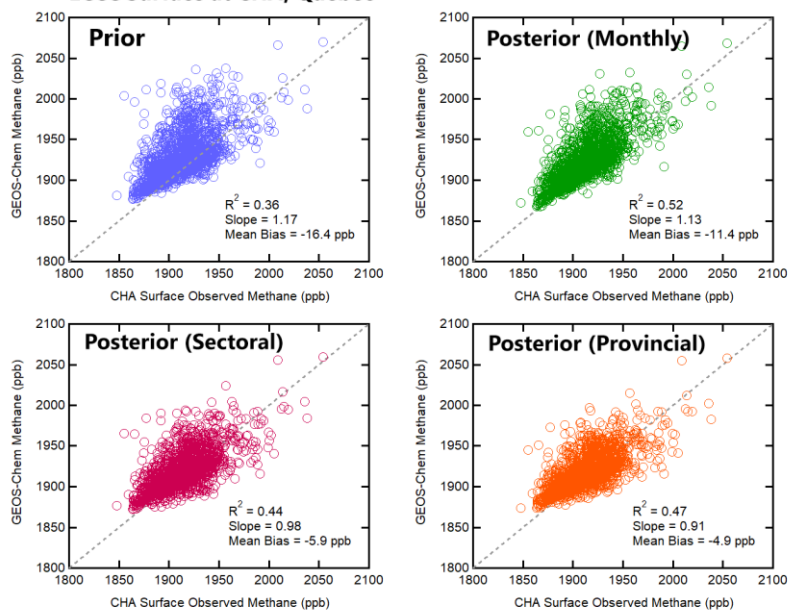
3.45 Comparison to Independent Aircraft and In situ Data

We test the robustness of the optimized emissions from each of the three inversions shown (monthly natural, sectoral, and provincial) by comparing to independent measurements not used in the inversions. Prior and posterior simulated methane concentrations are compared to measurements from NOAA ESRL aircraft profiles at East Trout Lake, Saskatchewan (Mund et al., 2017) and ECCC surface measurements in sites Chapais and Chibougamau in Quebec, Canada. The surface data was

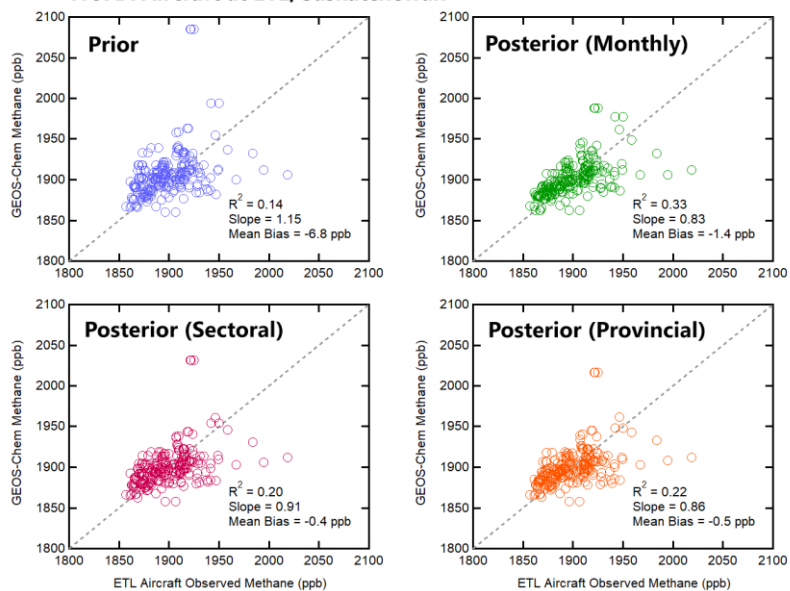
731 averaged to daily afternoon means (12:00 to 16:00 local time) in the same manner as the surface measurements used in the
 732 inversion. Aircraft data from the NOAA ESRL profiles coincide spatially with the surface measurements at ETL through a
 733 joint analysis program with Environment and Climate Change Canada and have occurred on a regular basis approximately
 734 once a month from 2005 until present time. Aircraft measurements reach ~7000 m above the surface with samples at
 735 multiple altitudes accomplished using a programmable multi-flask system that is further discussed in Mund et al. (2017),
 736 however we limit the comparison to the lowest 1 km above ground since higher altitude measurements are mostly
 737 background. The aircraft data is not averaged however the flights occur around the same time in the early afternoon.

738
 739 Figure 40-8 shows the comparison using reduced-major axis (RMA) regressions with the coefficient of determination (R^2),
 740 the slope and the mean-bias shown as metrics to evaluate the agreement. Surface data in CHA, Quebec shows better
 741 posterior agreement with observations according to all metrics for each of the three inversions. The R^2 of the prior is 0.36
 742 and improves to a range of 0.44–0.52–49 for the posterior results, the slope is 1.17 in the prior and improves to a range of
 743 0.94–92–1.13–12 and the mean bias (model – observations) is +16.4 ppb in the prior and improves to –11.4–13.2 and –
 744 4.9–5.6 ppb. Since this site in Quebec is particularly sensitive to the Hudson Bay Lowlands, the agreement in all metrics
 745 suggests our posterior emissions can better represent ~~wetlands emissions~~ wetland emissions in this region. This includes the
 746 reduced peak seasonality of natural emissions in the monthly inversion, the reduction of ~~wetlands emissions~~ wetland
 747 emissions in the sectoral inversion ~~and~~ or the reduction of natural emissions primarily in Central Canada in the provincial
 748 inversion. Aircraft data in Saskatchewan shows improvement in the R^2 and mean bias metrics but slightly degrades the slope
 749 in one case. The R^2 of the prior is 0.14 and improves to a range of 0.20–0.33–30, the mean bias of the prior is –6.8–6.8 ppb
 750 and improves to –0.4–1.2 and –1.4–3.1 ppb. The slope of the prior is 1.15 which slightly degrades to 0.83 in the monthly
 751 inversion and improves to a range of 0.86–0.88–0.94–0.93 in the provincial and sectoral inversions. The high resolution aircraft
 752 measurements are more susceptible to representation error at this 2°x2.5° grid resolution. Furthermore, the time-series
 753 comparison to surface data at East Trout Lake (Fig. 64) shows overall lower sensitivity to summertime ~~wetlands~~
 754 ~~emissions~~ wetland emissions than Fraserdale and Egbert, and lower sensitivity to anthropogenic emissions from Alberta than
 755 Lac La Biche. Hence the modelled methane concentrations at the aircraft measurement points are adjusted less by the change
 756 in posterior emissions. However, improvement in the R^2 and mean bias metrics show there is still a better representation of
 757 the variance in the data which suggests the posterior emissions reduce bias due to peak emission episodes.

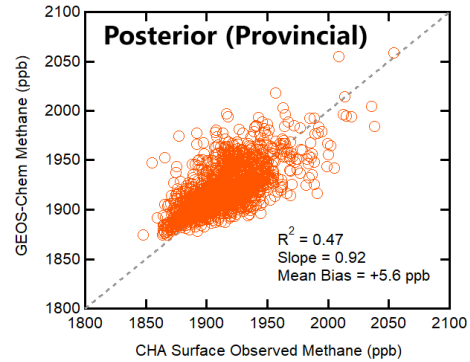
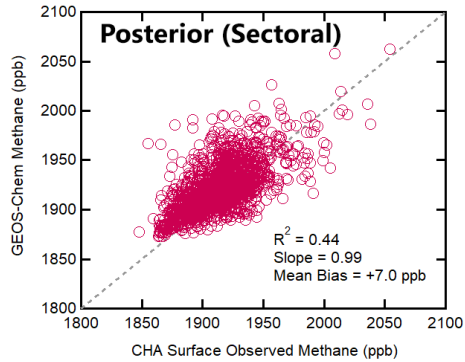
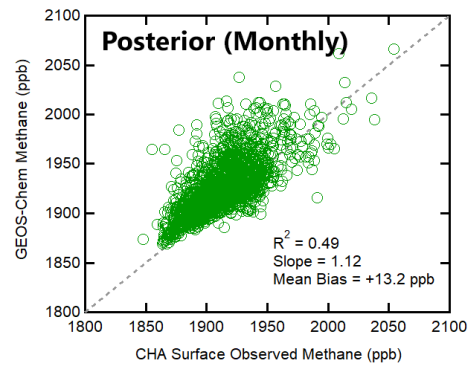
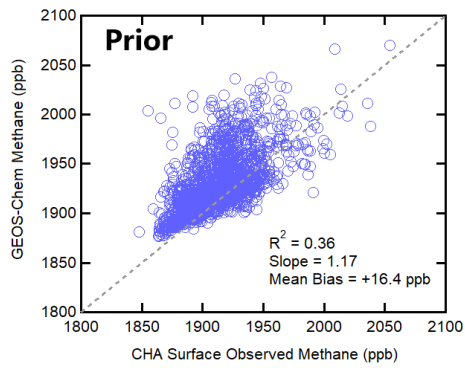
ECCC Surface at CHA, Quebec



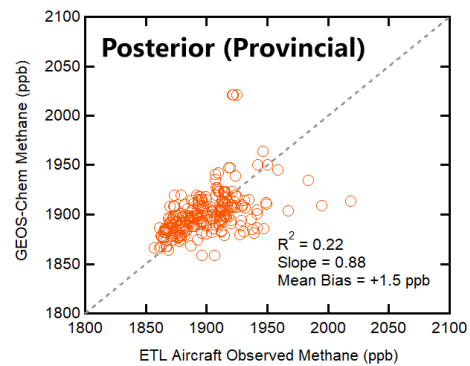
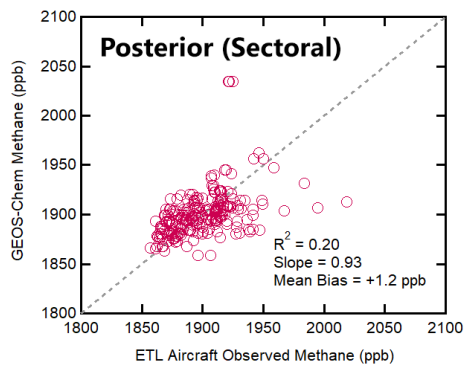
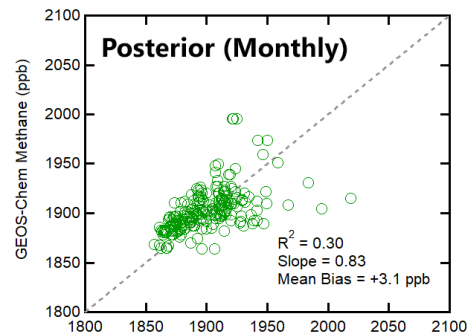
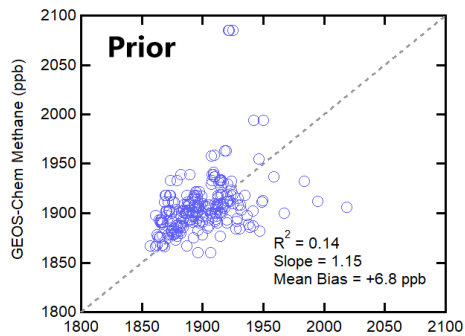
NOAA Aircraft at ETL, Saskatchewan



ECCC Surface at CHA, Quebec



NOAA Aircraft at ETL, Saskatchewan



763 **Figure 108:** Evaluation of inversion results with reduced-major axis (RMA) regressions using independent data. The top
 764 four panels show the comparison to ECCC surface observations at Chapais and Chibougamau in Quebec, Canada and the
 765 bottom four panels show the comparison to NOAA aircraft profiles at East Trout Lake, Saskatchewan. The agreement of
 766 observations with prior simulated methane concentrations (blue) are compared to posterior concentrations using optimized
 767 emissions from the monthly inversion (green), the sectoral inversion (magenta), and the provincial inversion (orange). The
 768 coefficient of determination (R^2), slope and mean bias are shown as metrics of agreement.

769 4 Conclusions

770 We conduct a Bayesian inverse analysis to optimize anthropogenic and natural methane emissions in Canada using 2010–
 771 2015 ECCC in situ and GOSAT satellite observations in GEOS-Chem. Methane concentrations are simulated on a $2^\circ \times 2.5^\circ$
 772 grid using recently updated prior emissions inventories for energy and ~~wetlands emissions~~ wetland emissions in Canada.
 773 Modelled background conditions for the Canadian domain are shown to be unbiased in the comparison to surface in situ data
 774 at the western most site in Canada, Estevan point, with agreement within 6 ppb. A forward model analysis shows much
 775 larger biases between –100 ppb and +1050 ppb at surface sites throughout Canada demonstrating the presence of
 776 misrepresented local emissions. We show large positive biases (overestimation of emissions) in the summertime are
 777 observed at sites sensitive to ~~wetlands emissions~~ wetland emissions, these biases are reduced by using lower magnitude
 778 ~~wetlands emissions~~ wetland emissions scenarios with lower CH_4 :C temperature sensitivities or lower inundation extent. We
 779 also show the opposite case of negative biases (underestimation of emissions) observed year-round at sites in Western
 780 Canada. The forward model analysis is consistent with the results of the inverse analysis that reduce emissions from natural
 781 sources and increase emissions from anthropogenic sources to minimize the mismatch between modelled and observed
 782 methane.

783
 784 We show three approaches for using ECCC and GOSAT data towards inverse modelling of Canadian methane emissions.
 785 These approaches differ according to the temporal and spatial resolution of the solution. We show: (1) a relatively higher
 786 time-resolution inversion that solves for natural emissions each month from 2010–2015 and anthropogenic emissions as
 787 yearly totals, (2) a sectoral inversion that solves for emissions according to categories in the N~~a~~tional I~~n~~ventory, (3) a
 788 provincial inversion that solves for total anthropogenic and natural emissions at the subnational level. The monthly inversion
 789 provides information on the seasonality of natural emissions (which are ~95% wetlands) but does not provide more depth
 790 into anthropogenic emissions beyond yearly scaling. The sectoral inversion provides more information on the categories of
 791 anthropogenic emissions that are misrepresented in the prior but without spatial detail. The provincial inversion provides the
 792 highest level of spatial discretization but is largely underdetermined due to the limitations of the observing system towards
 793 characterizing very low magnitude emissions from smaller contributing provinces.

794

795 Inversion results (1) show mean 2010–2015 posterior emissions for total anthropogenic sources in Canada are $6.0 \pm 0.4 \text{ Tg a}^{-1}$
 796 ¹ using ECCC data and $6.5 \pm 0.7 \text{ Tg a}^{-1}$ using GOSAT data. Annual mean natural emissions are ~~10.5 ± 1.6~~ 11.6 ± 1.2 Tg a^{-1}
 797 using ECCC data and $11.7 \pm 1.2 \text{ Tg a}^{-1}$ using GOSAT data. Both inverse modelling estimates are higher than the prior for
 798 anthropogenic emissions 4.4 Tg a^{-1} and lower than the prior for natural emissions 14.8 Tg a^{-1} . Inversion results using both
 799 datasets show a change in the seasonal profile of natural methane emissions where emissions are slower to begin in the
 800 spring and show a less intense peak in the summer. The agreement between two datasets assembled with different
 801 measurement methodologies that sample different parts of the atmosphere is a robust result that lends weight to our
 802 conclusions. Our results corroborate recent studies showing a less-intense and less-narrow summertime peak in North
 803 American Boreal ~~wetlands emissions~~ wetland emissions with a higher relative contribution from the cold season (Miller et
 804 al., 2016; Zona et al., 2016; Warwick et al., 2016; Thonat et al., 2017; Treat et al., 2018; Peltola et al., 2019). These top-
 805 down studies using atmospheric observations show biosphere process models can better account for a more complex
 806 response to peak surface soil temperatures.

807
 808 We also conduct combined ECCC+GOSAT inversions that aim to resolve finer resolution emissions corresponding to (2) the
 809 sectors of the National Inventory and corresponding to (3) provincial boundaries. These policy-themed inversions
 810 challenge the capabilities of the ECCC+GOSAT observation system and show the system is not capable of resolving many
 811 minor emissions in Canada. The degrees of freedom for signal for these inversions are 3–4 out of 5 state vector elements for
 812 the sectoral inversion and 8 out of 16 for the provincial inversion. The limitation of this inverse approach towards
 813 constraining sectoral or regional scale emissions in Canada is due to the low magnitude of these emissions, their overlapping
 814 nature in concentrated regions, and the sparsity of data available to distinguish them apart. Grouping correlated sectors
 815 together, we determine $5.1 \pm 1.0 \text{ Tg a}^{-1}$ for energy and agriculture which is 59% higher than the inventory, ~~0.6 ± 0.8~~ 0.30 ± 0.2
 816 Tg a^{-1} for waste which is ~~35~~ 14% lower than the inventory. For provincial emissions, we show Western Canada is ~~4.6 ± 4.7~~ \pm
 817 0.6 Tg a^{-1} which is ~~39~~ 42% higher than the prior and Central Canada is 0.8 ± 0.2 which is 11% lower. Both regions show
 818 lower natural emissions. These results show that the higher anthropogenic emissions in the posterior results can be attributed
 819 to energy and/or agriculture primarily in Western Canada where most of Canadian anthropogenic emissions are
 820 concentrated. Our results are consistent with other top-down studies that show higher than reported anthropogenic emissions
 821 in Western Canada (Wecht et al., 2014; Turner et al., 2015; Atherton et al., 2017; Johnson et al., 2017; Baray et al., 2018;
 822 Maasackers et al., 2019). This may be due to oil and gas emissions that are under-reported or unreported due to current
 823 reporting requirements (Zavala-Araiza et al., 2018). These top-down studies show a need for policy readjustment in
 824 reporting practices for Canadian anthropogenic methane emissions.

825
 826 This study shows the value of using complementary surface and satellite datasets in an inverse analysis. We emphasize the
 827 value of comparative analysis using the datasets independently versus as joint inversions, as minor emissions are too low in
 828 magnitude for the observational precision to distinguish finer scale discretization above the noise. The comparative analysis

829 has the added benefit of evaluating the datasets against each other and the assumptions that are specific to using either
830 surface or satellite data. The capabilities for combining and intercomparing datasets is expected to improve, with the launch
831 of Copernicus Sentinel-5p satellite (TROPOMI) in 2017 and continued expansions on in situ observation networks. The
832 ability for next generation observations to constrain subnational level emissions in Canada will depend on instrument and
833 model precision, as well as the emissions magnitudes and spatiotemporal overlap of the targets. These technical capabilities
834 should be weighed alongside policy needs for improved methane monitoring.

835

836 **Competing Interests**

837 The authors declare that they have no conflict of interest.

838 **Data Availability**

839 GEOS-Chem is from <http://acmg.seas.harvard.edu/geos/> which includes links to all gridded prior emissions and
840 meteorological fields used in this analysis. GOSAT satellite data is from the University of Leicester v7 proxy retrieval is
841 available through the Copernicus Climate Change Service <https://climate.copernicus.eu/>. ECCC in situ data is available
842 through the World Data Centre for Greenhouse Gases (WDCGG) <https://gaw.kishou.go.jp/>. NOAA/ESRL aircraft data is
843 from the Global Monitoring Laboratory <https://www.esrl.noaa.gov/gmd/ccgg/aircraft/>.

844 **Author Contributions**

845 SB, DJJ and RM designed the study. SB conducted the simulations and analysis with contributions from JDM, JXS, MPS,
846 and DBAJ. AAB provided WetCHARTS emissions and supporting data. SB and RM wrote the paper with contributions
847 from all authors.

848 **Acknowledgements**

849 Work at Harvard was supported by the NASA Carbon Monitoring System. We thank the Japanese Aerospace Exploration
850 Agency (JAXA) responsible for the GOSAT instrument, and the University of Leicester for the retrieval algorithm used in
851 this analysis. Doug Worthy and the Climate Research Division at Environment and Climate Change Canada are responsible
852 for the in situ surface measurements and the NOAA/ESRL/GML program is responsible for the ~~aircraft methane~~
853 ~~measurements~~. Carbon Cycle Greenhouse Gases (CCGG) cooperative air sampling network measurements.

854

855

856
857
858
859
860
861
862
863

864 **References**

- 865 Atherton, E., Risk, D., Fougère, C., Lavoie, M., Marshall, A., Werring, J., Williams, J. P. and Minions, C.: Mobile
866 measurement of methane emissions from natural gas developments in northeastern British Columbia, Canada, *Atmos. Chem.*
867 *Phys.*, 17(20), 12405–12420, doi:10.5194/acp-17-12405-2017, 2017.
- 868 Baray, S., Darlington, A., Gordon, M., Hayden, K. L., Leithead, A., Li, S.-M., Liu, P. S. K., Mittermeier, R. L., Moussa, S.
869 G., O'Brien, J., Staebler, R., Wolde, M., Worthy, D. and McLaren, R.: Quantification of methane sources in the Athabasca
870 Oil Sands Region of Alberta by aircraft mass balance, *Atmos. Chem. Phys.*, 18(10), 7361–7378, doi:10.5194/acp-18-7361-
871 2018, 2018.
- 872 Bloom, A. A., Bowman, K. W., Lee, M., Turner, A. J., Schroeder, R., Worden, J. R., Weidner, R., McDonald, K. C. and
873 Jacob, D. J.: A global wetland methane emissions and uncertainty dataset for atmospheric chemical transport models
874 (WetCHARTs version 1.0), *Geosci. Model Dev.*, 10(6), 2141–2156, doi:10.5194/gmd-10-2141-2017, 2017.
- 875 Bubier, J. L., Moore, T. R. and Roulet, N. T.: Methane Emissions from Wetlands in the Midboreal Region of Northern
876 Ontario, Canada, *Ecology*, 74(8), 2240–2254, doi:10.2307/1939577, 1993.
- 877 Buchwitz, M., Reuter, M., Schneising, O., Boesch, H., Guerlet, S., Dils, B., Aben, I., Armante, R., Bergamaschi, P.,
878 Blumenstock, T., Bovensmann, H., Brunner, D., Buchmann, B., Burrows, J. P., Butz, A., Chédin, A., Chevallier, F.,
879 Crevoisier, C. D., Deutscher, N. M., Frankenberg, C., Hase, F., Hasekamp, O. P., Heymann, J., Kaminski, T., Laeng, A.,
880 Lichtenberg, G., De Mazière, M., Noël, S., Notholt, J., Orphal, J., Popp, C., Parker, R., Scholze, M., Susmann, R., Stiller,
881 G. P., Warneke, T., Zehner, C., Bril, A., Crisp, D., Griffith, D. W. T., Kuze, A., O'Dell, C., Oshchepkov, S., Sherlock, V.,
882 Suto, H., Wennberg, P., Wunch, D., Yokota, T. and Yoshida, Y.: The Greenhouse Gas Climate Change Initiative (GHG-
883 CCI): Comparison and quality assessment of near-surface-sensitive satellite-derived CO₂ and CH₄ global data sets, *Remote*
884 *Sensing of Environment*, 162, 344–362, doi:10.1016/j.rse.2013.04.024, 2015.
- 885 Butz, A., Guerlet, S., Hasekamp, O., Schepers, D., Galli, A., Aben, I., Frankenberg, C., Hartmann, J.-M., Tran, H., and Kuze,
886 A.: Toward accurate CO₂ and CH₄ observations from GOSAT, *Geophys. Res. Lett.*, 38, L14812,
887 <https://doi.org/10.1029/2011GL047888>, 2011.

888 Chanton, J. and Liptay, K.: Seasonal variation in methane oxidation in a landfill cover soil as determined by an in-situ stable
889 isotope technique, *Global Biogeochem. Cycles*, 14(1), 51–60, doi:10.1029/1999GB900087, 2000.

890 Dlugokencky, E. J., Bruhwiler, L., White, J. W. C., Emmons, L. K., Novelli, P. C., Montzka, S. A., Masarie, K. A., Lang, P.
891 M., Crotwell, A. M., Miller, J. B. and Gatti, L. V.: Observational constraints on recent increases in the atmospheric CH₄
892 burden, *Geophys. Res. Lett.*, 36(18), L18803, doi:10.1029/2009GL039780, 2009. Darmenov, A. and da Silva, A.: The quick
893 fire emissions dataset (QFED)—documentation of versions 2.1, 2.2 and 2.4, *NASA Technical Report Series on Global*
894 *Modeling and Data Assimilation*, NASA TM-2013-104606, 32, 183 pp., 2013.

895 Environment and Climate Change Canada: National Inventory Report 1990–2015: Greenhouse Gas Sources and Sinks in
896 Canada, Canada’s Submission to the United Nations Framework Convention on Climate Change, Part 3. Available at:
897 http://publications.gc.ca/collections/collection_2018/eccc/En81-4-2015-3-eng.pdf, 2017.

898 ESA CCI GHG project team: ESA Greenhouse Gases Climate Change Initiative (GHG_cci): Column-averaged CH₄ from
899 GOSAT generated with the OCPR (UoL-PR) Proxy algorithm (CH₄_GOS_OCPR), v7.0. Centre for Environmental Data
900 Analysis, Available at: <https://catalogue.ceda.ac.uk/uuid/f9154243fd8744bdaf2a59c39033e659>, 2018.

901 Fung, I., John, J., Lerner, J., Matthews, E., Prather, M., Steele, L. P. and Fraser, P. J.: Three-dimensional model synthesis of
902 the global methane cycle, *J. Geophys. Res.*, 96(D7), 13033, doi:10.1029/91JD01247, 1991.

903 Hartmann, D. L., Tank, A. M. K., Rusticucci, M., Alexander, L. V., Brönnimann, S., Charabi, Y. A. R., Dentener, F. J.,
904 Dlugokencky, E. J., Easterling, D. R., Kaplan, A., Soden, B. J., Thorne, P. W., Wild, M., and Zhai, P. M.: Observations:
905 atmosphere and surface, in: *Climate Change 2013 the Physical Science Basis: Working Group I Contribution to the Fifth*
906 *Assessment Report of the Intergovernmental Panel on Climate Change*, Cambridge University Press, 2013.

907 Hausmann, P., Sussmann, R. and Smale, D.: Contribution of oil and natural gas production to renewed increase in
908 atmospheric methane (2007–2014): top-down estimate from ethane and methane column observations, *Atmos. Chem. Phys.*,
909 16(5), 3227–3244, doi:10.5194/acp-16-3227-2016, 2016.

910 Heald, C. L., Jacob, D. J., Jones, D. B. A., Palmer, P. I., Logan, J. A., Streets, D. G., Sachse, G. W., Gille, J. C., Hoffman, R.
911 N. and Nehr Korn, T.: Comparative inverse analysis of satellite (MOPITT) and aircraft (TRACE-P) observations to estimate
912 Asian sources of carbon monoxide: COMPARATIVE INVERSE ANALYSIS, *J. Geophys. Res.*, 109(D23),
913 doi:10.1029/2004JD005185, 2004.

914 Hu, H., Landgraf, J., Detmers, R., Borsdorff, T., Aan de Brugh, J., Aben, I., Butz, A. and Hasekamp, O.: Toward Global
915 Mapping of Methane With TROPOMI: First Results and Intersatellite Comparison to GOSAT, *Geophys. Res. Lett.*, 45(8),
916 3682–3689, doi:10.1002/2018GL077259, 2018.

917 Ishizawa, M., Chan, D., Worthy, D., Chan, E., Vogel, F. and Maksyutov, S.: Analysis of atmospheric CH₄ in Canadian
918 Arctic and estimation of the regional CH₄ fluxes, *Atmos. Chem. Phys.*, 19(7), 4637–4658, doi:10.5194/acp-19-4637-2019,
919 2019.

920 Jacob, D. J., Turner, A. J., Maasakkers, J. D., Sheng, J., Sun, K., Liu, X., Chance, K., Aben, I., McKeever, J. and
 921 Frankenberg, C.: Satellite observations of atmospheric methane and their value for quantifying methane emissions, *Atmos.*
 922 *Chem. Phys.*, 16(22), 14371–14396, doi:10.5194/acp-16-14371-2016, 2016.

923 Johnson, M. R., Tyner, D. R., Conley, S., Schwietzke, S. and Zavala-Araiza, D.: Comparisons of Airborne Measurements
 924 and Inventory Estimates of Methane Emissions in the Alberta Upstream Oil and Gas Sector, *Environ. Sci. Technol.*, 51(21),
 925 13008–13017, doi:10.1021/acs.est.7b03525, 2017.

926 Kirschke, S., Bousquet, P., Ciais, P., Saunois, M., Canadell, J. G., Dlugokencky, E. J., Bergamaschi, P., Bergmann, D.,
 927 Blake, D. R., Bruhwiler, L., Cameron-Smith, P., Castaldi, S., Chevallier, F., Feng, L., Fraser, A., Heimann, M., Hodson, E.
 928 L., Houweling, S., Josse, B., Fraser, P. J., Krummel, P. B., Lamarque, J.-F., Langenfelds, R. L., Le Quééré, C., Naik, V.,
 929 O’Doherty, S., Palmer, P. I., Pison, I., Plummer, D., Poulter, B., Prinn, R. G., Rigby, M., Ringeval, B., Santini, M., Schmidt,
 930 M., Shindell, D. T., Simpson, I. J., Spahni, R., Steele, L. P., Strode, S. A., Sudo, K., Szopa, S., van der Werf, G. R.,
 931 Voulgarakis, A., van Weele, M., Weiss, R. F., Williams, J. E. and Zeng, G.: Three decades of global methane sources and
 932 sinks, *Nature Geosci.*, 6(10), 813–823, doi:10.1038/ngeo1955, 2013.

933 Kuze, A., Suto, H., Shiomi, K., Kawakami, S., Tanaka, M., Ueda, Y., Deguchi, A., Yoshida, J., Yamamoto, Y., Kataoka, F.,
 934 Taylor, T. E., and Buijs, H. L.: Update on GOSAT TANSOFTS performance, operations, and data products after more than
 935 6 years in space, *Atmos. Meas. Tech.*, 9, 2445–2461, <https://doi.org/10.5194/amt-9-2445-2016>, 2016.

936 Lu, X., Jacob, D. J., Zhang, Y., Maasakkers, J. D., Sulprizio, M. P., Shen, L., Qu, Z., Scarpelli, T. R., Nesser, H., Yantosca,
 937 R. M., Sheng, J., Andrews, A., Parker, R. J., Boesch, H., Bloom, A. A., and Ma, S.: Global methane budget and trend, 2010–
 938 2017: complementarity of inverse analyses using in situ (GLOBALVIEWplus CH4 ObsPack) and satellite (GOSAT)
 939 observations, *Atmos. Chem. Phys.*, 21, 4637–4657, <https://doi.org/10.5194/acp-21-4637-2021>, 2021. ~~Lu, X., Jacob, D. J.,~~
 940 ~~Zhang, Y., Maasakkers, J. D., Sulprizio, M. P., Shen, L., Qu, Z., Scarpelli, T. R., Nesser, H., Yantosca, R. M., Sheng, J.,~~
 941 ~~Andrews, A., Parker, R. J., Boesch, H., Bloom, A. A., and Ma, S.: Global methane budget and trend, 2010–2017:~~
 942 ~~complementarity of inverse analyses using in situ (GLOBALVIEWplus CH4 ObsPack) and satellite (GOSAT) observations,~~
 943 ~~*Atmos. Chem. Phys. Discuss.*, <https://doi.org/10.5194/acp-2020-775>, in review, 2020.~~

944 Maasakkers, J. D., Jacob, D. J., Sulprizio, M. P., Turner, A. J., Weitz, M., Wirth, T., Hight, C., DeFigueiredo, M., Desai, M.,
 945 Schmeltz, R., Hockstad, L., Bloom, A. A., Bowman, K. W., Jeong, S. and Fischer, M. L.: Gridded National Inventory of
 946 U.S. Methane Emissions, *Environ. Sci. Technol.*, 50(23), 13123–13133, doi:10.1021/acs.est.6b02878, 2016.

947 Maasakkers, J. D., Jacob, D. J., Sulprizio, M. P., Scarpelli, T. R., Nesser, H., Sheng, J.-X., Zhang, Y., Hersher, M., Bloom,
 948 A. A., Bowman, K. W., Worden, J. R., Janssens-Maenhout, G. and Parker, R. J.: Global distribution of methane emissions,
 949 emission trends, and OH concentrations and trends inferred from an inversion of GOSAT satellite data for 2010–2015,
 950 *Atmos. Chem. Phys.*, 19(11), 7859–7881, doi:10.5194/acp-19-7859-2019, 2019.

951 Maasakkers, J. D., Jacob, D. J., Sulprizio, M. P., Scarpelli, T. R., Nesser, H., Sheng, J., Zhang, Y., Lu, X., Bloom, A. A.,
 952 Bowman, K. W., Worden, J. R., and Parker, R. J.: 2010–2015 North American methane emissions, sectoral contributions,

953 ~~and trends: a high-resolution inversion of GOSAT observations of atmospheric methane, *Atmos. Chem. Phys.*, 21, 4339–~~
954 ~~4356, <https://doi.org/10.5194/acp-21-4339-2021>, 2021.~~

955 ~~Maasakkers, J. D., Jacob, D. J., Sulprizio, M. P., Scarpelli, T. R., Nesser, H., Sheng, J., Zhang, Y., Lu, X., Bloom, A. A.,~~
956 ~~Bowman, K. W., Worden, J. R., and Parker, R. J.: 2010–2015 North American methane emissions, sectoral contributions,~~
957 ~~and trends: a high-resolution inversion of GOSAT satellite observations of atmospheric methane, *Atmos. Chem. Phys.*~~
958 ~~*Discuss.*, <https://doi.org/10.5194/acp-2020-915>, in review, 2020.~~

959 Miller, S. M., Worthy, D. E. J., Michalak, A. M., Wofsy, S. C., Kort, E. A., Havice, T. C., Andrews, A. E., Dlugokencky, E.
960 J., Kaplan, J. O., Levi, P. J., Tian, H. and Zhang, B.: Observational constraints on the distribution, seasonality, and
961 environmental predictors of North American boreal methane emissions, *Global Biogeochem. Cycles*, 28(2), 146–160,
962 doi:10.1002/2013GB004580, 2014.

963 Miller, S. M., Commane, R., Melton, J. R., Andrews, A. E., Benmergui, J., Dlugokencky, E. J., Janssens-Maenhout, G.,
964 Michalak, A. M., Sweeney, C. and Worthy, D. E. J.: Evaluation of wetland methane emissions across North America using
965 atmospheric data and inverse modeling, *Biogeosciences*, 13(4), 1329–1339, doi:10.5194/bg-13-1329-2016, 2016.

966 Moore, T. R., Heyes, A. and Roulet, N. T.: Methane emissions from wetlands, southern Hudson Bay lowland, *J. Geophys.*
967 *Res.*, 99(D1), 1455, doi:10.1029/93JD02457, 1994.

968 Mund, J., Thoning, K., Tans, P., Sweeny, C., Higgs, J., Wolter, S., Crotwell, A., Neff, D., Dlugokencky, E., Lang, P.,
969 Novelli, P., Moglia, E. and Crotwell, M.: Earth System Research Laboratory Carbon Cycle and Greenhouse Gases Group
970 Flask-Air Sample Measurements of CO₂, CH₄, CO, N₂O, H₂, and SF₆ from the Aircraft Program, 1992-Present, ,
971 doi:10.7289/V5N58JMF, 2017.

972 Myhre, G.: Anthropogenic and Natural Radiative Forcing, in *Climate Change 2013: The Physical Science Basis.*
973 *Contribution of Working Group I to the Fifth Assessment Report of the Intergovernmental Panel on Climate Change.*, 2013.

974 ~~Nakajima, M., Suto, H., Yotsumoto, K., Shiomi, K., and Hirabayashi, T.: Fourier transform spectrometer on GOSAT and~~
975 ~~GOSAT-2, in: *International Conference on Space Optics — ICSO 2014, International Conference on Space Optics 2014,*~~
976 ~~*Tenerife, Canary Islands, Spain, 2*, <https://doi.org/10.1117/12.2304062>, 2017.~~

977 ~~Nisbet, E. G., Dlugokencky, E. J., Manning, M. R., Lowry, D., Fisher, R. E., France, J. L., Michel, S. E., Miller, J. B., White,~~
978 ~~J. W. C., Vaughn, B., Bousquet, P., Pyle, J. A., Warwick, N. J., Cain, M., Brownlow, R., Zazzeri, G., Lanoisellé, M.,~~
979 ~~Manning, A. C., Gloor, E., Worthy, D. E. J., Brunke, E. G., Labuschagne, C., Wolff, E. W. and Ganesan, A. L.: Rising~~
980 ~~atmospheric methane: 2007–2014 growth and isotopic shift: RISING METHANE 2007–2014, *Global Biogeochem. Cycles*,~~
981 ~~30(9), 1356–1370, doi:10.1002/2016GB005406, 2016.~~

982 Nisbet, E. G., Fisher, R. E., Lowry, D., France, J. L., Allen, G., Bakkaloglu, S., Broderick, T. J., Cain, M., Coleman, M.,
983 Fernandez, J., Forster, G., Griffiths, P. T., Iverach, C. P., Kelly, B. F. J., Manning, M. R., Nisbet-Jones, P. B. R., Pyle, J. A.,
984 Townsend-Small, A., al-Shalaan, A., Warwick, N. and Zazzeri, G.: Methane Mitigation: Methods to Reduce Emissions, on
985 the Path to the Paris Agreement, *Rev. Geophys.*, 58(1), doi:10.1029/2019RG000675, 2020.

986 [Parker, R., Boesch, H., Cogan, A., Fraser, A., Feng, L., Palmer, P. I., Messerschmidt, J., Deutscher, N., Griffith, D. W., and](#)
987 [Notholt, J.: Methane observations from the Greenhouse Gases Observing SATellite: Comparison to ground-based TCCON](#)
988 [data and model calculations, Geophys. Res. Lett., 38, L15807, <https://doi.org/10.1029/2011GL047871>, 2011.](#)
989 [Parker, R. J., Boesch, H., Byckling, K., Webb, A. J., Palmer, P. I., Feng, L., Bergamaschi, P., Chevallier, F., Notholt, J.,](#)
990 [Deutscher, N., Warneke, T., Hase, F., Sussmann, R., Kawakami, S., Kivi, R., Griffith, D. W. T., and Velazco, V.: Assessing 5](#)
991 [years of GOSAT Proxy XCH4 data and associated uncertainties, Atmos. Meas. Tech., 8, 4785–4801,](#)
992 <https://doi.org/10.5194/amt-8-4785-2015>, 2015.
993 Patra, P. K., Houweling, S., Krol, M., Bousquet, P., Belikov, D., Bergmann, D., Bian, H., Cameron-Smith, P., Chipperfield,
994 M. P., Corbin, K., Fortems-Cheiney, A., Fraser, A., Gloor, E., Hess, P., Ito, A., Kawa, S. R., Law, R. M., Loh, Z.,
995 Maksyutov, S., Meng, L., Palmer, P. I., Prinn, R. G., Rigby, M., Saito, R. and Wilson, C.: TransCom model simulations of
996 CH4 and related species: linking transport, surface flux and chemical loss with CH4 variability in the troposphere and lower
997 stratosphere, Atmos. Chem. Phys., 11(24), 12813–12837, doi:10.5194/acp-11-12813-2011, 2011.
998 Peltola, O., Vesala, T., Gao, Y., Rätty, O., Alekseychik, P., Aurela, M., Chojnicki, B., Desai, A. R., Dolman, A. J.,
999 Euskirchen, E. S., Friborg, T., Göckede, M., Helbig, M., Humphreys, E., Jackson, R. B., Jocher, G., Joos, F., Klatt, J., Knox,
1000 S. H., Kowalska, N., Kutzbach, L., Lienert, S., Lohila, A., Mammarella, I., Nadeau, D. F., Nilsson, M. B., Oechel, W. C.,
1001 Peichl, M., Pypker, T., Quinton, W., Rinne, J., Sachs, T., Samson, M., Schmid, H. P., Sonnentag, O., Wille, C., Zona, D. and
1002 Aalto, T.: Monthly gridded data product of northern wetland methane emissions based on upscaling eddy covariance
1003 observations, Earth Syst. Sci. Data, 11(3), 1263–1289, doi:10.5194/essd-11-1263-2019, 2019.
1004 Pickett-Heaps, C. A., Jacob, D. J., Wecht, K. J., Kort, E. A., Wofsy, S. C., Diskin, G. S., Worthy, D. E. J., Kaplan, J. O.,
1005 Bey, I. and Drevet, J.: Magnitude and seasonality of wetland methane emissions from the Hudson Bay Lowlands (Canada),
1006 Atmos. Chem. Phys., 11(8), 3773–3779, doi:10.5194/acp-11-3773-2011, 2011.
1007 Poulter, B., Bousquet, P., Canadell, J. G., Ciais, P., Pregon, A., Saunois, M., Arora, V. K., Beerling, D. J., Brovkin, V.,
1008 Jones, C. D., Joos, F., Gedney, N., Ito, A., Kleinen, T., Koven, C. D., McDonald, K., Melton, J. R., Peng, C., Peng, S.,
1009 Prigent, C., Schroeder, R., Riley, W. J., Saito, M., Spahni, R., Tian, H., Taylor, L., Viovy, N., Wilton, D., Wiltshire, A., Xu,
1010 X., Zhang, B., Zhang, Z. and Zhu, Q.: Global wetland contribution to 2000–2012 atmospheric methane growth rate
1011 dynamics, Environ. Res. Lett., 12(9), 094013, doi:10.1088/1748-9326/aa8391, 2017.
1012 [Prather, M. J., Holmes, C. D., and Hsu, J.: Reactive greenhouse gas scenarios: Systematic exploration of uncertainties and](#)
1013 [the role of atmospheric chemistry, Geophys. Res. Lett., 39, L09803, <https://doi.org/10.1029/2012GL051440>, 2012.](#)
1014 [Prather, M. J., Holmes, C. D. and Hsu, J.: Reactive greenhouse gas scenarios: Systematic exploration of uncertainties and the](#)
1015 [role of atmospheric chemistry: ATMOSPHERIC CHEMISTRY AND GREENHOUSE GASES, Geophys. Res. Lett., 39\(9\),](#)
1016 [n/a n/a, doi:10.1029/2012GL051440, 2012.](#)
1017 [Rigby, M., Montzka, S. A., Prinn, R. G., White, J. W. C., Young, D., O'Doherty, S., Lunt, M. F., Ganesan, A. L., Manning,](#)
1018 [A. J., Simmonds, P. G., Salameh, P. K., Harth, C. M., Mühle, J., Weiss, R. F., Fraser, P. J., Steele, L. P., Krummel, P. B.,](#)

1019 ~~McCulloch, A. and Park, S.: Role of atmospheric oxidation in recent methane growth, *Proc Natl Acad Sci USA*, 114(21),~~
1020 ~~5373–5377, doi:10.1073/pnas.1616426114, 2017.~~

1021 Rodgers, C. D.: *Inverse Methods for Atmospheric Sounding: Theory and Practice*, WORLD SCIENTIFIC., 2000.

1022 Rogelj, J., Popp, A., Calvin, K. V., Luderer, G., Emmerling, J., Gernaat, D., Fujimori, S., Strefler, J., Hasegawa, T.,
1023 Marangoni, G., Krey, V., Kriegler, E., Riahi, K., van Vuuren, D. P., Doelman, J., Drouet, L., Edmonds, J., Fricko, O.,
1024 Harmsen, M., Havlík, P., Humpenöder, F., Stehfest, E. and Tavoni, M.: Scenarios towards limiting global mean temperature
1025 increase below 1.5 °C, *Nature Clim Change*, 8(4), 325–332, doi:10.1038/s41558-018-0091-3, 2018.

1026 Sheng, J.-X., Jacob, D. J., Maasakkers, J. D., Sulprizio, M. P., Zavala-Araiza, D. and Hamburg, S. P.: A high-resolution
1027 ($0.1^\circ \times 0.1^\circ$) inventory of methane emissions from Canadian and Mexican oil and gas systems, *Atmospheric Environment*,
1028 158, 211–215, doi:10.1016/j.atmosenv.2017.02.036, 2017.

1029 Sheng, J.-X., Jacob, D. J., Turner, A. J., Maasakkers, J. D., Benmergui, J., Bloom, A. A., Arndt, C., Gautam, R., Zavala-
1030 Araiza, D., Boesch, H. and Parker, R. J.: 2010–2016 methane trends over Canada, the United States, and Mexico observed
1031 by the GOSAT satellite: contributions from different source sectors, *Atmos. Chem. Phys.*, 18(16), 12257–12267,
1032 doi:10.5194/acp-18-12257-2018, 2018a.

1033 Sheng, J.-X., Jacob, D. J., Turner, A. J., Maasakkers, J. D., Sulprizio, M. P., Bloom, A. A., Andrews, A. E. and Wunch, D.:
1034 High-resolution inversion of methane emissions in the Southeast US using SEAC 4 RS aircraft observations of atmospheric
1035 methane: anthropogenic and wetland sources, *Atmos. Chem. Phys.*, 18(9), 6483–6491, doi:10.5194/acp-18-6483-2018,
1036 2018b.

1037 ~~Stanevich, I., Jones, D. B. A., Strong, K., Parker, R. J., Boesch, H., Wunch, D., Notholt, J., Petri, C., Warneke, T.,~~
1038 ~~Sussmann, R., Schneider, M., Hase, F., Kivi, R., Deutscher, N. M., Velazco, V. A., Walker, K. A., and Deng, F.:~~
1039 ~~Characterizing model errors in chemical transport modeling of methane: impact of model resolution in versions v9-02 of~~
1040 ~~GEOS-Chem and v35j of its adjoint model, *Geosci. Model Dev.*, 13, 3839–3862, <https://doi.org/10.5194/gmd-13-3839-2020>,~~
1041 ~~2020.~~

1042 ~~Stanevich, I., Jones, D. B. A., Strong, K., Keller, M., Henze, D. K., Parker, R. J., Boesch, H., Wunch, D., Notholt, J., Petri,~~
1043 ~~C., Warneke, T., Sussmann, R., Schneider, M., Hase, F., Kivi, R., Deutscher, N. M., Velazco, V. A., Walker, K. A. and~~
1044 ~~Deng, F.: Characterizing model errors in chemical transport modelling of methane: Using GOSAT XCH₄ data with weak~~
1045 ~~constraint four dimensional variational data assimilation, preprint, *Gases/Atmospheric Modelling/Troposphere/Chemistry*~~
1046 ~~(chemical composition and reactions), 2019.~~

1047 ~~Sweeney, C., Dlugokencky, E., Miller, C. E., Wofsy, S., Karion, A., Dinardo, S., Chang, R. Y. W., Miller, J. B., Bruhwiler,~~
1048 ~~L., Crotwell, A. M., Newberger, T., McKain, K., Stone, R. S., Wolter, S. E., Lang, P. E. and Tans, P.: No significant increase~~
1049 ~~in long term CH₄ emissions on North Slope of Alaska despite significant increase in air temperature: LONG TERM CH₄~~
1050 ~~EMISSIONS ON NORTH SLOPE, *Geophys. Res. Lett.*, 43(12), 6604–6611, doi:10.1002/2016GL069292, 2016.~~

1051 Thonat, T., Saunio, M., Bousquet, P., Pison, I., Tan, Z., Zhuang, Q., Crill, P. M., Thornton, B. F., Bastviken, D.,
1052 Dlugokencky, E. J., Zimov, N., Laurila, T., Hatakka, J., Hermansen, O. and Worthy, D. E. J.: Detectability of Arctic methane

sources at six sites performing continuous atmospheric measurements, *Atmos. Chem. Phys.*, 17(13), 8371–8394, doi:10.5194/acp-17-8371-2017, 2017.

Treat, C. C., Bloom, A. A. and Marushchak, M. E.: Nongrowing season methane emissions-a significant component of annual emissions across northern ecosystems, *Glob Change Biol*, 24(8), 3331–3343, doi:10.1111/gcb.14137, 2018.

Tunnicliffe, R. L., Ganesan, A. L., Parker, R. J., Boesch, H., Gedney, N., Poulter, B., Zhang, Z., Lavrič, J. V., Walter, D., Rigby, M., Henne, S., Young, D., and O'Doherty, S.: Quantifying sources of Brazil's CH₄ emissions between 2010 and 2018 from satellite data, *Atmos. Chem. Phys.*, 20, 13041–13067, <https://doi.org/10.5194/acp-20-13041-2020>, 2020.

Turner, A. J. and Jacob, D. J.: Balancing aggregation and smoothing errors in inverse models, *Atmos. Chem. Phys.*, 15(12), 7039–7048, doi:10.5194/acp-15-7039-2015, 2015.

Turner, A. J., Jacob, D. J., Wecht, K. J., Maasakkers, J. D., Lundgren, E., Andrews, A. E., Biraud, S. C., Boesch, H., Bowman, K. W., Deutscher, N. M., Dubey, M. K., Griffith, D. W. T., Hase, F., Kuze, A., Notholt, J., Ohyama, H., Parker, R., Payne, V. H., Sussmann, R., Sweeney, C., Velazco, V. A., Warneke, T., Wennberg, P. O. and Wunch, D.: Estimating global and North American methane emissions with high spatial resolution using GOSAT satellite data, *Atmos. Chem. Phys.*, 15(12), 7049–7069, doi:10.5194/acp-15-7049-2015, 2015.

~~Turner, A. J., Frankenberg, C., Wennberg, P. O. and Jacob, D. J.: Ambiguity in the causes for decadal trends in atmospheric methane and hydroxyl, *Proc Natl Acad Sci USA*, 114(21), 5367–5372, doi:10.1073/pnas.1616020114, 2017.~~

Turner, A. J., Frankenberg, C. and Kort, E. A.: Interpreting contemporary trends in atmospheric methane, *Proc Natl Acad Sci USA*, 116(8), 2805–2813, doi:10.1073/pnas.1814297116, 2019.

Warwick, N. J., Cain, M. L., Fisher, R., France, J. L., Lowry, D., Michel, S. E., Nisbet, E. G., Vaughn, B. H., White, J. W. C., and Pyle, J. A.: Using $\delta^{13}\text{C-CH}_4$ and $\delta\text{D-CH}_4$ to constrain Arctic methane emissions, *Atmos. Chem. Phys.*, 16, 14891–14908, <https://doi.org/10.5194/acp-16-14891-2016>, 2016.

Wecht, K. J., Jacob, D. J., Frankenberg, C., Jiang, Z. and Blake, D. R.: Mapping of North American methane emissions with high spatial resolution by inversion of SCIAMACHY satellite data: NORTH AMERICA METHANE EMISSION INVERSION, *J. Geophys. Res. Atmos.*, 119(12), 7741–7756, doi:10.1002/2014JD021551, 2014.

~~Worden, J. R., Bloom, A. A., Pandey, S., Jiang, Z., Worden, H. M., Walker, T. W., Houweling, S. and Röckmann, T.: Reduced biomass burning emissions reconcile conflicting estimates of the post 2006 atmospheric methane budget, *Nat Commun*, 8(1), 2227, doi:10.1038/s41467-017-02246-0, 2017.~~

Zavala-Araiza, D., Herndon, S. C., Roscioli, J. R., Yacovitch, T. I., Johnson, M. R., Tyner, D. R., Omara, M. and Knighton, B.: Methane emissions from oil and gas production sites in Alberta, Canada, *Elem Sci Anth*, 6(1), 27, doi:10.1525/elementa.284, 2018.

Zona, D., Gioli, B., Commane, R., Lindaas, J., Wofsy, S. C., Miller, C. E., Dinardo, S. J., Dengel, S., Sweeney, C., Karion, A., Chang, R. Y.-W., Henderson, J. M., Murphy, P. C., Goodrich, J. P., Moreaux, V., Liljedahl, A., Watts, J. D., Kimball, J. S., Lipson, D. A. and Oechel, W. C.: Cold season emissions dominate the Arctic tundra methane budget, *Proc Natl Acad Sci USA*, 113(1), 40–45, doi:10.1073/pnas.1516017113, 2016.

1088 *Supplement of*
1089
1090 **Estimating 2010–2015 Anthropogenic and Natural Methane**
1091 **Emissions in Canada using ECCC Surface and GOSAT Satellite**
1092 **Observations**
1093 **Sabour Baray et al.**

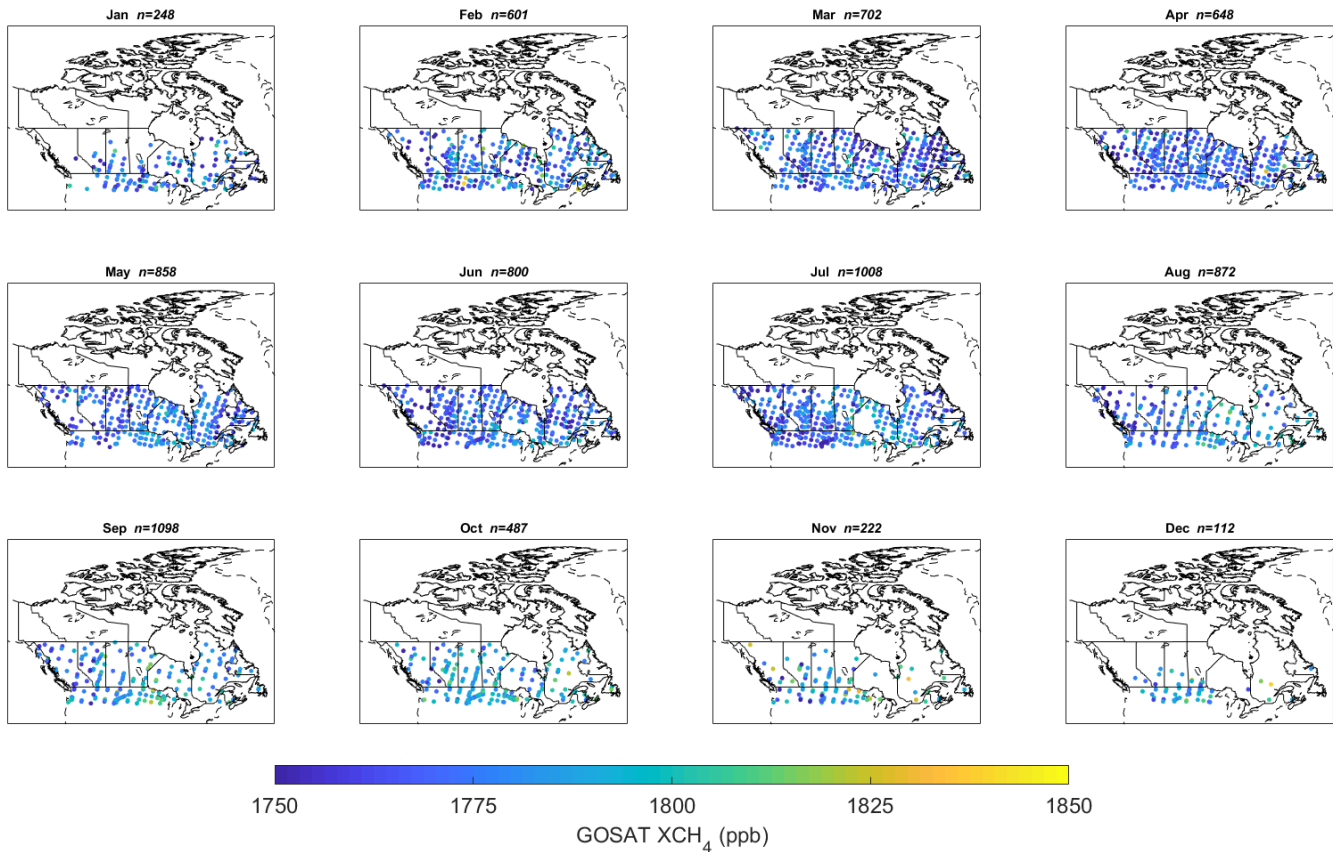
1094 *Correspondence to:* Sabour Baray (sabour@yorku.ca)

1095
1096
1097
1098
1099
1100
1101
1102
1103
1104
1105
1106
1107
1108
1109
1110
1111
1112
1113
1114
1115
1116
1117
1118

1120 **S1.1 Monthly GOSAT Data in the Canadian Domain**

1121 Figure S1 shows the GOSAT data available per month using 2013 as an example year, this corresponds to the data coverage
 1122 shown in Fig. 1 of the main text but highlights the variability in satellite observational coverage over a single year. GOSAT
 1123 data shown passes all quality assurance flags and includes our domain filter to land data that is within 50°W to 150°W
 1124 longitude and 45°N to 60°N latitude. The minimum in December observations ($n=112$) and neighbouring months is due to
 1125 less solar radiation in the winter resulting in less retrievals. Fewer observations cause the inversion to favour the prior state
 1126 of emissions. There are less methane emissions from Canadian wetlands in the coldest months of the winter, and the
 1127 comparison between the prior, the posterior using GOSAT data, and the posterior using ECCC data shows very small
 1128 differences in emissions estimates for these coldest months.

1129



1130

1131 **Figure S1:** GOSAT observations per month in the year 2013 corresponding to Fig. 1 in the main text ($n=7656$ observations
 1132 for the entire year). Observations are filtered to land data that is within 50°W to 150° W longitude and 45°N to 60° N
 1133 latitude.

1134 **S1.2 Sensitivity of Seasonal Emissions to Climatological Data**

1135 We select four climatological stations shown in Table S1 to sample temperature and precipitation data from 2010–2015 in
1136 the four provinces where ~~wetlands emissions~~wetland emissions are concentrated (Alberta, Saskatchewan, Manitoba, and
1137 Ontario). These stations are not exhaustive and are chosen for their proximity to the stations shown in Table 1. Station
1138 measurements are quality-controlled from the National Climate Data Archive from Environment and Climate Change
1139 Canada (Hutchinson et al., 2009).

1140

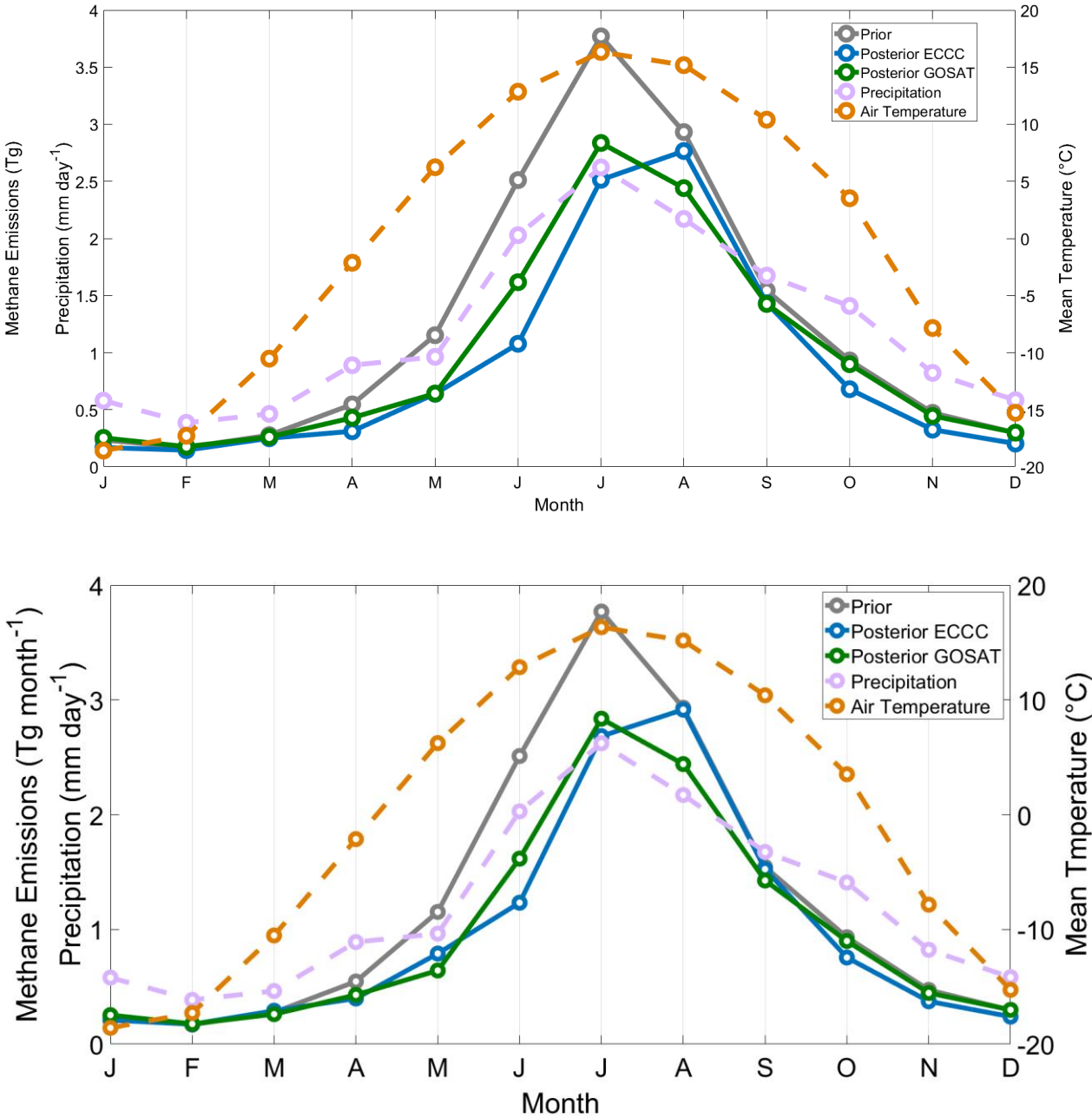
1141 **Table S1:** Climatological sites used for air temperature and total precipitation measurements for the seasonality comparison.

Site Name, Province	Latitude	Longitude
Lac La Biche Climate, Alberta	54.8° N	112.0° W
La Ronge, Saskatchewan	55.1° N	105.3° W
Churchill Climate, Manitoba	58.7° N	94.1° W
Moosonee, Ontario	51.3° N	80.6° W

1142

1143 Figure S2 shows the mean 2010–2015 seasonal pattern of natural methane emissions constrained by ECCC and GOSAT data
1144 corresponding to Fig. 8-6 in the main text. These emissions are compared to monthly mean air temperature and precipitation
1145 averaged over the four climatological stations in Table S1. We consider air temperature a reasonable proxy for the surface
1146 skin temperature that is used in WetCHARTS. Surface skin temperature is itself a proxy for soil temperatures deeper beneath
1147 the surface where methane is produced (Miller et al., 2016). Hence both metrics may be lagging indicators for the peak of
1148 methane emissions. Both air temperature and precipitation show peaks in July which correspond well with the maxima of
1149 methane emissions in the prior from WetCHARTS. Methane emissions in the prior begin to accelerate from March to April,
1150 however for both months air temperature is below freezing. It is not likely that soil temperatures and subsurface soil
1151 temperatures would be above freezing in these months. Air temperature crosses from below 0° to above freezing one month
1152 later from April to May, which corresponds to where the posterior ECCC and GOSAT emissions begin to accelerate. Total
1153 precipitation shows the highest acceleration one month later from May to June. As the peak in July is passed, late-summer
1154 and autumn air temperatures are higher than the months opposite of the peak (August is warmer than June, September is
1155 warmer than May, October is warmer than April). This pattern is corroborated by the precipitation measurements. Air
1156 temperatures go below freezing from October to November. As shown by Zona et al. (2016), “zero-curtain” emissions may
1157 continue even when the soil is at freezing temperatures. This mechanism may be more likely to occur in the months after the
1158 peak if subsurface soils are slower to thaw in the spring and slower to freeze in the autumn. These simple climatological
1159 measurements and the described mechanisms suggested in other studies corroborate our posterior results of lower spring
1160 methane emissions and lower peak methane emissions in the summer. Our results suggest process models may benefit from

1161 better parameterization of possible lagging effects from air temperature and precipitation for Boreal Canada methane
1162 emissions.



1164
1165 **Figure S2:** Mean seasonal pattern of 2010-2015 methane emissions from the prior (gray), posterior constrained with ECCC
1166 data (blue), posterior constrained with GOSAT data (green). This is compared to the seasonal pattern of monthly mean air
1167 temperature (orange, right axis) and precipitation (pink, left axis) from station measurements listed in Table S1. Both air

temperature and precipitation show an asymmetry about the July peak, with higher temperature and precipitation in the fall months than the spring.

S1.3 Evaluation of Bias in the Global Model

In this section we test the GEOS-Chem representation of background methane for both surface ECCC data and column GOSAT data using global and/or boundary condition observations. We show the model representation of methane can be improved using surface and column bias corrections which are presented as the base case in the main text. We test the sensitivity of the posterior emissions to the use of these bias corrections and show the inversions produce consistent results.

S1.3.1 Evaluation of the ECCC Surface Data Background and Bias Corrections

The left panel of Figure S3 shows the comparison of monthly mean GEOS-Chem surface methane concentrations and methane measured at the ECCC station ESP from 2009 to 2015. ESP is located at the west coast of Vancouver Island (Fig. 1); this site is used as an evaluation of background methane and tests the bias in the global model as it is the least sensitive to Canadian emissions due to westerly prevailing winds. The model reliably reproduces surface observations at this station and the growth rate in background methane due to the source-sink imbalance of +13 Tg a⁻¹ in the model global budget (Maasakkers et al., 2019) with a small mean model-observation bias of +5.3 ppb. The right panel of Figure S3 shows the comparison of modelled methane to NOAA aircraft profiles at the same site. Aircraft profiles occur approximately once a month continuously over the study period. The data is not averaged here and is directly compared to GEOS-Chem simulated grid boxes at the pressure level of the measurement. The reduced mean axis (RMA) regression shows a slope of 0.86 and a coefficient of regression $r^2 = 0.67$ which shows a reasonable model representation of the measurements. These statistics are consistent with previous inversions using GEOS-Chem that showed relatively unbiased conditions against NOAA surface stations globally (Turner et al., 2015; Maasakkers et al., 2019). A high resolution inversion over North America over the same 2010–2015 time-period using the same prior have shown adjustments to US emissions near the Canadian border are relatively minimal (Maasakkers et al., 2021), so we treat US emissions as constant in the inversion. The acceptable reproducibility of background methane at this site allows us to attribute much larger differences observed at other sites, up to a maximum of ~1000 ppb in the summer (Figure 4), to Canadian emissions which are optimized using Canadian observations while holding other global emissions constant.

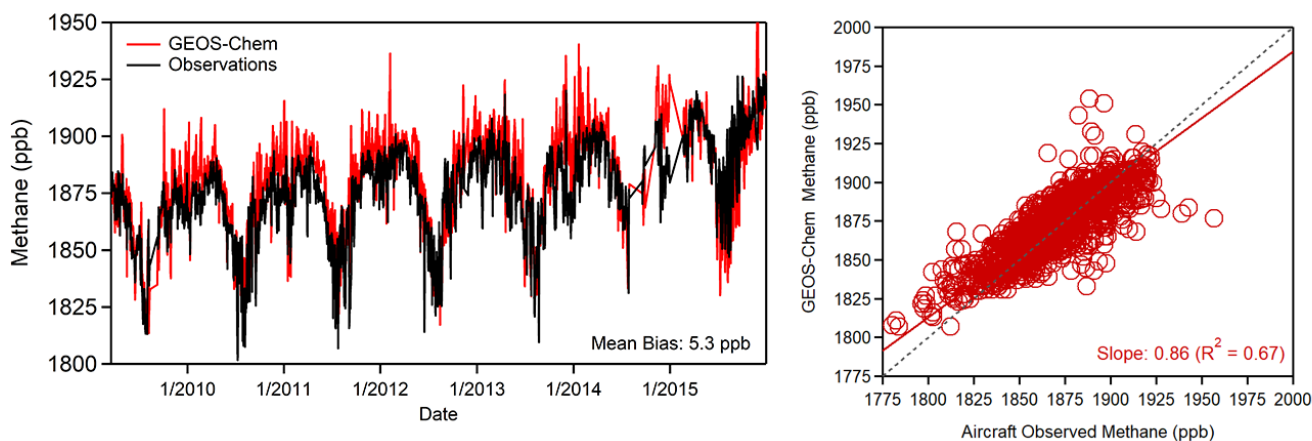


Figure S3: Time-series comparison (left) from 2009–2015 of surface GEOS-Chem simulated methane (red) and measured in situ methane (black) at site ESP off the west coast of British Columbia. Comparison to NOAA aircraft profiles (right) from 2009–2015 at the same site using a reduced major axis (RMA) regression along with the 1:1 line (black).

While the mean model bias of +5.3 ppb in Figure S3 shows a net over-estimation in the model, the later years 2014 and 2015 show a model underestimation primarily due to underestimated tropical emissions (Maasakkers et al., 2019). This positive-to-negative difference in the model background can project errors onto the trend of ECCC-constrained emissions. This is addressed by removing the annual-mean background bias at the Canadian boundary conditions from the observation vector. We use the westmost boundary condition site ESP and a second northernmost background site at Alert, Nunavut (ALT) to diagnose errors in the methane background and show the annual mean model-observation differences in Table S2. The average of these two sites is used to adjust the model for the base-case ECCC inversion in the main text. In Section 1.3.2 of the Supplement, we test the sensitivity of the posterior emissions to the use of these various background corrections and show consistent results, with the background-adjusted inversion showing slightly more agreement with the GOSAT inversion.

Table S2: Mean annual model-measurement differences at background sites ESP and ALT.

Mean Model–Measurement Difference (ppb)			
Year	ESP ^a	ALT ^b	Average ^c
2010	+5.0	+8.8	+6.9
2011	+5.8	+8.5	+7.2
2012	+3.6	+5.9	+4.8
2013	+2.6	+10.5	+6.6

	<u>2014</u>	<u>+2.1</u>	<u>+11.3</u>	<u>+6.7</u>
	<u>2015</u>	<u>-6.9</u>	<u>-4.7</u>	<u>-5.8</u>
1214	<u>^aSite ESP is located at 49.38°N, 126.54°W, and is the westernmost boundary condition for Canada.</u>			
1215	<u>^bSite ALT is located at 82.45°N, 62.51°W, and is the northernmost boundary condition for Canada.</u>			
1216	<u>^cThe average is used in the base-case ECCC inversions shown in the main text. The three alternatives: adjustments using</u>			
1217	<u>ESP, ALT and no background adjustments are shown as sensitivity tests in the Supplement.</u>			
1218	<u>S1.3.2 Sensitivity Tests of ECCC-Constrained Emissions</u>			
1219	<u>Figure S4 shows the sensitivity tests comparing the ECCC inversions with an unadjusted model to the two background-</u>			
1220	<u>adjusted ECCC inversions using either the mean yearly bias from ESP or ALT. The three inversions are consistent with each</u>			
1221	<u>other within their error intervals, but the adjusted ECCC inversions show improved agreement with the GOSAT results. For</u>			
1222	<u>anthropogenic sources, the mean yearly emissions are $6.0 \pm 0.4 \text{ Tg a}^{-1}$ in the unadjusted ECCC inversion, $6.1 \pm 0.4 \text{ Tg a}^{-1}$</u>			
1223	<u>with the ESP-adjusted ECCC inversion, and $6.0 \pm 0.4 \text{ Tg a}^{-1}$ with the ALT-adjusted inversion. For natural sources, the mean</u>			
1224	<u>yearly emissions are $10.5 \pm 1.9 \text{ Tg a}^{-1}$ in the unadjusted ECCC inversion, $12.0 \pm 1.4 \text{ Tg a}^{-1}$ in the ESP-adjusted ECCC</u>			
1225	<u>inversion, and $11.0 \pm 1.2 \text{ Tg a}^{-1}$ in the ALT-adjusted ECCC inversion. The background-adjusted inversions show higher</u>			
1226	<u>natural emissions in the years 2010–2014 compared to the unadjusted case, and lower natural emissions in 2015 due to the</u>			
1227	<u>negative background bias that is removed. The background-adjusted inversions show better agreement with the GOSAT</u>			
1228	<u>mean yearly natural emissions of $11.7 \pm 1.2 \text{ Tg a}^{-1}$. In addition, the trend in natural emissions over this time period is reduced</u>			
1229	<u>by 40–45% from 1.0 Tg a^{-1} in the unadjusted inversion to $0.55\text{--}0.60 \text{ Tg a}^{-1}$ in the adjusted inversions. These results show that</u>			
1230	<u>the background error does not largely affect the average 2010–2015 results regarding the overall increase in anthropogenic</u>			
1231	<u>emissions and decrease in natural emissions. Correcting for the model background minimizes the projection of under-</u>			
1232	<u>estimated tropical emissions onto the Canadian fluxes in the later years, which improves the consistency with the GOSAT</u>			
1233	<u>inversion and significantly reduces the presence of a large trend that was not corroborated by GOSAT.</u>			
1234				

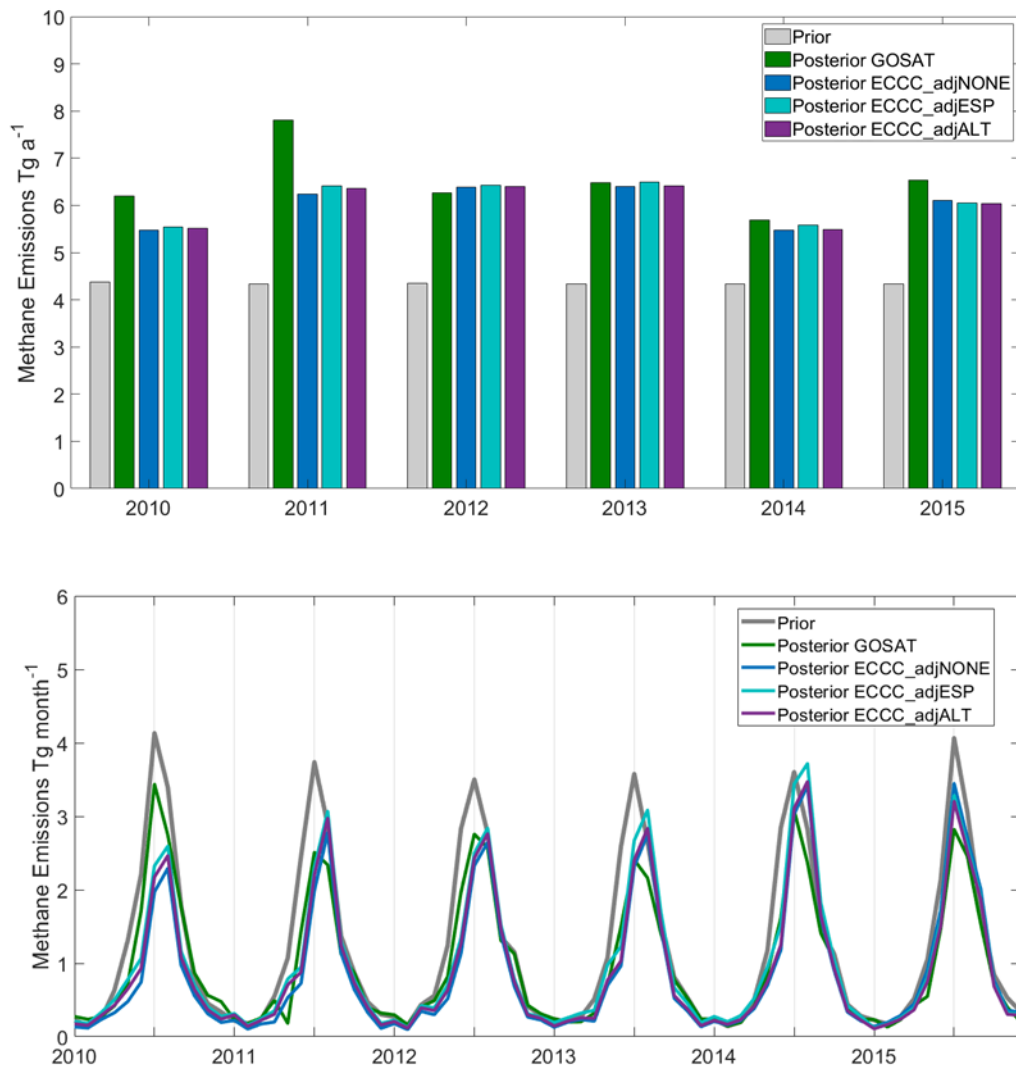


Figure S4: Sensitivity analysis of inversion results depending on the use of model background correction for surface pixels. Referred to as the monthly inversion, this approach optimizes annual total Canadian anthropogenic emissions (top) and monthly total natural emissions (bottom) in an $n = 78$ state-vector element setup. The prior emissions (gray) are compared to the posterior results using GOSAT (green), and the posterior using ECCC data with an unadjusted background (blue), ECCC data using a background adjusted according to the yearly difference at ESP (teal) and ALT (purple) from Table S2.

To address the possibility of US emissions influencing the posterior results near the Canadian border, we show a sensitivity test where the two stations most influenced by cross-border transport, Egbert (EGB) and Sable Island (SBL) are removed from the ECCC inversion. Figure S5 shows posterior-ECCC emissions where EGB and SBL (at latitudes of 44.2°N and

43.9°N, respectively) are removed (note in this case, the background is left un-adjusted to avoid overlap in the issues). The mean of anthropogenic emissions in the inversion without these stations is $6.4 \pm 0.6 \text{ Tg a}^{-1}$, and the mean of natural emissions is $10.9 \pm 1.5 \text{ Tg a}^{-1}$. These results are similar to the posterior from the unadjusted ECCC inversion ($6.0 \pm 0.4 \text{ Tg a}^{-1}$ anthropogenic, $10.5 \pm 1.9 \text{ Tg a}^{-1}$ natural) and the GOSAT inversion ($6.5 \pm 0.7 \text{ Tg a}^{-1}$ anthropogenic, $11.7 \pm 1.2 \text{ Tg a}^{-1}$ natural). This sensitivity test shows that the US signal does not substantially affect the results from the optimization of large biases observed by Canadian observations due to Canadian emissions.

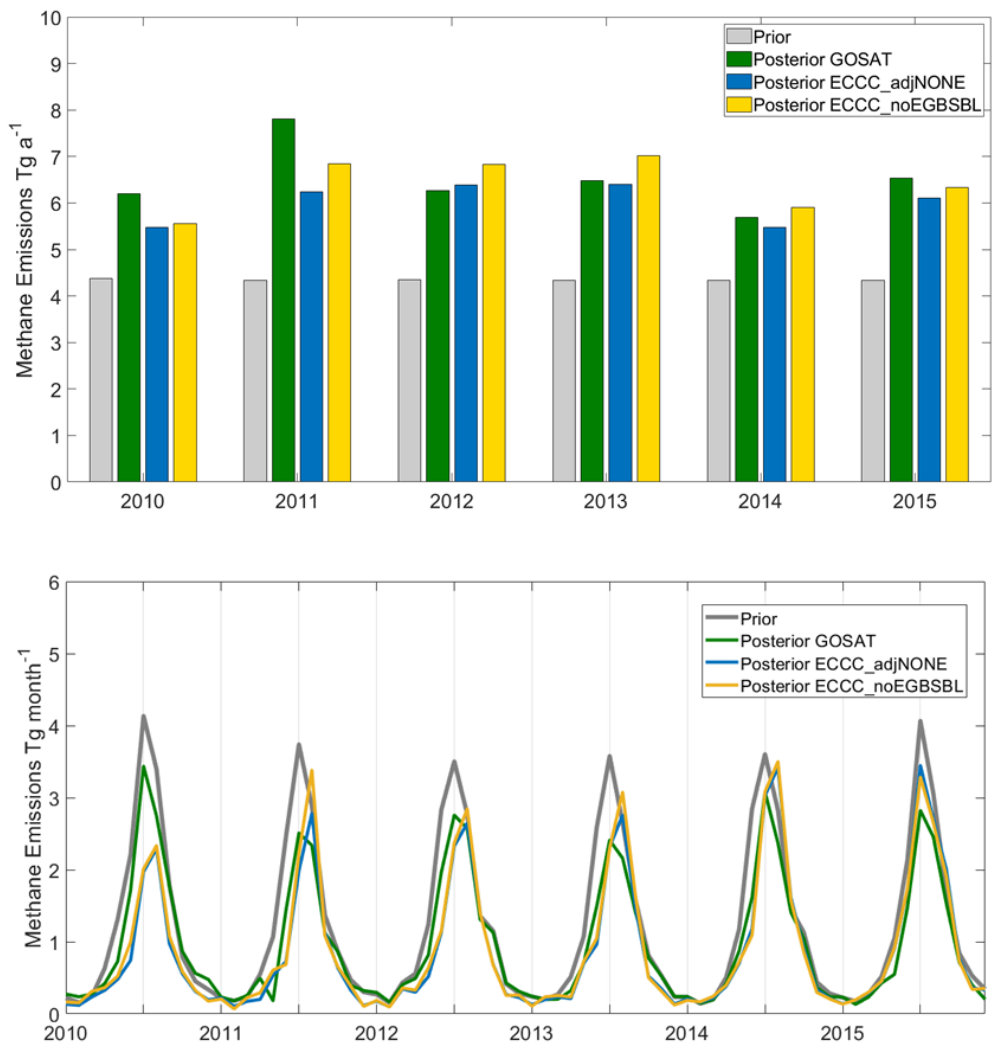


Figure S5: Sensitivity analysis of inversion results depending on the inclusion of sites EGB and SBL which are sensitive to cross-border transport from the United States. Similar to Fig. S4, the monthly inversion optimizes annual total Canadian

1255 anthropogenic emissions (top) and monthly total natural emissions (bottom) in an $n = 78$ state-vector element setup. The
1256 prior emissions (gray) are compared to the posterior results using GOSAT (green), and the posterior using ECCC data
1257 including all sites (blue) and ECCC data excluding EGB and SBL (yellow).

1258 **S1.3.3 Evaluation of Global GOSAT Data and Bias Corrections**

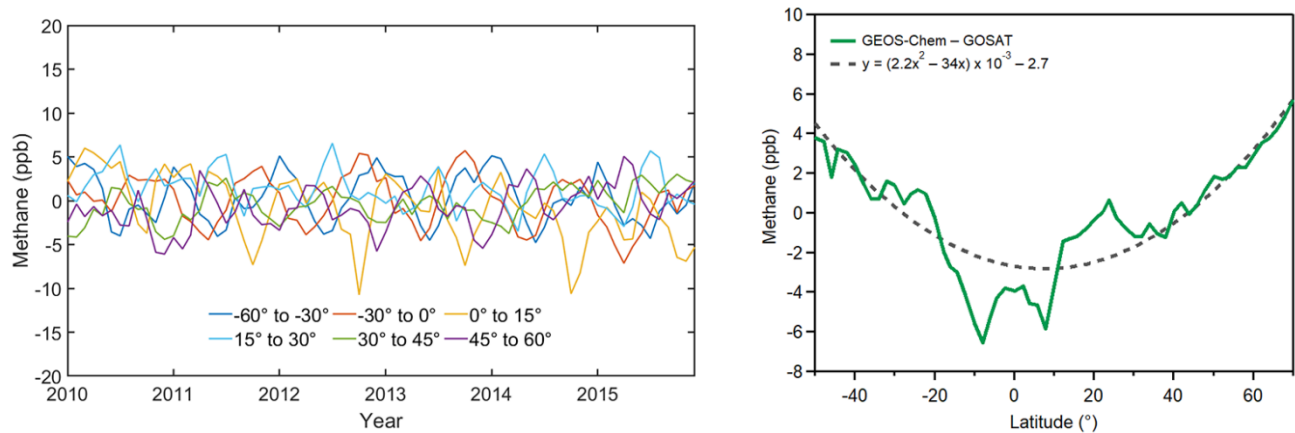
1259 The GEOS-Chem simulation of column averaged methane shows three global biases previously discussed in the literature:
1260 (1) a latitude-dependent bias, (2) a seasonal bias and (3) a background change for 2014 and 2015 due to differences in the
1261 global source-sink imbalance in these two years (Turner et al., 2015; Saad et al., 2018; Maasakkers et al., 2019; Stanevich et
1262 al., 2020). We apply these corrections to the simulated column of methane on a global basis to produce an unbiased
1263 background for our target Canadian domain (45° N to 60° N, 50° W to 150° W). The latitude-dependent bias (1) is likely due
1264 to excessive polar stratospheric transport (Stanevich et al., 2020). We correct for this bias by fitting the model-GOSAT
1265 difference for global $2^{\circ} \times 2.5^{\circ}$ grid cells according to a second-order polynomial as shown in Figure S6:

$$1267 \xi = (2.2\theta^2 - 34\theta) \times 10^{-3} - 2.7 \quad (\text{S1s})$$

1268
1269 where ξ is the resulting bias correction in ppb and θ is latitude in degrees. The correction in this work for the latitude bins of
1270 our target domain (45° N to 60° N) is between 0.3 to 2.9 ppb. This correction is lower than what has been shown previously
1271 (Turner et al., 2015; Maasakkers et al., 2019) and we attribute this improvement to our use of a $2^{\circ} \times 2.5^{\circ}$ gridded simulation
1272 instead of a $4^{\circ} \times 4.5^{\circ}$ as recommended by Stanevich et al. (2020) to reduce transport errors. A seasonally oscillating bias (2)
1273 remains after this correction. The seasonal bias has an amplitude of ± 4 ppb with repeating maxima in June and minima in
1274 December. It is not clear whether this seasonal bias is due to emissions and/or transport errors. In our base case we remove
1275 the seasonal bias on a monthly basis following Maasakkers et al. (2019) and show a sensitivity test without the correction for
1276 our inversion of monthly natural emissions in Canada (Supplement 1.3.4). Inversion results using GOSAT data with and
1277 without bias corrections in the model simulation of total column methane do not show major differences (Fig. S7). These
1278 scenarios all show agreement with the posterior emissions adjustments determined using unadjusted ECCC in situ data –
1279 which is a useful benchmark since modelled methane at the surface is not subject to any bias corrections. The background
1280 change (3) that appears in the simulated methane column from 2014 onwards is corrected for in Maasakkers et al. (2019) by
1281 optimizing emissions, emissions trends and trends in OH using a global inversion. In that work correction factors do not
1282 appear over Canada and the United States that would significantly influence the global change in atmospheric methane, and
1283 the main adjustment in 2014 and 2015 were to tropical wetlands emissions wetland emissions and OH. Here we treat this as a
1284 background change and apply a uniform correction to the simulated column since emissions outside of Canada and changes
1285 in OH are treated as fixed in our Canada-focused inversion. The background change (3) is 5 ppb in 2014 and 10 ppb in 2015.
1286 The right panel of Figure S6 shows the latitude dependent bias correction and the left panel shows the resulting global time-
1287 series of GEOS-Chem total column methane from 2010–2015 after corrections are applied. The global GEOS-Chem –

1288 GOSAT differences in the methane column can be limited globally to within 10 ppb without including the seasonal bias
 1289 correction, and within 5 ppb with its inclusion. This shows a steady background in methane for the entire time period from
 1290 2010–2015 so global emissions do not affect the optimization of Canadian emissions. While biases within 10 ppb have been
 1291 treated as acceptable for methane inversions (Buchwitz et al., 2015), we evaluate our GOSAT inversion results against
 1292 inversions with independent ECCC in situ measurements that do not require any bias corrections in the model to produce
 1293 more robust emissions estimates.

1294



1295

1296

1297 **Figure S6:** Time series (left) from 2010–2015 of the difference between GEOS-Chem simulated total column methane and
 1298 GOSAT observations after applying bias corrections, showing a consistent global background for methane. Data used in the
 1299 inversion for Canada is from 45° N to 60° N (purple line) and shows acceptable differences within 5 ppb over the entire
 1300 global latitude band. To produce the left figure, the latitude-dependent bias (right) is shown with the polynomial correction
 1301 that is applied (gray dash) that is within a magnitude of 0.3 to 2.9 ppb for the same latitude.

1302

1303 **S1.3.4 Sensitivity Tests of GOSAT-Constrained Emissions ~~to GEOS-Chem Column Bias Corrections~~**

1304 We test the sensitivity of the posterior GOSAT-constrained methane emissions in our analysis to the use of latitude-
 1305 dependent and seasonal bias corrections in the GEOS-Chem simulated total column of methane. The latitude-dependent bias
 1306 correction has a magnitude less than 3.5 ppb for our domain of interest (45 to 60°N). On a global basis the seasonal bias
 1307 correction has an amplitude of ± 4 ppb with a maximum in June and a minimum in December. Figure [S3–S7](#) shows the
 1308 sensitivity of posterior monthly emissions to these bias corrections using 2013 as an example. We show four versions of the
 1309 posterior methane emissions using GOSAT data: GOSAT11 (green) is the base case which applies the latitude-dependent
 1310 bias correction and the seasonal bias correction, GOSAT10 (purple) applies the latitude-dependent bias correction and does
 1311 not apply the seasonal correction, GOSAT01 (orange) does not apply the latitude-dependent bias correction and applies the

seasonal correction, and GOSAT00 (light blue) uses neither bias correction. The range of emissions from all four examples is 9.7 – 10.7 Tg a⁻¹, which are all consistent with the unadjusted ECCC emissions of 10.0 Tg a⁻¹ and lower than the prior emissions of 14.3 Tg a⁻¹. Not applying the latitude-dependent bias correction results in a decrease in the resulting emissions and maintains the same seasonal pattern. Not applying the seasonal bias correction results in a change in the temporal distribution of emissions that better matches the August peak in the posterior with ECCC data. Emissions are lower than the base case in the spring and higher than the base case in autumn. This change enhances the autumn-shift in emissions that has been described in [Section 4.3.2 of the main text](#). While this may be more consistent with our interpretations, it is not clear whether the difference is due to emissions or transport biases. Stanevich et al. ([2019](#)[2020](#)) showed that the latitude dependent bias is most likely due to excessive polar stratospheric transport at high latitudes. If the seasonal bias is indeed due to mischaracterized natural emissions, it is not clear why the bias would be equally large in December (–4 ppb) as June (+4 ppb) on a global basis. The magnitude of natural emissions in December is much lower than June and emissions mischaracterization would not itself produce an equally large bias as the largely overestimated summertime emissions. Our analysis with ECCC data shows most of the adjustments to wetlands are in the peak of summer with some extension into the autumn. These results show that the bias corrections produce minor differences in the magnitude and seasonal pattern of emissions.

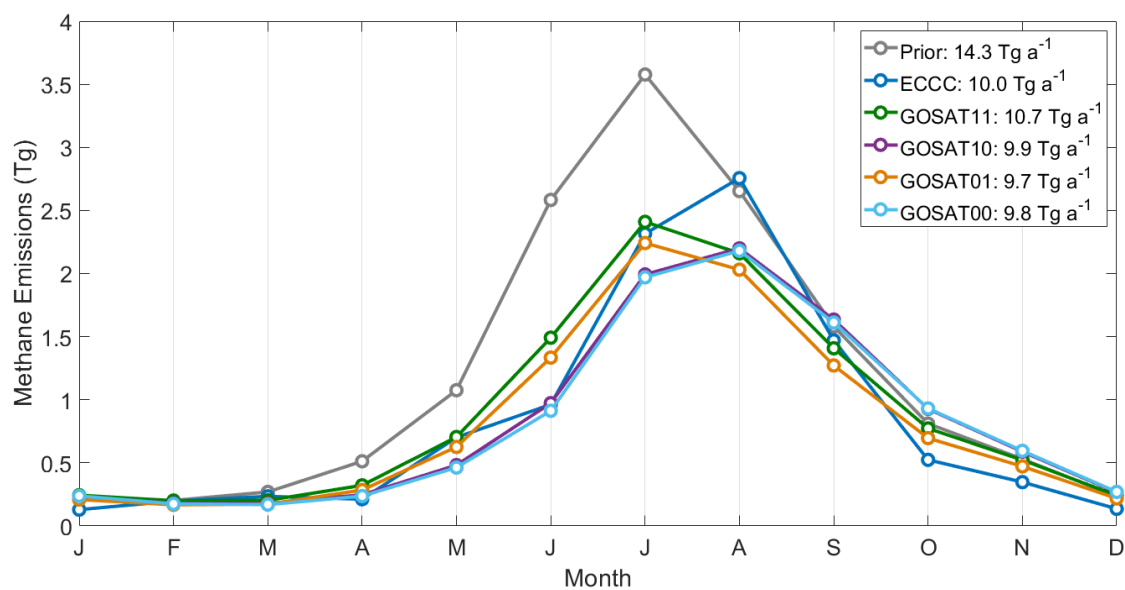


Figure S3S7: Sensitivity of 2013 posterior GOSAT constrained methane emissions to bias corrections used in the GEOS-Chem simulated total column of methane. For comparison, the prior in 2013 (gray) and the posterior in 2013 constrained by ECCC data (unadjusted, blue) are shown. The digits in the GOSAT label represent the binary use of bias corrections (1 = applied, 0 = not applied). The first digit corresponds to the use of the latitude bias correction, the second digit corresponds to

the use of the monthly bias correction, hence GOSAT11 is the base case that applies both bias corrections and GOSAT00 is the case with no bias corrections applied.

S1.3.5 Evaluation of the Prior and Posterior Model Fluxes Using Global Observations Outside of the Canadian Domain

The inverse model design in this study uses a simplified approach, where Canadian emissions are optimized using only observations in Canada. The results from this approach may be sensitive to errors in the global model projected onto the Canadian domain if errors in the global model are sufficiently large relative to the local biases in Canada (Figure 4 in the main text) and the observational error used in the inversion procedure (16 ppb for GOSAT, 65 ppb for ECCO). Figure S8 shows an independent evaluation of the prior global model and the posterior in this study to 2010–2015 background observations from the NOAA cooperative flask sampling network (<https://gml.noaa.gov/ccgg/flask.html>) outside of the Canadian domain. We use a simple version of the posterior where Canadian anthropogenic emissions are scaled up by 37% to 6.0 Tg a⁻¹ and natural emissions are scaled down by 24% to 11.2 Tg a⁻¹. This captures the central results of the monthly, sectoral, and provincial inversions in the main text and avoids a large number of model comparisons. The analysis shows that the prior model reasonably reproduces the methane background, and the posterior from adjusted Canadian emissions does not degrade this result. In the reduced-major axis regression, the prior r^2 coefficients are in the range of 0.77–0.92 and the prior slopes are in the range of 0.94–0.97 across the three surface, ship, and aircraft datasets. In the posterior, the r^2 is in the range of 0.76–0.91 and the slope is in the range of 0.93–0.96. The posterior reflects a decrease of 2.0 Tg a⁻¹ in the global budget due to a net decrease in Canadian emissions, which is shown in the improvements to the mean bias comparisons. This decrease in emissions slightly improves the global model agreement with independent data in the years 2010–2013 (since the model overestimates emissions) and slightly degrades the agreement in 2014–2015 (since the model underestimates tropical emissions), which is understandable considering only Canadian emissions are adjusted and the global model is not optimized. A net decrease in Canadian emissions is consistent with previous global inversion studies using GEOS-Chem (Turner et al., 2015; Maasakkers et al., 2019). The results from the Canada-focused inversion with subnational details in this study show that the net-decrease in Canadian natural emissions masks an increase in anthropogenic emissions in Western Canada which should be considered in global inverse studies.

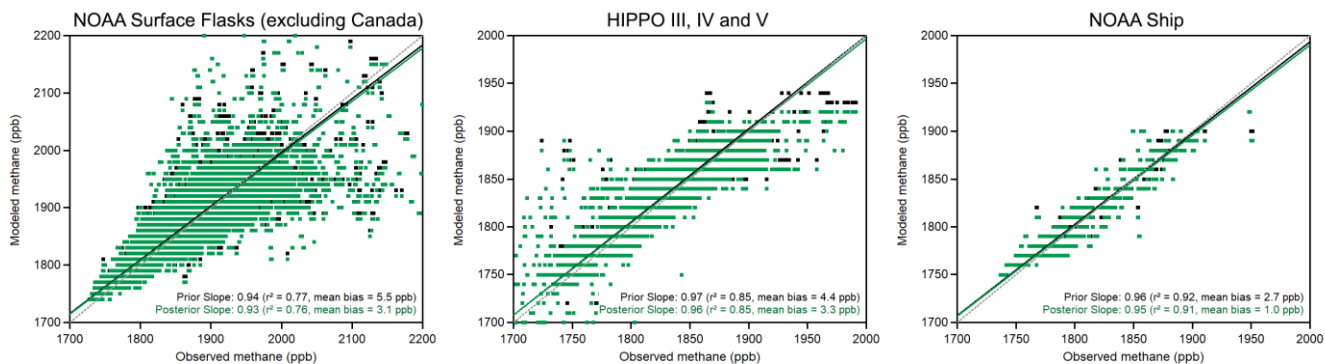
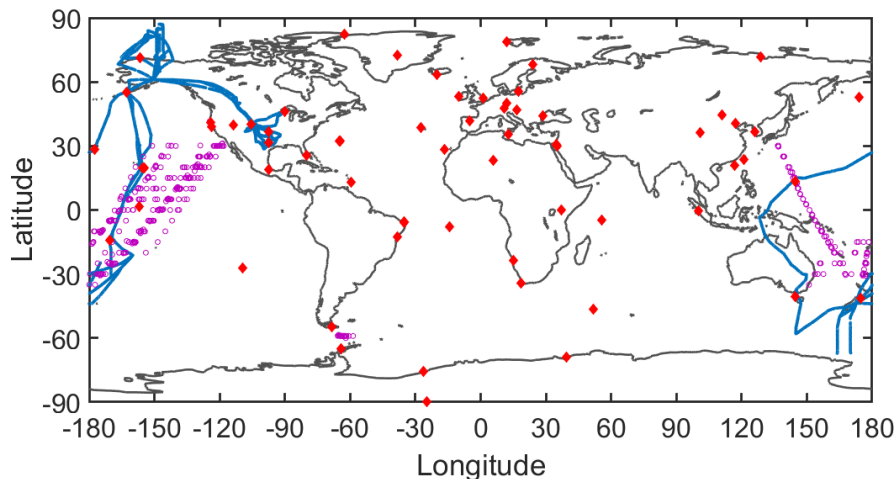


Figure S8: Model comparison to independent NOAA observations globally from 2010–2015. The top panel shows data used in the global model comparison. Red diamonds indicate NOAA surface flasks, purple circles indicate NOAA ship data, and blue lines indicate HIPPO III, IV and V aircraft data. Comparison of the prior and posterior emissions in GEOS-Chem is shown using a reduced-major axis regression against NOAA Surface flasks (bottom-left), HIPPO III, IV and V aircraft data (bottom-middle), and NOAA Ship data (bottom-right).

S1.4 Diagnostics of Sectoral and Provincial Inversions

In this analysis we first evaluate the correlations and/or independence of the state vector elements from the posterior error covariance matrix $\hat{\mathbf{S}}$ as follows (Heald et al., 2004):

$$r_{ij} = \frac{\hat{s}_{ij}}{\sqrt{\hat{s}_{ii}} \sqrt{\hat{s}_{jj}}} \quad (24s)$$

1377

1378 The error-normalized posterior correlation matrix \mathbf{r} provides information on the independence of the state vector elements.
 1379 This is corroborated by the averaging kernel matrix \mathbf{A} which shows which state vector elements contain independent pieces
 1380 of information, with the trace of \mathbf{A} providing the total degrees of freedom for signal for the inversion. To further evaluate the
 1381 signal-to-noise ratio of the observation-constrained state vector elements and their independence from each other we use an
 1382 eigenanalysis. The Jacobian matrix \mathbf{K} is normalized about the observational and prior error covariance matrices as follows
 1383 (Rodgers, 2000):

1384

$$1385 \quad \check{\mathbf{K}} = \mathbf{S}_o^{-1/2} \mathbf{K} \mathbf{S}_a^{1/2} \quad (32s)$$

1386

1387 The singular value decomposition of $\check{\mathbf{K}}$ gives its rank which is the number of singular values greater than one. The singular
 1388 values also correspond to the signal-to-noise ratio of state vector elements and hence quantify the strength of the
 1389 observational constraints on individual emissions categories.

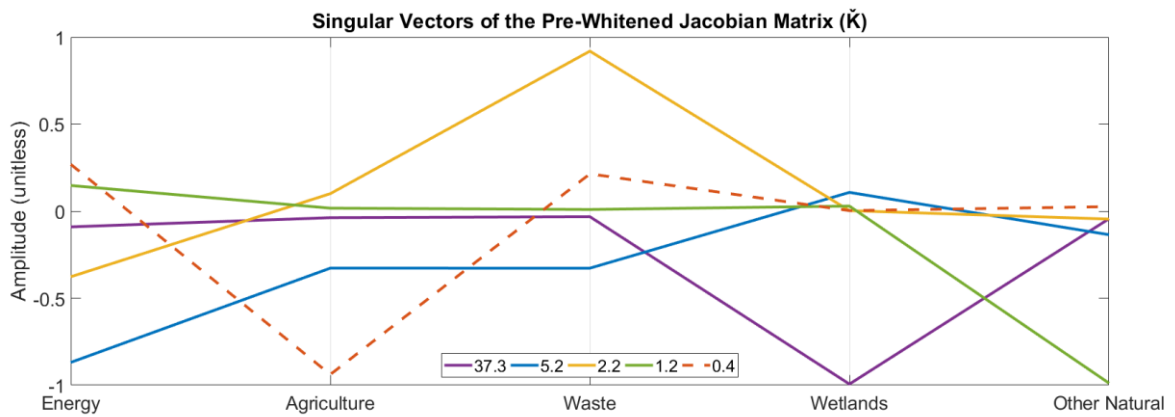
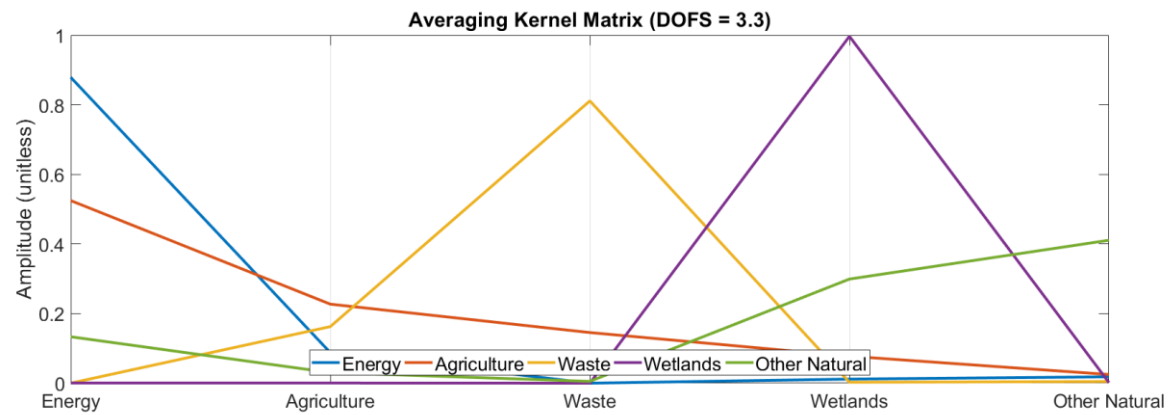
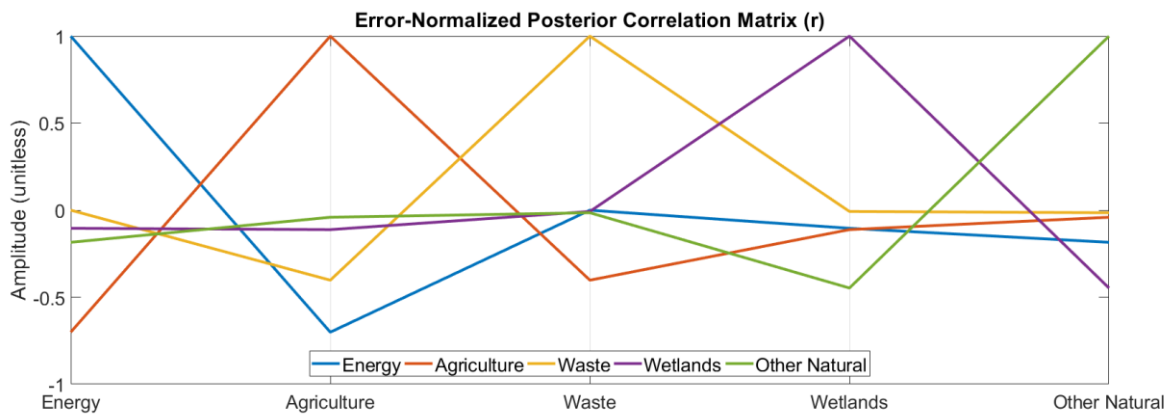
1390

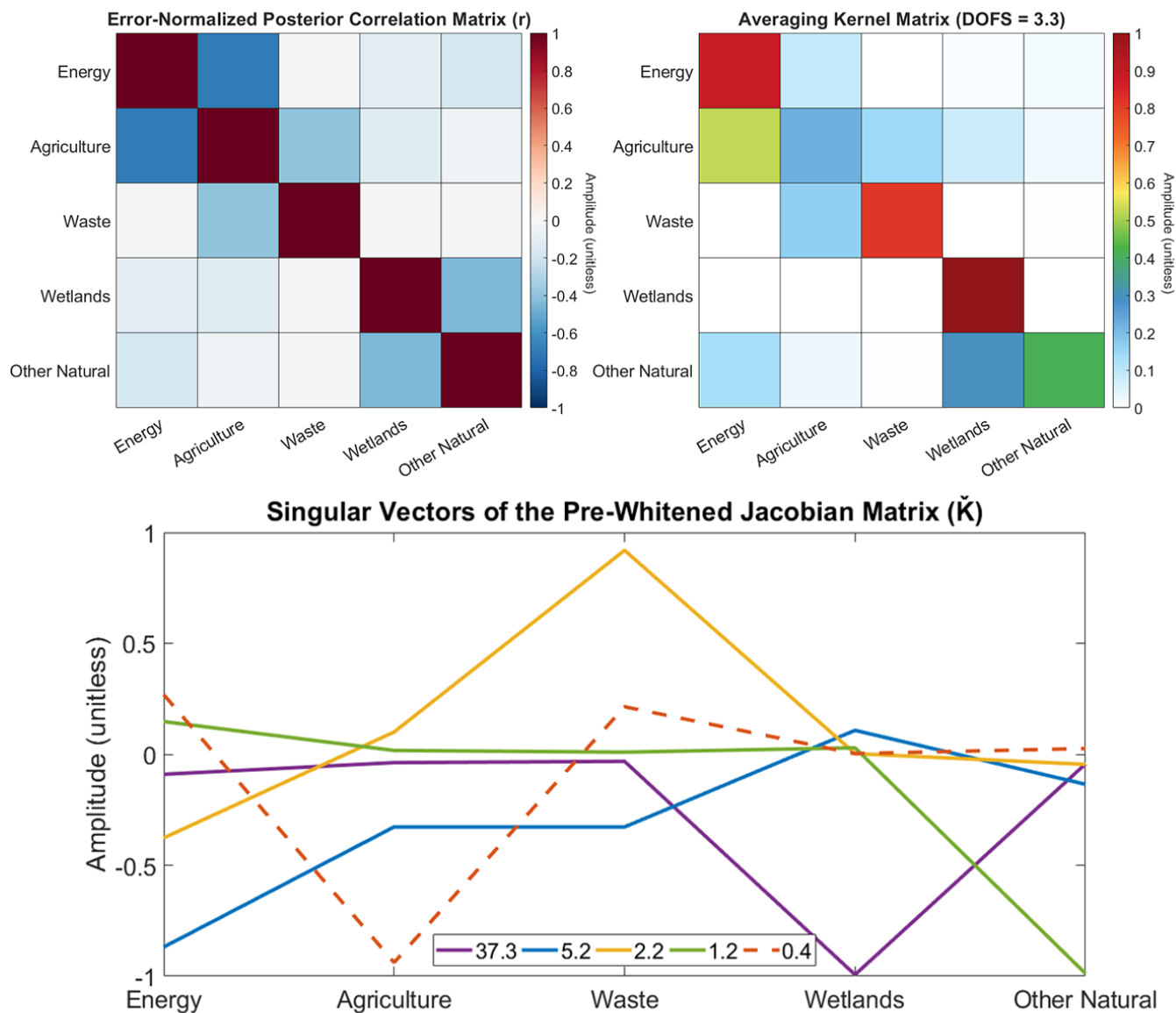
1391 Figure S94 shows this series of diagnostics for the sectoral (5 state vector element) inversion and Figure S105 shows the
 1392 same analysis for the provincial (16 state vector element) inversion. Figure S4-S9 (top left) shows the error-normalized
 1393 correlation matrix for the sectoral inversion. The most important result is that the primary source of natural emissions,
 1394 wetlands (purple line), is not correlated with the primary source of anthropogenic emissions, energy (blue line). Within the
 1395 anthropogenic category however, we see that energy is strongly correlated with agriculture, showing that these two elements
 1396 cannot be distinguished by the observation system. For natural emissions, other natural sources are weakly correlated with
 1397 wetlands and are not completely independent. Emissions from waste are shown to be slightly more independent and can be
 1398 distinguished from the other sources. The averaging kernel matrix corroborates this result, and shows the three independent
 1399 pieces of information are energy, wetlands and waste, with partial information content from other natural sources and a lack
 1400 of information on agriculture. The singular values show strong constraints on wetlands with a signal-to-noise ratio of 37.3,
 1401 and strong constraints on energy with a signal-to-noise ratio of 5.2. Waste sources are 2.2, other natural are 1.2 and
 1402 agriculture is below the noise at 0.4. These diagnostics demonstrate that a joint ECCC in situ and GOSAT satellite inversion
 1403 system can successfully provide constraints on and distinguish the three major categories of methane emissions in Canada:
 1404 wetlands, energy and waste. Emissions from agriculture cannot be distinguished in this system and should be aggregated with
 1405 energy, this is likely because of the strong spatial overlap between these emissions in Western Canada and the lower signal
 1406 from lower magnitude agriculture emissions. Emissions from other natural sources (biomass burning, seeps, and termites)
 1407 also are at the noise and should be aggregated with wetlands. This is because minor natural sources are much lower in
 1408 magnitude (0.8 Tg a⁻¹ out of 14.8 Tg a⁻¹) and also show spatial overlap with wetlands.

1409

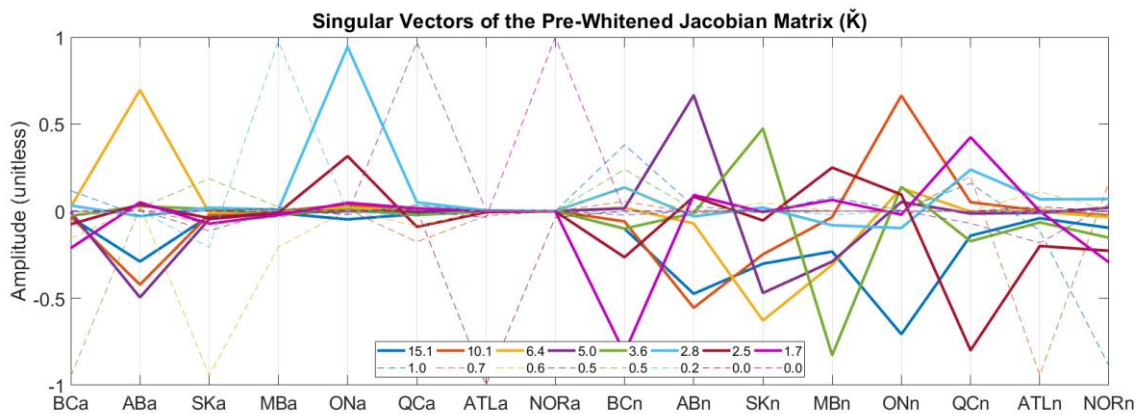
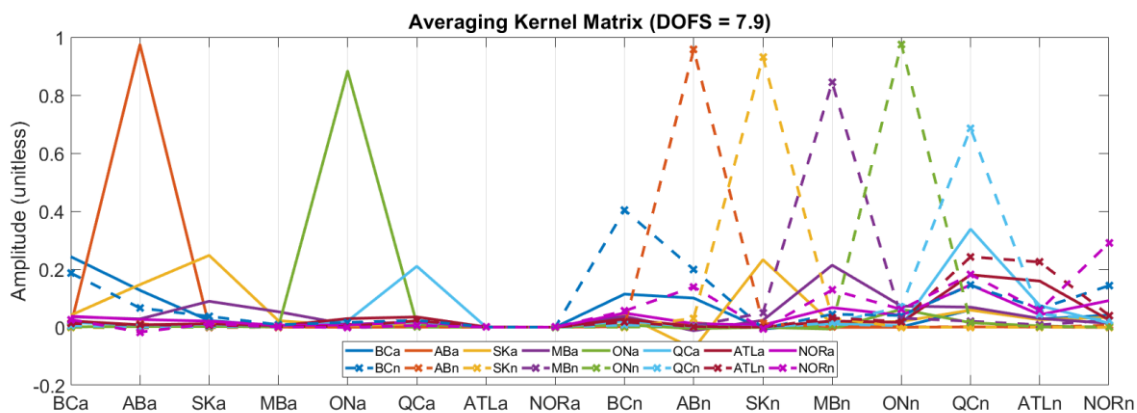
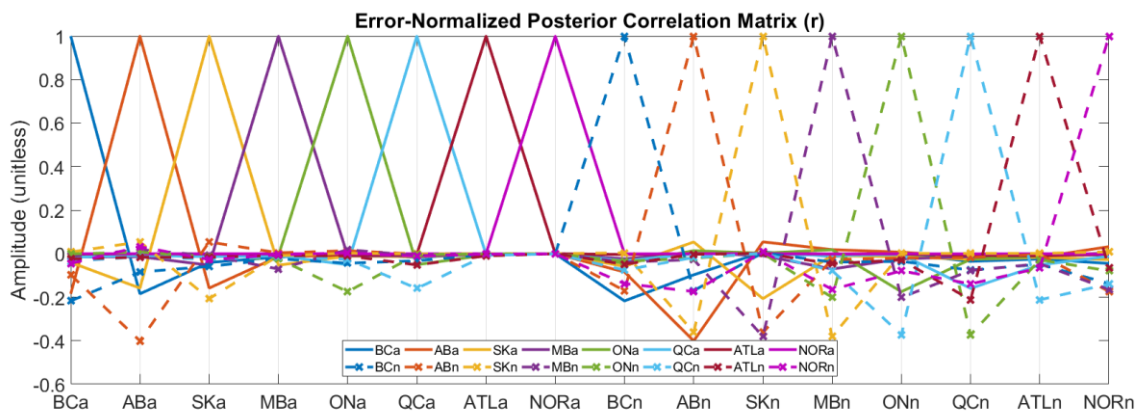
Figure S10~~5~~ shows the diagnostics on the provincial (16 state vector element) inversion. This choice of state vector elements challenges the observing system and results in a largely underdetermined solution. These diagnostics allow us to identify where the limitations of the ECCC + GOSAT observing system are. The posterior error correlation matrix \mathbf{r} shows the provincial emissions are somewhat correlated a) between anthropogenic/natural emissions of the same province and b) with neighboring provinces in the same category of emissions. For example, AB anthropogenic emissions ~~(solid orange line)~~ show a small inverse correlation with AB natural emissions ~~(dashed x orange line)~~. ~~The solid orange line~~ AB anthropogenic emissions also show a small correlation with the anthropogenic emissions of nearby provinces BC and SK. For the natural emissions, ~~the dashed lines corresponding to~~ natural emissions within a province in most cases extend correlations into the provinces to the east and west. These correlations are not as large as the case of Energy and Agriculture emissions in Fig. S4S9, and show a more moderate influence of nearby provinces on the optimized emissions. The primary limitation of the provincial inversion is the inability to distinguish provinces with a very small magnitude of emissions. This is shown in the averaging kernel matrix, which has a degrees of freedom for signal of 7.9 out of 16 elements. The 6 regions that are best constrained are AB anthropogenic, ON anthropogenic, AB natural, SK natural, MB natural, and ON natural, with partial constraints on BC anthropogenic, SK anthropogenic, QC anthropogenic, BC natural, QC natural and NOR natural. The singular vectors corroborate this result and show that there are 8 regions that are above the noise and 8 that are at or below the noise. The best constraints on anthropogenic emissions are in Alberta, with a signal to noise ratio as good as 15.1 (solid blue line), followed by Ontario (2.5-2.8).

These diagnostics show that the ECCC+GOSAT observing system for Canada is limited in its ability to characterize agricultural emissions, and somewhat limited in its ability to characterize non-wetlands natural emissions. Hence we present Energy+Agriculture and Wetlands+Other Natural together for our conclusions. More precise and more dense measurements at a finer scale would better disaggregate these sources, although the use of the precise in situ data is primarily limited by the model error (Section 2.3 of the main text). In the provincial inversion, the observing system provides good constraints on anthropogenic emissions from AB and ON and is capable of distinguishing these emissions from natural sources in the same province. However, anthropogenic sources from other provinces with much lower emissions cannot be distinguished. Natural emissions can be characterized from the provinces that are most responsible for ~~wetlands emissions~~ wetland emissions (AB, SK, MB, ON), however the observing system struggles in Atlantic and Northern Canada where the surface and satellite observations we use are limited. The emissions adjustments to state vector elements beneath the noise are due to aliasing with other sources and compensation effects due to interprovincial transport. We limit our ~~rt~~ conclusions to simple interpretations, we use the limited provincial inversion for spatial attribution to show higher posterior anthropogenic emissions are primarily from the total in Western Canada (BC+AB+SK+MB), and not emissions in Central Canada (ON+QC).





1445
 1446 **Figure S4S9:** Diagnostics of the sectoral inversion used to evaluate the independence and information content of the 5 state
 1447 vector elements. The error-normalized posterior correlation matrix (top left) shows the correlations between elements. The
 1448 averaging kernel matrix (middletop right) shows where the independent pieces of information are (DOFS = 3.3). The
 1449 singular vector decomposition of the pre-whitened jacobian (bottom) quantifies the signal-to-noise ratio of the significant
 1450 elements – these are the singular values listed above one (4 in total). The singular vector below noise (agriculture) is shown
 1451 as a dashed line.



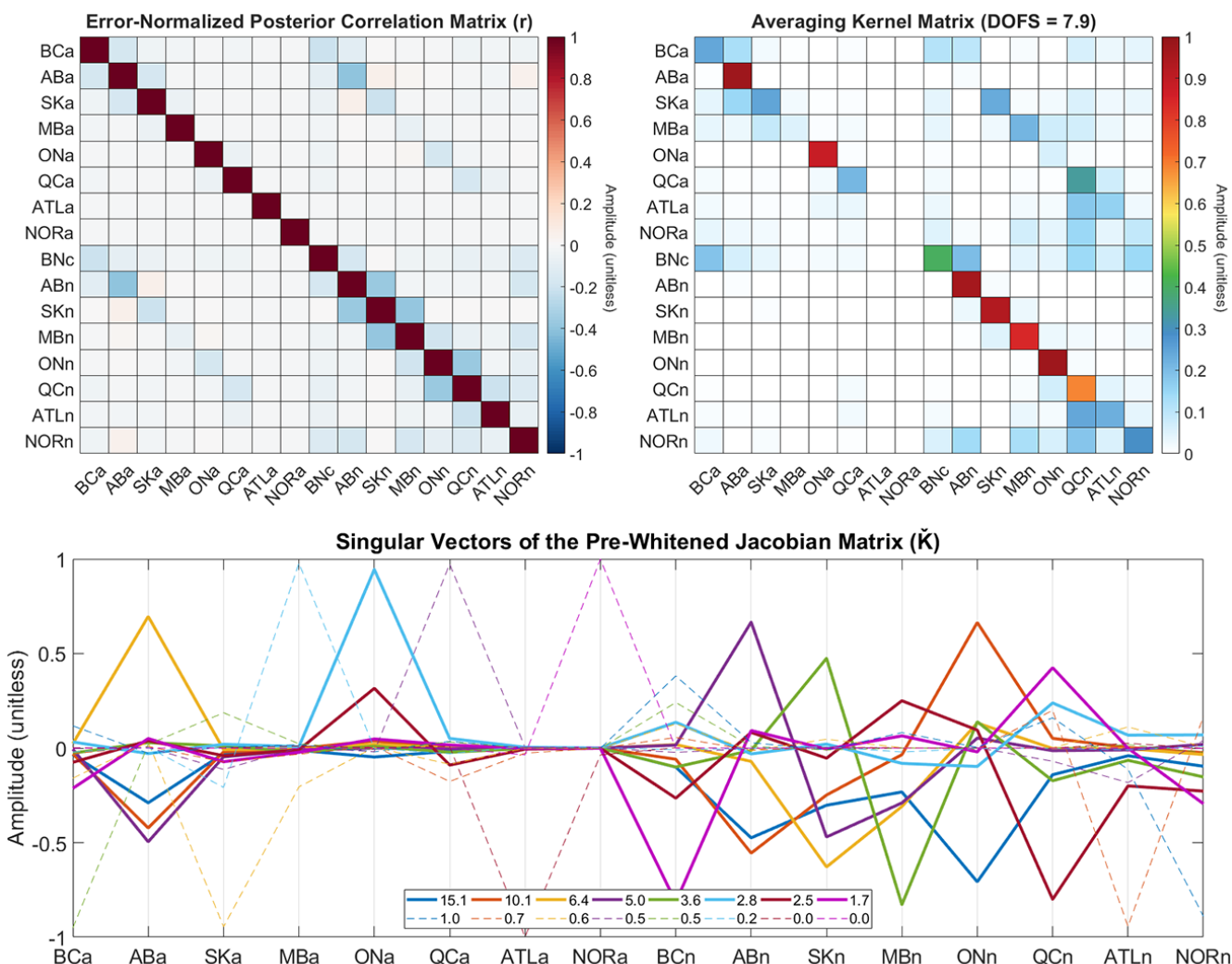


Figure S105: Similar to Fig. S4-S9 for the 16 state vector provincial inversion. The DOFS from the averaging kernel matrix are 7.9, which are consistent with the number of singular values greater than unity in the pre-whitened jacobian matrix (8 in total). *Note the difference in meaning of dashed lines between panels: in the top two panels, solid and dashed x lines of the same colour correspond to anthropogenic and natural emissions of the same province to help visualize the capability for disentangling intra province emissions.* In the bottom panel, the singular vectors below the noise (corresponding to singular values less than one) are shown as light-dashed lines, these show which emissions are not constrained by observations.

A possible solution to improving the resolution of the solution is to combine all six years of data to constrain finer scale emissions for the sectoral and provincial inversions. In the presented approach inversions were completed on a yearly basis for six years to produce an average result for 2010–2015. We used the year to year variance as a representation of noise in

the system and real yearly variability in the state (due to emissions and/or transport). In principle using more years of data provides a better signal to noise ratio. However, due to the way our state vector elements are defined in the sectoral and provincial inversions, the inverse approach is sensitive to aggregation error and overfitting the fewer number of well-defined state vector elements. Overfitting can be diagnosed using the reduced chi-squared metric:

1470

$$\chi_v^2 = \frac{\chi^2}{v} \cong \frac{\sum \frac{(y - Kx)^2}{S_o}}{m} \quad (43s)$$

1472

Where χ_v^2 is the chi-square per degree of freedom v . Here, the χ^2 is equal to the ratio of the square of the innovation, S_o is the diagonal element of the observational error covariance matrix corresponding to the same observation, m is the number of rows of the observation vector and n is the number of state vector elements. A value of χ_v^2 less than one indicates overfitting. We calculate a value of 0.65 for the total vector containing ECCC and GOSAT data which shows evidence of overfitting. Hence using a larger amount of data for the same number of state vector elements would exasperate the issue.

1478

We further test the improvement from combining 6 years of data against independent measurements. To evaluate the differences between using a repeated 1-year approach and a 6-year approach we use independent observations from NOAA ETL aircraft measurements and ECCC CHA in situ surface measurements. Table S32 lists the metrics of agreement that were in Figure 40-8 and compares them to the results using all 6 years of data simultaneously, using inversions with no model background corrections for the ECCC observation vector. For the sectoral inversion, using 6 years of data provides a small improvement in the slope (0.96 vs. 0.91), no improvement in the R^2 (0.20) and degrades the mean bias (± 4.3 ppb vs. ± 0.4 ppb) when comparing to NOAA ETL. Similarly with ECCC CHA data, using 6 years of data for the sectoral inversion provides an improvement in the slope (1.01 vs. 0.98), a slightly worse R^2 (0.43 vs. 0.44) and largely degrades the mean bias comparison (± 10.6 ppb vs. ± 5.9 ppb). For the provincial inversion evaluation at NOAA ETL, using 6 years of data slightly degrades the slope (0.83 vs. 0.86), gives an improvement in the R^2 (0.27 vs. 0.22), and degrades the mean bias (± 3.2 ppb vs. ± 0.5 ppb). The same comparison at ECCC CHA degrades agreement in the slope (0.87 vs. 0.91), improves the R^2 (0.51 vs. 0.47), and improves the mean bias (± 4.1 ppb vs. ± 4.9 ppb). These results show that using 6 years of data for the subnational inversions does not improve agreement against independent data and in many cases degrades the mean bias. The inversion converges on a solution within our defined prior error matrix S_o with only one year of data. These tests show that using one year of data at a time and calculating the average and variance of the repeated results is reasonable considering the limits of the observation system towards resolve low magnitude emissions.

1495

1496

1497

1498

1499
1500
1501
1502
1503
1504
1505
1506
1507
1508
1509
1510
1511
1512
1513
1514
1515
1516
1517
1518
1519
1520
1521
1522
1523
1524
1525

Table S2S3: Sensitivity test against independent observations

		NOAA Aircraft Observations ETL			ECCC Surface Observations CHA		
		Slope	R ²	Mean Bias (ppb)	Slope	R ²	Mean Bias (ppb)
Sectoral	Prior	1.15	0.14	± 6.8	1.17	0.36	± 16.4
	Posterior (1 yr)	0.91	0.20	± 0.4	0.98	0.44	± 5.9
	Posterior (6 yr)	0.96	0.20	± 4.3	1.01	0.43	± 10.6
Provincial	Posterior (1 yr)	0.86	0.22	± 0.5	0.91	0.47	± 4.9
	Posterior (6 yr)	0.83	0.27	± 3.2	0.87	0.51	± 4.1

We show a comparison of emissions estimates and methods to derive errors for the sectoral inversion in Table S3-S4 and for the provincial inversion in Table S4S5. The tables compare two error estimates to three sensitivity tests. They show the error estimates from the diagonal elements of the posterior error covariance matrix $\hat{\mathbf{S}}$ and compares to the 1σ variance in the repeated yearly inversions. In both the sectoral and the provincial inversions, the error estimates from the diagonal elements of $\hat{\mathbf{S}}$ often show a more optimistic estimate of the uncertainties. This is likely due to spatial and temporal correlations in the daily-mean ECCC in situ observations and correlations in the GOSAT data that are difficult to quantify in the absence of a full OSSE study. We compare the 1σ variance from repeated yearly inversions from 2010–2015 to the relative change in posterior emissions from using only ECCC data, only GOSAT data, and using 6 years of ECCC+GOSAT data simultaneously. The 1σ yearly variance captures these differences except for state vector elements that were shown to be below the noise and highly correlated with other emissions in Figure S4S9 and S5S10. The lack of improvement against the comparison to independent data in Table S2-S3 suggests that this may be suggestive of overfitting. We consider the agreement between the independent use of ECCC and GOSAT data to be a reliable sensitivity test to check the robustness of our results.

1526
1527
1528
1529
1530
1531
1532

1533
1534
1535
1536
1537

Table S3S4: Sensitivity analysis of the Sectoral (5 state vector) inversion. The error estimates from the posterior error covariance matrix are compared to the yearly variance and the change in emissions using alternative observation vectors.

	Prior (Tg a ⁻¹)	Posterior (Tg a ⁻¹)	Posterior \hat{S} Relative Error (%)	1 σ Yearly Variance Relative Error (%)	ECCC-only (% change)	GOS-only (% change)	6-year (% change)
Energy	2.4	3.6	± 11	± 25	+69	-76	-241
Agriculture	1.0	1.5	± 2928	± 2725	-01	-1619	+5764
Waste	0.9	0.68	± 3125	± 4725	-18	+8450	-3329
Wetlands	14.0	9.46	± 4	± 1211	-4+3	+34	+32
Other Natural	0.8	1.7	± 20	± 5655	-3731	-69	+7869

Table S54: Sensitivity analysis of the Provincial (16 state vector) inversion. As per S3-S4 error estimates from the posterior error covariance matrix are compared to the yearly variance and the change in emissions using alternative observation vectors.

	Prior (Tg a ⁻¹)	Posterior (Tg a ⁻¹)	Posterior \hat{S} Relative Error (%)	1 σ Yearly Variance Relative Error (%)	ECCC-only (% change)	GOS-only (% change)	6-year (% change)
BCA	0.5	0.8	± 24	± 41	-206	-11	+1157
ABA	2.3	3.32	± 5	± 1416	-6	+52	-2
MBASKA	0.3	0.3	± 44	± 4037	+1118	+1	+64
SKAMBA	0.2	0.2	± 4950	± 2625	-3+2	+56	+3322
ONA	0.5	0.45	± 2017	± 2514	-41	+2711	+2
QCA	0.4	0.3	± 51	± 4240	-114	+1719	+2314
ATLA	0.0	0.0	± 5251	± 4	+1	+3	-98
NORA	0.0	0.0	± 50	± 1	0	0	+1
BCN	0.4	0.56	± 3532	± 5350	-7+2	+135	-8076
ABN	2.4	1.9	± 14	± 34	+5967	-3029	-2625
MBNSKN	1.6	0.7	± 3128	± 4637	+7	+47	-4
SKNMBN	1.5	1.4	± 2122	± 3332	+1327	-96	-1311

ONN	3.5	0.9 <u>1.0</u>	±38 <u>32</u>	±57 <u>37</u>	+9 <u>12</u>	+13 <u>-3</u>	-18 <u>13</u>
QCN	1.6	1.2	±38 <u>40</u>	±38 <u>41</u>	+15 <u>9</u>	-30 <u>34</u>	-37 <u>51</u>
ATLN	0.7	0.8	±40 <u>39</u>	±27 <u>26</u>	-36 <u>29</u>	+24 <u>21</u>	+58 <u>48</u>
NORN	0.7	1.9	±14 <u>15</u>	±35	-45 <u>41</u>	-3 <u>2</u>	+73 <u>72</u>

1538 **S1.5 Combined ECCC+GOSAT Monthly Inversion**

1539 Figure S11 shows the monthly inversion comparing the results from the ECCC-only inversion, the GOSAT-only inversion
1540 and the combined ECCC+GOSAT inversion. The mean 2010–2015 anthropogenic emissions in the combined inversion is
1541 6.0 ± 0.4 Tg a⁻¹. The mean 2010–2015 total natural emissions in the combined inversion is 12.0 ± 0.9 Tg a⁻¹. The combined
1542 inversion agrees with the ECCC and GOSAT results and appears to follow the seasonality of natural emissions in the
1543 GOSAT-only inversion more closely. Combining the two datasets does not appear to improve the results of the individual
1544 inversions, hence the intercomparison between the ECCC-only and GOSAT-only inversions adds more value as a
1545 consistency test of the posterior results.

1546

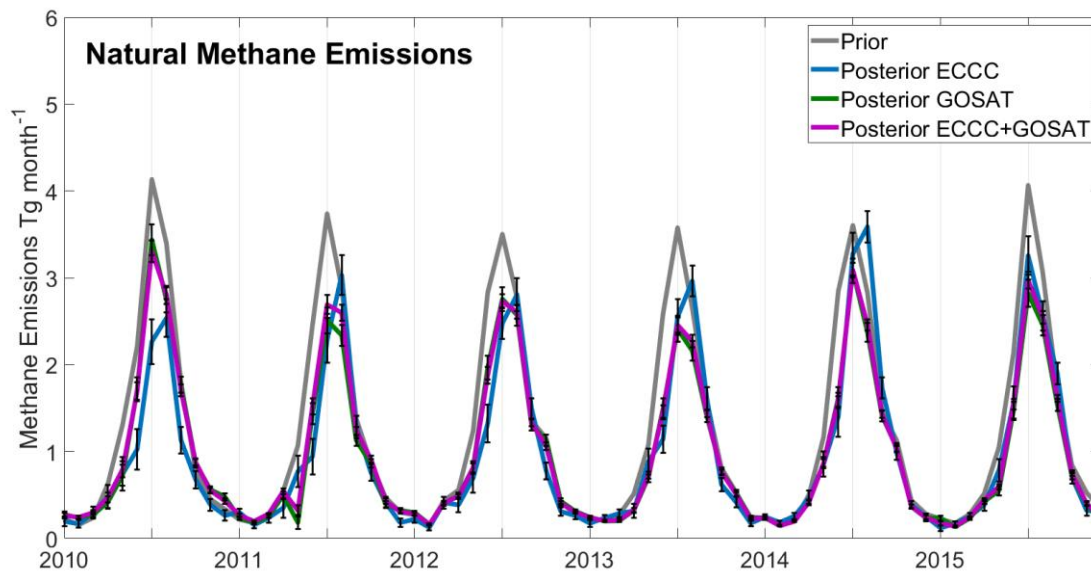
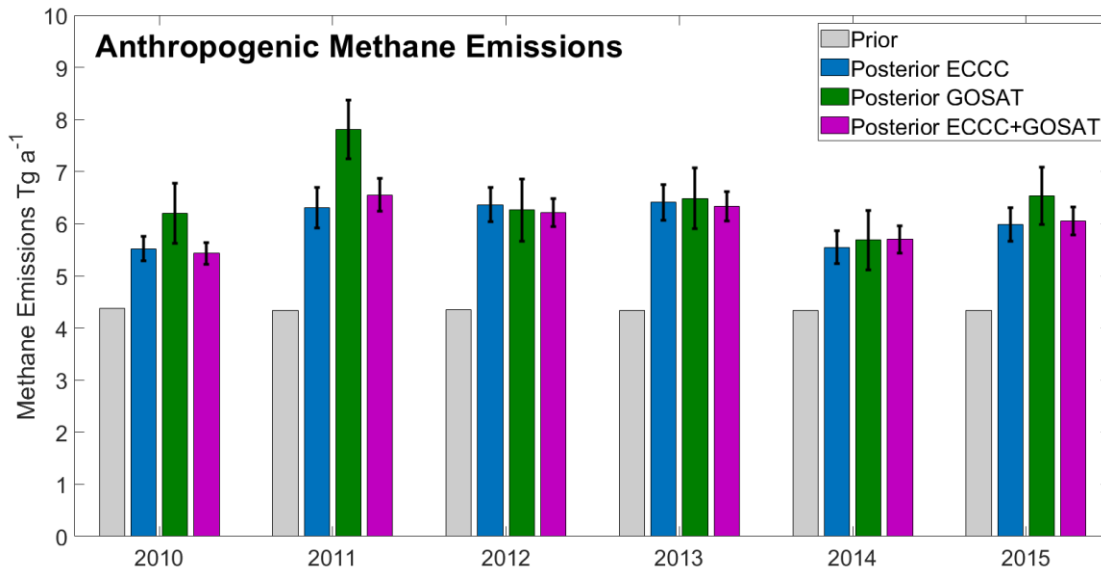


Figure S11: Sensitivity analysis of the results from the monthly inversion including a comparison to the combined ECCC+GOSAT inversion. Following Fig. 4 in the main text, the monthly inversion optimizes annual total Canadian anthropogenic emissions (top) and monthly total natural emissions (bottom) in an $n = 78$ state-vector element setup. The prior emissions (gray) are compared to the posterior results using GOSAT (green), and the posterior combining both ECCC and GOSAT data (purple).

1554 References

- 1555 [Buchwitz, M., Reuter, M., Schneising, O., Boesch, H., Guerlet, S., Dils, B., Aben, I., Armante, R., Bergamaschi, P.,](#)
 1556 [Blumenstock, T., Bovensmann, H., Brunner, D., Buchmann, B., Burrows, J. P., Butz, A., Chédin, A., Chevallier, F.,](#)
 1557 [Crevoisier, C. D., Deutscher, N. M., Frankenberg, C., Hase, F., Hasekamp, O. P., Heymann, J., Kaminski, T., Laeng, A.,](#)
 1558 [Lichtenberg, G., De Mazière, M., Noël, S., Notholt, J., Orphal, J., Popp, C., Parker, R., Scholze, M., Sussmann, R., Stiller,](#)
 1559 [G. P., Warneke, T., Zehner, C., Bril, A., Crisp, D., Griffith, D. W. T., Kuze, A., O'Dell, C., Oshchepkov, S., Sherlock, V.,](#)
 1560 [Suto, H., Wennberg, P., Wunch, D., Yokota, T. and Yoshida, Y.: The Greenhouse Gas Climate Change Initiative \(GHG-](#)
 1561 [CCI\): Comparison and quality assessment of near-surface-sensitive satellite-derived CO₂ and CH₄ global data sets, *Remote*
 1562 \[Sensing of Environment\]\(#\), 162, 344–362, doi:10.1016/j.rse.2013.04.024, 2015.](#)
 1563
- 1564 Heald, C. L., Jacob, D. J., Jones, D. B. A., Palmer, P. I., Logan, J. A., Streets, D. G., Sachse, G. W., Gille, J. C., Hoffman, R.
 1565 N. and Nehrkorn, T.: Comparative inverse analysis of satellite (MOPITT) and aircraft (TRACE-P) observations to estimate
 1566 Asian sources of carbon monoxide: COMPARATIVE INVERSE ANALYSIS, *J. Geophys. Res.*, 109(D23),
 1567 doi:10.1029/2004JD005185, 2004.
 1568
- 1569 Hutchinson, M. F., McKenney, D. W., Lawrence, K., Pedlar, J. H., Hopkinson, R. F., Milewska, E. and Papadopol, P.:
 1570 Development and Testing of Canada-Wide Interpolated Spatial Models of Daily Minimum–Maximum Temperature and
 1571 Precipitation for 1961–2003, *Journal of Applied Meteorology and Climatology*, 48(4), 725–741,
 1572 doi:10.1175/2008JAMC1979.1, 2009.
 1573
- 1574 [Maasakkers, J. D., Jacob, D. J., Sulprizio, M. P., Scarpelli, T. R., Nesser, H., Sheng, J.-X., Zhang, Y., Hersher, M., Bloom,](#)
 1575 [A. A., Bowman, K. W., Worden, J. R., Janssens-Maenhout, G. and Parker, R. J.: Global distribution of methane emissions,](#)
 1576 [emission trends, and OH concentrations and trends inferred from an inversion of GOSAT satellite data for 2010–2015,](#)
 1577 [Atmos. Chem. Phys., 19\(11\), 7859–7881, doi:10.5194/acp-19-7859-2019, 2019.](#)
 1578
- 1579 [Maasakkers, J. D., Jacob, D. J., Sulprizio, M. P., Scarpelli, T. R., Nesser, H., Sheng, J., Zhang, Y., Lu, X., Bloom, A. A.,](#)
 1580 [Bowman, K. W., Worden, J. R., and Parker, R. J.: 2010–2015 North American methane emissions, sectoral contributions,](#)
 1581 [and trends: a high-resolution inversion of GOSAT observations of atmospheric methane, *Atmos. Chem. Phys.*, 21, 4339–](#)
 1582 [4356, <https://doi.org/10.5194/acp-21-4339-2021>, 2021.](#)
 1583
- 1584 [Miller, S. M., Commane, R., Melton, J. R., Andrews, A. E., Benmergui, J., Dlugokencky, E. J., Janssens-Maenhout, G.,](#)
 1585 [Michalak, A. M., Sweeney, C. and Worthy, D. E. J.: Evaluation of wetland methane emissions across North America using](#)
 1586 [atmospheric data and inverse modeling, *Biogeosciences*, 13\(4\), 1329–1339, doi:10.5194/bg-13-1329-2016, 2016.](#)

1587

1588 [Saad, K. M., Wunch, D., Deutscher, N. M., Griffith, D. W. T., Hase, F., De Mazière, M., Notholt, J., Pollard, D. F., Roehl,](#)

1589 [C. M., Schneider, M., Sussmann, R., Warneke, T., and Wennberg, P. O.: Seasonal variability of stratospheric methane:](#)

1590 [implications for constraining tropospheric methane budgets using total column observations, Atmos. Chem. Phys., 16,](#)

1591 [14003–14024, <https://doi.org/10.5194/acp-16-14003-2016>, 2016.](#)

1592

1593 [Stanevich, I., Jones, D. B. A., Strong, K., Parker, R. J., Boesch, H., Wunch, D., Notholt, J., Petri, C., Warneke, T.,](#)

1594 [Sussmann, R., Schneider, M., Hase, F., Kivi, R., Deutscher, N. M., Velazco, V. A., Walker, K. A., and Deng, F.:](#)

1595 [Characterizing model errors in chemical transport modeling of methane: impact of model resolution in versions v9-02 of](#)

1596 [GEOS-Chem and v35j of its adjoint model, Geosci. Model Dev., 13, 3839–3862, <https://doi.org/10.5194/gmd-13-3839-2020>,](#)

1597 [2020.](#)

1598

1599 [Turner, A. J., Jacob, D. J., Wecht, K. J., Maasakkers, J. D., Lundgren, E., Andrews, A. E., Biraud, S. C., Boesch, H.,](#)

1600 [Bowman, K. W., Deutscher, N. M., Dubey, M. K., Griffith, D. W. T., Hase, F., Kuze, A., Notholt, J., Ohyama, H., Parker,](#)

1601 [R., Payne, V. H., Sussmann, R., Sweeney, C., Velazco, V. A., Warneke, T., Wennberg, P. O. and Wunch, D.: Estimating](#)

1602 [global and North American methane emissions with high spatial resolution using GOSAT satellite data, Atmos. Chem.](#)

1603 [Phys., 15\(12\), 7049–7069, doi:10.5194/acp-15-7049-2015, 2015.](#)

1604

1605

1606 ~~[Miller, S. M., Commane, R., Melton, J. R., Andrews, A. E., Benmergui, J., Dlugokencky, E. J., Janssens Maenhout, G.,](#)~~

1607 ~~[Michalak, A. M., Sweeney, C. and Worthy, D. E. J.: Evaluation of wetland methane emissions across North America using](#)~~

1608 ~~[atmospheric data and inverse modeling, Biogeosciences, 13\(4\), 1329–1339, doi:10.5194/bg-13-1329-2016, 2016.](#)~~

1609

1610 ~~[Stanevich, I., Jones, D. B. A., Strong, K., Keller, M., Henze, D. K., Parker, R. J., Boesch, H., Wunch, D., Notholt, J., Petri,](#)~~

1611 ~~[C., Warneke, T., Sussmann, R., Schneider, M., Hase, F., Kivi, R., Deutscher, N. M., Velazco, V. A., Walker, K. A. and](#)~~

1612 ~~[Deng, F.: Characterizing model errors in chemical transport modelling of methane: Using GOSAT XCH₄ data with weak](#)~~

1613 ~~[constraint four dimensional variational data assimilation, preprint, Gases/Atmospheric Modelling/Troposphere/Chemistry](#)~~

1614 ~~[\(chemical composition and reactions\)., 2019.](#)~~

1615

1616 Zona, D., Gioli, B., Commane, R., Lindaas, J., Wofsy, S. C., Miller, C. E., Dinardo, S. J., Dengel, S., Sweeney, C., Karion,

1617 A., Chang, R. Y.-W., Henderson, J. M., Murphy, P. C., Goodrich, J. P., Moreaux, V., Liljedahl, A., Watts, J. D., Kimball, J.

1618 S., Lipson, D. A. and Oechel, W. C.: Cold season emissions dominate the Arctic tundra methane budget, Proc Natl Acad Sci

1619 USA, 113(1), 40–45, doi:10.1073/pnas.1516017113, 2016.